

NASA CR-166,605

NASA-CR-166605
19840026637

A Reproduced Copy
OF

NASA CR - 166,605

Reproduced for NASA
by the
NASA Scientific and Technical Information Facility

LIBRARY COPY

MAR 3 1987

LANGLEY RESEARCH CENTER
LIBRARY, NASA
HAMPTON, VIRGINIA

FFNo 672 Aug 65



NF02166

BEST

AVAILABLE

COPY

(NASA-CR-166609) CONCEPTUAL DESIGN OF A
HYBRID Ge:Ga (Aerofjet ElectroSystems Co.)
136 p HC A07/MF A01 CSCI 14B

N84-34708

Unclas
G3/35 23153

Conceptual Design of a Hybrid Ge:Ga Detector Array

Christopher M. Parry

CONTRACT NAS2- 10740
July 1984

NASA



N84-34708#

Conceptual Design of a Hybrid Ge:Ga Detector Array

Christopher M. Parry
Aerojet ElectroSystems Company
Azusa, California

Prepared for
Ames Research Center
under Contract NAS2-10740



National Aeronautics and
Space Administration

Ames Research Center
Moffett Field, California 94035

FOREWORD

This report documents the results of, and completes, a study of FIR mosaic detector concepts for SIRTf undertaken by Aerojet Electro-Systems Company in accordance with Contract NAS2-10740 for the AMES Research Center of the National Aeronautics and Space Administration.

TABLE OF CONTENTS

Section	Page
1 INTRODUCTION AND SUMMARY	1
2 REQUIREMENTS	3
2.1 SIRTf Resolution and Minimum Number of Detectors	3
2.2 Background Photon Flux	3
2.3 Detector Performance Requirements	3
2.3.1 Detector G-R Noise	4
2.3.2 Detector Responsivity Requirements	5
2.4 Data Rates	8
2.5 Spectral Response and Stressing	8
2.6 Thermal Power Budget	8
3 DESIGN ALTERNATIVES	9
3.1 Technological Context	9
3.2 Array Architecture	11
3.2.1 Detector Opto-Electronic Size Constraints	12
3.2.2 Detector Geometry	16
3.3 Signal Processing	21
3.3.1 General Performance Considerations for an Integration Samples System	23
3.3.2 CCD and Monolithic Architectures	27
3.3.3 MOS Switch Multiplexers	29
3.4 Application of Uniaxial Stress	32
3.4.1 Thermally Induced Stress	32
3.4.2 Spring Loading	37
3.4.3 Mechanical Ram Loading	41
4 STRAWMAN DESIGN	42
4.1 Mechanical Assembly	42
4.2 Thermal Conductivity Considerations	48
4.3 Electronic Design and Performance	50

TABLE OF CONTENTS (Con't)

Section		Page
	4.3.1 Addressing Electronics	50
	4.3.2 Multiplexer Charge Integration Capacity	54
	4.3.3 Multiplexer Noise and Data Rates	56
5	CONCLUSIONS AND RECOMMENDATIONS	61
6	REFERENCES	64
APPENDIX A	ANALYTICAL DESCRIPTION OF Ge:Ga PHOTORESPONSE	A-1
APPENDIX B	OPTICAL EFFICIENCY AND CROSSTALK	B-1
APPENDIX C	INSTABILITY OF STRESSED GERMANIUM COLUMNS	C-1
APPENDIX D	TRANSPARENT ELECTRODE DESIGN FOR FIR GERMANIUM	D-1
APPENDIX E	VULNERABILITY TO SPACE RADIATIONS	E-1
APPENDIX F	DESIGN DATA FOR BELLEVILLE SPRING WASHERS	F-1
APPENDIX G	THERMAL BUSS COMPUTATIONS	G-1
APPENDIX H	MECHANICAL STRESS DESIGN COMPUTATIONS	H-1
APPENDIX J	HYBRID Ge:Ga DETECTOR ARRAY (Drawing Set)	J-1

1. INTRODUCTION AND SUMMARY

The Space Shuttle Infrared Telescope Facility (SIRTF) will provide a very low background environment for astronomical observations from earth orbit. The approximately one meter telescope is designed to be optimum in the mid-and long-wavelength infrared regions (3-100 μm) but its useful spectral range will extend to the far-infrared beyond 700 μm . The telescope will be cooled sufficiently that performance will be limited by natural backgrounds at wavelengths up to 100 μm . To efficiently cover the entire two micrometers to 1000 micrometer spectral range, focal plane instruments will utilize a variety of different detector species. Gallium doped germanium photoconductors are expected to find application for detection between 30 and 120 μm . Furthermore, if subjected to high uniaxial stress, a Ge:Ga detector's response can be extended to 200 μm .

In the initial flight(s) small arrays of discrete devices will be used. For later flights larger arrays in both one- and two-dimensional formats will be needed in cameras and spectrophotometers. For shorter wavelength applications such arrays utilizing doped-silicon detectors, monolithically integrated or hybridized with silicon MOS sampling, multiplexing and readout electronics, are already in an advanced state of development. In this study the feasibility of producing similarly high performance "mosaic" arrays of stressed Ge:Ga detectors has been examined and a baseline design concept established.

In Section 2 below the basic requirements and constraints of the focal plane subsystem are established, based upon the scientific mission requirements and tempered where necessary by experience with the development of detector arrays for other applications. In Section 3 fundamental electronic and mechanical design alternatives are compared and an optimum approach for near term implementation is selected.

A conceptual design for a two dimensional stressed Ge:Ga focal plane, suitable for SIRTF use and based on the selected design approach, is detailed in Section 4. This specific point design would provide a high fill factor square array of 49 detectors (7 x 7) arranged on 0.1 centimeter centers - approximating the resolution of the SIRTF telescope at 100 μm . The array design is modular and can be extended (or reduced) at will in either dimension. Array readout utilizes an integration

sampling approach with an individual photocurrent integration capacitor and reset switch for each pixel. Hybrid chip and wire implementation is proposed, and existing commercially available chips are identified and utilized for the package. Naturally some packaging benefits would accrue from custom design, but the performance benefit would be minor and cost impact major.

Section 5 addresses some of the critical issues which could (and should) be resolved prior to committing to this or similar approach for a preliminary design hardware phase. Some alternative design concepts worthy of study or development as potentially superior for far term applications are also identified.

2. REQUIREMENTS

To take full advantage of the cooled SIRTf, the focal plane must ideally provide background limited information at the data rates of interest and with a spatial resolution not significantly worse than that provided by the optical system. Starting from the baseline SIRTf design concept, and coupled with the performance characteristics reported for experimental Ge:Ga detectors, a self consistent set of requirements can be generated.

2.1 SIRTf Resolution and Minimum Number of Detectors

In accordance with the phase A SIRTf concept description [1] the telescope will provide an infrared field of view of approximately 7 arc minutes with a diffraction limit, defined at the first dark ring, of approximately $\lambda/100$ arc minutes, where λ is the wavelength in microns. The minimum array size (number of detectors) for 100 μm imaging should therefore provide approximately 7×7 pixels within the field of view. Since the Ge:Ga array(s) will also be used at shorter wavelengths - $\Delta\lambda/\lambda = 0.5$ is a baseline assumption - arrays up to 16×16 elements corresponding to 30 arc seconds per pixel would be useful in the SIRTf instrumentation.

Fill factor or the ratio of active to total focal plane area is important imaging systems. An 80% fill factor requirement was adopted in Ref [2].

2.2 Background Photon Flux

By cooling the telescope optics to 7^oK, thermal emission within the telescope will be reduced below the natural background due to zodiacal IR and interstellar dust. The minimum background spectral density is expected to be of the order 10^{-13} w/cm²/ster/ μm [1], corresponding to a photon flux of the order 2×10^4 photons/second/ μm for a 1 arc minute pixel. For spectral broadband measurements or for different numbers of sizes of pixels the background will vary accordingly. Steady state backgrounds of up to 5×10^5 photons/sec per pixel are to be expected for 40 μm to 50 μm broadband measurements.

2.3 Detector Performance Requirements

As a design goal the mosaic focal plane is required [2] to achieve an NEP equal to or less than 10^{-16} watts/ $\sqrt{\text{Hz}}$ at 100 μm for a 5 frames per second frame rate. The effective noise bandwidth for an integration sampled operating at fs samples

second is assumed to be $f_s/2$, the equivalent bandwidth of the corresponding sinc function. The requirement therefore corresponds to a wideband NEP of the order 1.6×10^{-16} rms watts, or 8×10^4 rms photons per second at $100 \mu\text{m}$. This is equivalent to a detection limit of 1.6×10^4 rms photons/sample.

2.3.1 Detector G-R Noise

Assuming that the incoming photon flux exhibits full shot noise, it is customary to invoke Boltzmann statistics and to write the sample noise attributable to the generation process as

$$\sqrt{\Delta n^2} = G \sqrt{\phi_B \eta \Delta T} \quad \text{rms electrons/sample}$$

Here G = the photo-conductive gain
 ϕ_B = average background flux (ph/sec),
 η = quantum efficiency (generation events/photon),
 ΔT = sample integration interval (secs),

and $\phi_B \eta \Delta T$ is the average number of generation events per sample. For photoconductors it is usual to assume that there will also be an equivalent contribution due to the statistical nature of the recombination process, since the average recombination event rate must be equal to the rate of generation events.

However, for long wavelength, such that $h\nu \ll kT$, classical Boltzmann forms no longer provide a good approximation to the Bose-Einstein statistics which describe the behavior of photons [7]. For bosons the shot noise expressions must be increased by a factor $\{1 - e^{-h\nu/kT}\}^{-1}$ over the usual Boltzmannian relationships. In the time domain, we find that the mean square generation fluctuation for an integration sample ($\bar{n} = G \phi_B \eta \Delta T$ electrons) becomes

$$\sqrt{\Delta n^2} = G \sqrt{\phi_B \eta \Delta T / \{1 - e^{-h\nu/kT}\}} \quad \text{rms el per sample}$$

and, transposing to the frequency domain, the generation noise spectral density is given by

$$\hat{n}(f) = G \sqrt{2\phi_B \eta / (1 - e^{-h\nu/kT})} \quad \text{rms electrons/sec-Hz}^{1/2}$$

Though not very different from unity under most circumstances the scaling factor can be substantial in the far infrared. For $100 \mu\text{m}$ radiation emitted by a 300 K blackbody for example,

$$\{1 - e^{-h\nu/kT}\}^{-1} = 2.64.$$

This "photon bunching" term accounts for the partial correlations associated with stimulated emission.

Bratt et al. [Ref. 3] considering the performance potential of Ge:Ga FIR devices, have applied the boson correlation factor to both the generation and recombination noise terms. It is not clear that this is justified since such correlation as exists is strictly associated only with the generation process. The recombinations of the resultant carrier electrons (or holes) are uncorrelated and are not governed by Bose statistics.

Ionizations by high energy particles for example provide a related situation. Here it is found that the associated noise is well represented by the generation term alone [Ref. 4] which is calculable independently. For event rates \dot{n} per second of average amplitude \bar{h} carriers per event the generation noise is proportional to $\bar{h}\sqrt{\dot{n}}$. Recombination on the other hand consists of $\bar{h}\dot{n}$ events of unit amplitude whose shot noise is proportional to $\sqrt{\bar{h}\dot{n}}$. The recombination noise is therefore lower by $\sqrt{\dot{n}}$ and is negligible when, as is usually the case for high energy particles, \bar{h} represents 10^3 to 10^4 bunched or correlated carriers.

In the "boson bunching" case of interest here it seems reasonable to assume that the recombination processes would be similarly uncorrelated. However here, because of the lower amplitude of the "bunching", the recombination noise will nevertheless remain significant though smaller than the generation term. The total background g-r noise will be of the form

$$\sqrt{\Delta n_{gr}^2} = G\sqrt{\phi_2\Delta T [1 + \{1 - e^{-h\nu/kT}\}^{-1}]} \text{ rms electrons/sample.}$$

2.3.2 Detector Responsivity Requirements

The responsivity of a detector may be expressed as the product of its quantum efficiency and photoconductive gain in the form of a quantum yield

$$\Gamma = \eta G \text{ electrons/photon}$$

or as a short circuit responsivity

$$R_I = 0.8 \eta G \lambda \text{ Amps/watt}$$

Multiplying the allowable system noise equivalent flux (1.6×10^4 photons/sample at 5 sps) by the quantum yield Γ , we obtain the allowable total sample noise $\sqrt{\Delta n_c^2} = 1.6 \times 10^4 G \eta$ rms electrons/sample.

In order to meet this overall performance requirement we must demand that the g-r noise contribution be less than this total so that

$$1 \geq \frac{\overline{\Delta n_{gr}^2}}{\overline{\Delta n_e^2}} = \phi \Delta T [1 + \{1 - e^{-h\nu/kT}\}^{-1}] / 2.6 \times 10^8 \eta$$

For the nominal design conditions

$$\Delta T = 0.2 \text{ seconds}$$

$$\text{and } \phi = 5 \times 10^5 \text{ ph/sec/pixel}$$

$$\text{at } \lambda = 100 \mu\text{m}, T = 300\text{K}$$

the requirement becomes

$$1 \gg \frac{\overline{\Delta n_{gr}^2}}{\overline{\Delta n_e^2}} = 1.4 \times 10^{-3} / \eta$$

In terms of quantum efficiency the demands on the detector are apparently not at all stringent. However the sampling, multiplexing and data conditioning electronics, and thermal g-r processes in the detector will also add noise to the total. The permissible contribution from these alternate sources is given by

$$\sqrt{\overline{\Delta n_a^2}} = \sqrt{\overline{\Delta n_e^2} - \overline{\Delta n_{gr}^2}} = 1.6 \times 10^4 G \eta \sqrt{1 - \frac{1.4 \times 10^{-3}}{\eta}}$$

and depends strongly on both the gain and quantum efficiency of the detector.

The total noise $\sqrt{\overline{\Delta n_e^2}}$ allowed by the nominal performance specification is plotted as a function of quantum efficiency for various values of gain in Figure 1. An equivalent detector responsivity scale is provided for reference, and a probable detector performance envelope is also defined, based upon the materials analysis of Appendix A. This is consistent with the recent materials performance survey by Haller and coworkers [8] which data points* are also provided for comparison.

Also plotted in Figure 1 are the relative amplitudes of the g-r noise and allowable readout system noise components. They are conveniently expressed as fractions (or %) of the total noise in a form dependent only on quantum efficiency. Within the anticipated nominal performance envelope, the g-r noise amplitude will clearly be negligible; ranging from 11% of an allowed total 250 rms electrons/sample case ($\eta = 0.1, G = 0.15$) to only 7% of a total 1700 rms electrons/sample in the most optimistic scenario ($\eta = 0.27, G = 0.4$). Evidently readout electronics performance will determine the ultimate quality of the system, and NEP levels significantly better than the nominal requirements should be possible with careful design.

* The detector evaluated by Haller et al. (Ref. 8) were mounted in integrating cavities.

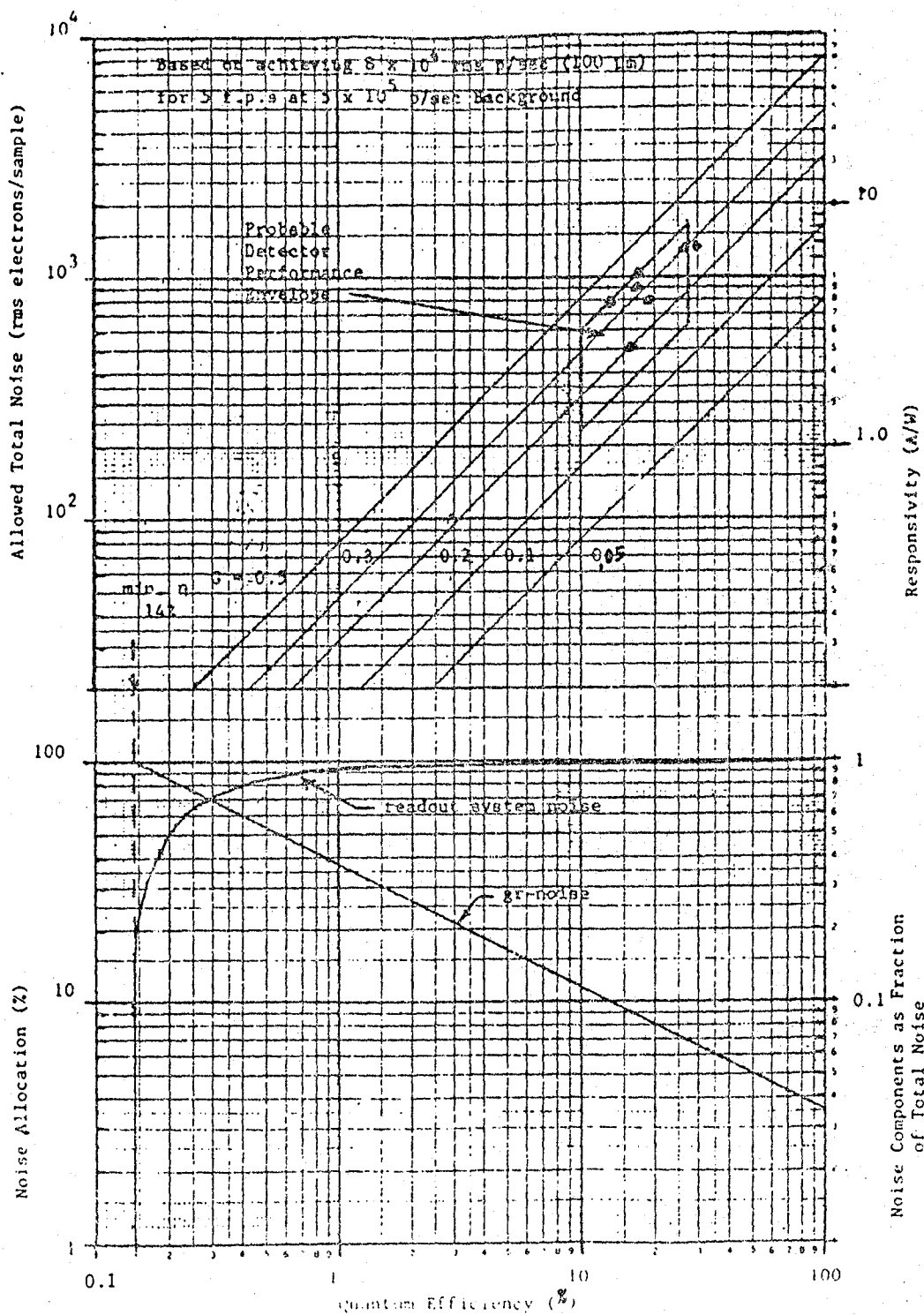


Figure 1 - Detector and Mux Noise Requirements

Background limited performance may be feasible at somewhat lower framcrates, where average integrated flux samples and the corresponding sample to sample variance are greater

2.4 Data Rates

Data rates may vary from the nominal 5 frames per second, (Ref 2) to as high as 100 frames/second or as low as 0.016 frames per second, corresponding to sample integration times from 10 msec to 60 seconds. By comparison with most silicon or HgCdTe mosaic systems the required data rates are thus quite low. Ionization by high energy particles may prevent use of the very longest proposed integration intervals. Expected ionization-pulse rates and amplitudes due to unshielded cosmic rays and trapped electron fluxes are discussed in Appendix E. Precise data rate limitations from this source will depend critically on the sensor deployment and experiments/measurements to be performed both of which remain to be determined.

2.5 Spectral Response and Stressing

In its normal condition the spectral response of Ge:Ga peaks in the vicinity of 100 to 110 μm with useful response extending to 125 μm . By uniaxially stressing the detector however, ground state impurity ionization energies can be modified to extend response to beyond 200 μm (e.g. Ref. 5,6). As a design goal, the ability to provide stress levels up to 90 Klb/in² is desired to extend the spectral response to beyond 200 μm .

2.6 Thermal Power Budget

The latest design concepts for the SIRTF/MIC cold station will provide up to 50 mW orbit average cooling at 2K. Since the Ge:Ga array instrument will possibly occupy no more than 30% of the MIC, a 17 mW orbit average power dissipation was established as a design goal for the mosaic array.

Cable conductance and optical load will dissipate power continuously but should not consume more than 10% of this budget. However the power dissipation of the array due to the detectors and any on-focal-plane signal processing electronics may if necessary exceed the remaining 15 mW average budget when operational since the instrument will likely be inoperative for significant segments of each orbit.

3. DESIGN ALTERNATIVES

The evolution of a specific point design necessarily involves the resolution of a large number of interdependent and frequently conflicting issues. The following paragraphs present the rationale for the particular mechanical and electronic configurations selected by AESC for a Ge:Ga mosaic array. In a few instances these choices verge on the arbitrary, and in others selections were necessarily made on the basis of incomplete data. Wherever possible however risk was minimized by favoring existing rather than developmental or speculative technologies. The resulting design approach, while certainly not representing the ultimate in either elegance or originality of concept, is nevertheless considered to be an eminently practical means for providing near state-of-the-art performance for the 80's time frame.

3.1 Technological Context

The development of two dimensional arrays (mosaics) of LWIR detectors in extrinsic silicon is well advanced. For use in moderate to high background conditions they have been integrated with readout multiplexers to form large fully monolithic arrays. Both photoconductor and MIS accumulation mode (majority carrier storage) operational modes have been employed with CCD and CID readout. For low background applications at very low temperatures CCDs tend to be less well suited and the utility of accumulation mode charge injection (AMCID) and direct charge transfer readout (DRO) MIS devices is complicated by long time constant response characteristics. Nevertheless, other concepts such as switch-addressed or coded-biased photoconductors, have progressed to the stage that application of the former to flight sensor systems is imminent. Hybrid silicon-on-silicon architectures providing for separate optimization of detector and multiplexer are now preferred. The performance achieved with these configurations mostly matches, and in some respects has surpassed, that available from a conventional linescanner photoconductor with a cryoMOSFET preamplifier. Considerable progress has also been achieved in hybridizing intrinsics (HgCdTe, PbS, InSb etc.) with silicon readout electronics to form mosaics in these alternate materials.

That the same progress has not been seen in germanium detectors stems mainly from the unfortunate economic reality that sponsoring agencies

have exhibited little or no interest in any applications which could not be served easily - and usually better - by silicon devices. The superiority of silicon in this regard is in part circumstantial, inasmuch as a well developed silicon active device technology (e.g. MOS/LSI) was independently available. It is also inherent. Besides the advantage of a highly stable native oxide silicon materials offer higher doping concentrations and absorption cross-sections as compared with their more or less equivalent germanium substitutes. Furthermore, in the shorter (!) wavelength germanium materials (Ge:Hg, Ge:Cd, Ge:Cu) the existence of very low ionization-energy impurities has historically had an adverse impact on device yield and uniformity. When uncompensated, they increase the tendency to impact-ionization breakdown and impose lower operating temperature requirements. When counterdoped they tend to reduce responsivity (shortening carrier lifetime) and may give rise to trapping effects.

It is these same very low ionization-energy impurity states, however, that have provided the basis for the continuing, albeit modest level of interest in doped germanium infrared detectors during the past decade. Extrinsic germanium materials such as Ge:Be and Ge:Ga (or Ge:B, Ge:Sb) offer one of the few viable means for high performance photon detection in the FIR spectrum beyond 30 μm .

Three factors now combine to provide the impetus for development which germanium has hitherto been lacking. The first, the ready availability of hyperpure material ($\sim 10^{10}$ impurities/cm³), has been extant for several years. The second factor is the burgeoning interest in infrared astronomy, particularly in the VLWIR (or FIR) between 10 μm and 1000 μm which represents a comparatively unexplored portion of the electromagnetic spectrum.

Although some ground based work had been performed using bolometers, and some Ge:Ga devices had been flown in balloon borne experiments, activity in this area has until comparatively recently been at a relatively low level. Earth's ambient background radiation being deleterious to any endo-atmospheric observation of VLWIR objects, NASA's development of the shuttle and the opportunity it presents as a platform for exoatmospheric telescope facilities therefore provides the third and key factor for the nascence of a Ge:Ga technology. The success of the recent IRAS deployment

has reinforced this prospect while validating the feasibility of an alternative free-flying cryogenic sensor.

Although late starting, the development of a Ge:Ga mosaic technology will have the advantage of building on, and drawing upon, a broad base of experience and insight acquired during similar efforts in extrinsic silicon and other detector materials. Though many, if not all, of the techniques which will be required for Ge:Ga mosaic design and fabrication may have already been developed for other materials, they are not necessarily transferrable as is. Most certainly the properties and requirements of Ge:Ga are sufficiently different, even from those of LWIR extrinsic silicon that approaches found optimum for the latter will not be applied to the former without extensive modification. Indeed, it is Aerojet's conclusion that for Ge:Ga a fully integrated monolithic detector/MUX design approach would be inappropriate. For the "80s" an architecture based upon assembly of linear array modules, hybridized with silicon MOS/LSI integration sampling and MUX readout electronics is recommended.

3.2 Array Architecture

Some of the features which adversely distinguish Ge:Ga from Si:X are:

- Low absorption coefficient - requiring very long absorption depth and/or integrating cavity configurations for high quantum efficiency.
- Large detector dimensions reflecting the lower resolution of sensor optics at very long wavelengths.
- Increased vulnerability to the natural radiations of the space environment due to the larger detector volumes and lower intrinsic energy bandgap of germanium.
- Low impact ionization breakdown field strength.
- Very low operating temperature.
- Requirement for highly uniaxially stressed configurations for extending the response spectrum to 200 μm .

Added to these inherent difficulties, the materials technology for growth of the large uniform crystals, indispensable for economical high-yield processing of large arrays, is comparatively undeveloped. A similarly undeveloped low surface-state-density MIS device technology in germanium, attributable in part to the lack of a stable native oxide, prevents any prospect of near term development of any Ge:Ga array architectures analogous to the fully integrated monolithic silicon arrays now becoming available.

On the positive side of the ledger, the larger detector sizes and spacing typical of the FIR make fully monolithic integration at the level achieved for silicon mosaics (and some HgCdTe and InSb devices) a less compelling prospect for Ge:Ga. Even the monolithic-to-monolithic hybridization of detectors and silicon readout electronics might represent overkill in this context. In short, architectures which would be considered rather crude and ineffective for shorter wavelength applications may be quite appropriate (if somewhat inelegant) for FIR focal plane construction.

3.2.1 Detector Opto-Electronic Size Constraints

In order to take advantage of the expected SIRTf resolution at 50 to 100 μm , detector element (pixel) dimensions should correspond to approximately 0.5 arc minutes IFOV or less. For the proposed 85 cm, $f/2.3$ SIRTf instrument with X10 secondary magnification, pixel dimensions would then be approximately 0.1 inches. Some demagnification may be implemented in the MIC instruments themselves so that a minimum detector size in the vicinity of 0.04 inches (1 mm) is probably appropriate. This size also seems to be approximately optimum from an optoelectronic standpoint for interelectrode spacing.

The effective absorption depth of the detector must be long compared to the pixel dimensions, and extremely long compared with the dimensions usually associated with silicon devices. The calculated quantum efficiency for a conventional, laterally-biased, rectangular Ge:Ga device (64% transmission at front and rear surface) of near optimum doping density is plotted as a function of wavelength for various absorption lengths in Figure 2. Clearly, without benefit of an integrating cavity (or equivalent) absorption lengths of the order of 2 cm or more may be required to achieve the desired

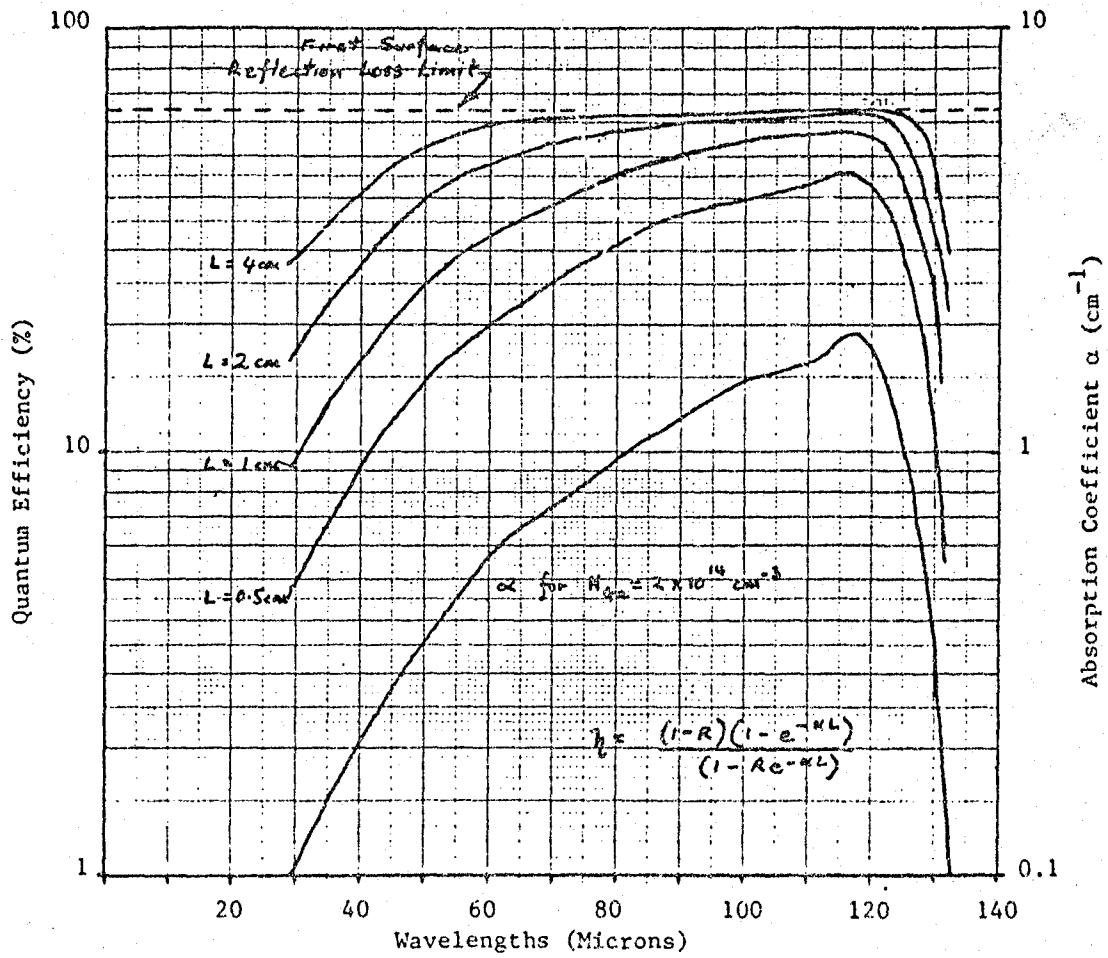


FIGURE 2 DEPENDENCE OF SPECTRAL QUANTUM EFFICIENCY ON ABSORPTION DEPTH

efficiencies (λ 30% say). For a transparent electroded device, where the back surface - the other electrode - may be considered to be near totally reflecting, the effective absorption depth is roughly double the nominal detector dimension, but thicknesses of the order of 1 cm or more would still be necessary.

As an interelectrode dimension however even 1 cm would be considered usually large. The bias field (E) required to achieve a given dc photoconductive gain (G) increases as the interelectrode spacing (L). Ignoring contact and space charge effects* we may write:

$$G = \frac{\text{lifetime}}{\text{transit time}} = \frac{E \mu \tau}{L}$$

where $\mu\tau$ is the mobility-lifetime product for the photo-generated carriers. For a detector with breakdown field strength E_B the maximum gain available is

$$G_{\text{max}} = E_B \mu\tau/L$$

inversely varying as the interelectrode spacing which should therefore be minimized.

Published data for Ge:Ga devices from several sources is reviewed in Appendix A, and is analyzed by fitting semi-empirically to the basic carrier transport and space charge relaxation models which have been developed over the last 15 years to very effectively describe the behavior of extrinsic silicon. While acknowledging that the detailed dependence of mobility and carrier lifetime on field, temperature and doping may differ from material to material there is reason to believe that the basic concepts and results embodied in the model are qualitatively applicable to any extrinsic. The analysis clearly indicates that an interelectrode spacing of the order of a millimeter is probably optimum for Ge:Ga.

* AC gain saturation due to space charge relaxation is dealt with in more detail in Appendix A.

For substantially larger dimensions the available photoconductive gain would be decreased. Referring to Figure A3 of Appendix A for example, note that as absorption thickness increases beyond a millimeter or so the computed performance of a monolithic transparent-electroded device (for which the absorption depth is also the interelectrode spacing) falls substantially below that computed for a laterally biased device with a smaller but fixed interelectrode distance. This despite the fact that the nominal absorption depth is effectively doubled by the reflecting back electrode in the former configuration.

On the other hand, decreasing the interelectrode spacing below the vicinity of approximately 1 mm will tend to further increase the available dc photoconductive gain, but will not appreciably enhance the ac response, and indeed may be a source of nonlinearities. (The saturation of ac gain due to dielectric relaxation, and the notion of dc to ac response ratio and its relation to long secondary response time constants and non linear effects is briefly discussed in Appendix A). For 1 mm interelectrode separation a 0.5 volt bias would be quite sufficient to produce ac gain saturation ($G_{ac} \approx 0.5$). The secondary response time constant is expected to be of the order of the dielectric relaxation time which defines the demarcation between ac and dc response regimes and hence to be photon flux dependent. It may be calculated from the relationships:

$$\begin{aligned} \tau_p &= \rho E E_o = \frac{e E_o}{n e \mu} = \frac{L \omega d e E_o}{\phi \tau n e \mu} \\ &= \frac{e E_o}{e} \cdot \frac{\omega d}{n L} \cdot \frac{L^2}{\mu \tau} \cdot \frac{1}{\phi} \end{aligned}$$

where L, ω and d are the detector dimensions, L being the interelectrode spacing, and $L^2/\mu\tau$ is the "saturation" bias voltage (V_{sat}) at which ac response is within 63% of its saturated gain value. For a 1 mm square (ω, L), laterally biased detector of moderately counterdoped material in a 10^5 p/sec-pixel flux (ϕ), V_{sat} would be of the order of 100 to 200 mV. (see Figure A2, Appendix A) and τ_p would be expected to be of the order of a few seconds. Since this is the middle of the signal passband of interest (namely sample-integration times ranging from 10 msec to 100 seconds or more) reducing bias to less than V_{sat} to reduce the dc to ac gain ratio may well be necessary to ensure system response linearity and/or unambiguous calibration.

Since the bias voltage required to achieve a given gain varies as the square of the interelectrode spacing, any significant reduction of this detector dimension below 1 mm would imply very small bias voltages. Though not inherently undesirable from the detector standpoint alone, it happens that a small bias voltage has unfortunate implications for the associated device readout electronics, particularly for the charge-integration sampling and multiplexing schemes utilized for high density mosaics. The lower the applied bias voltage, the lower the perturbation of voltage that can be tolerated at the detector signal node (i.e. integration node). All other parameters being equal reducing the detector size will therefore adversely impact useful dynamic range.

Related considerations lead also to the conclusion that striving for hyperpure Ge:Ga with extremely low counterdoping concentrations may not only be unnecessary but even undesirable. Hyperpure materials with fewer counterdoped (ionized gallium) recombination sites will exhibit proportionally longer carrier lifetimes, and require lower operational bias levels to achieve the limited levels of photoconductive gain (see Figure A2 for example), which are useful. Examination of the limited data available in Appendix A suggests that an ideal material would be characterized by N-type counterdoping of the order of 3×10^{11} donors/cm³. Gallium doping in the vicinity of 2×10^{14} /cm³ is also near optimum, higher levels leading to rapid decrease in breakdown strength and increased "hopping" conductivity without usefully decreasing the discrepancy between absorption depth and interelectrode spacing requirements.

In summary, for Ge:Ga, it seems that 1 mm represents a near optimum dimension both for pixel size and for interelectrode spacing, matching the SIRTIF IFOV requirements, and maximizing useful photoconductive gain. On the other hand an effective absorption length on the order of 2 cm may be necessary to achieve the desired quantum efficiency throughout the 40 to 120 μ m range of an (unstressed) Ge:Ga detector.

3.2.2 Detector Geometry

The basic geometry of detector configuration may be defined in terms of three vectors representing the applied bias field (E)*, the

*The applied field may be modulated as in the case of COBM or AMCID arrays.

incident radiation (\bar{I}) and, in the case of the proposed FIR Ge:Ga, the direction of uniaxial stress application (\bar{F}). In principle these may be arranged in any convenient manner from mutual orthogonality on the one hand to directional coincidence on the other. If however we take it as axiomatic that lack of a suitably transparent mechanical loading structure will preclude colinearity of incident radiation and applied stress, then the three alternatives delineated in Figure 3 remain distinguishable by the orientation of the applied electric bias field in relation to the orthogonal \bar{F} and \bar{I} vectors.

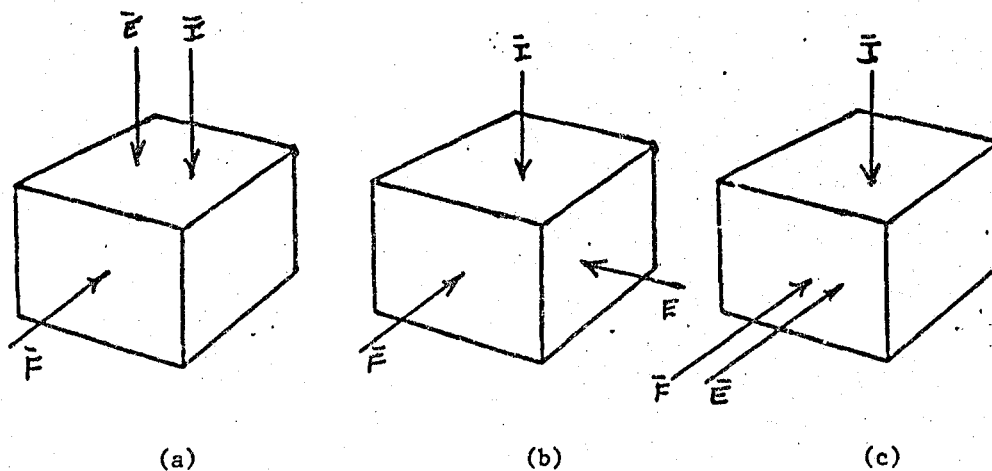


Figure 3 Alternative Orientations of Applied Bias Field (E) With Respect to the Incident Radiation (I) and Uniaxial Mechanical Stress (F)

Configuration (a) represents the approach now employed almost exclusively for extrinsic silicon detector manufacture. The principal advantage of this design, which utilizes a transparent front surface electrode is that it lends itself readily to the manufacture of higher density mosaic arrays, and is in fact the only way (presently known) for making such arrays monolithically. A secondary but significant benefit in certain applications is the fact that this design renders all points on the incident surface equivalent

with regard to bias field distribution, thereby avoiding the space-charge related spatial response non-uniformities to which laterally biased extrinsic devices are particularly prone when they are partially or non-uniformly illuminated. For silicon devices a further advantage of this structure is that pixel dimensions may be adjusted at will, independent of the optoelectronically critical absorption length and interelectrode spacing which become one and the same.

For doped germanium detectors the transparent electrode configuration approach is far less favorable. For the lightly doped FIR species like Ge:Ga the gross discrepancy between the optimum values of absorption depth (> 1 cm) and interelectrode spacing (~ 1 mm) as discussed above presents a particularly serious problem. Furthermore transparent electroding of VFIR stressed germanium has not been demonstrated and may also have inherent problems associated with the conflicting requirements for high conductivity and low free carrier (plasma) optical absorption (Ref 9). Even if these issues could be resolved however, the practicability of a fully monolithic structure in a fast optical system is limited by excessive internal optical crosstalk (Appendix B) when absorption depth is very large compared to pixel dimensions. If somehow absorption depth could be reduced to only a few millimeters reducing crosstalk to acceptable* levels, then the maximum size of the array would now become restricted, by column instability under stress, to less than about 15 pixels which, though currently acceptable, would be unduly restrictive in the long term.

The special properties of Ge:Ga and of the FIR environment thus combine to defeat any concept of a fully monolithic mosaic analogous to state-of-the-art silicon arrays. Alternative less elegant approaches must be pursued, constructing mosaics from ensembles of linear array modules based on the geometries of Figure 3b or 3c. Column instability (Appendix C) limits the first of these in which the stress and bias field vectors are orthogonal to arrays of about 6 or 7 pixels length. The only approach that seems to be fully compatible with all the requirements and constraints, and which is

* In silicon mosaics for example absorption depth is usually no greater than about 1.5 times the pixel spacing.

in principle capable of unlimited extension in both dimensions is the configuration of Figure 3c in which the mechanical stress is parallel to the bias field, the load being applied through the electroded surfaces. This configuration has the added advantage that it is the only one for which the individual elements of an array may be physically segmented to reduce optical crosstalk. Further benefits of the non-monolithic configuration(s) include the compelling practical advantage of being less demanding of ingot size and uniformity.

The actual absorption length (and volume) of each detector can also be substantially reduced, decreasing thermal noise, decreasing vulnerability to cosmic rays, and decreasing the magnitude of the load to be applied to the structure (but without loss of quantum efficiency) by bevelling the end of the detector. The idea is to make the detector element its own integrating cavity by promoting total internal reflection within the detector itself, thereby extending its effective absorption depth significantly, compared with its actual depth. This objective is easily accomplished by placing a bevel on one face of the detector. The technique has been used extensively by Aerojet in the past. For example, Ge:Hg detectors were reduced from about 3 mm to only 1 mm length (while increasing quantum efficiency from 20 to 40%) by applying an 18° bevel to one end. Several hundred subarrays of 360 detectors, each only 4 mils square section, were manufactured in this fashion for a series of FLIR systems. Application to the much larger Ge:Ga devices should present no difficulty. Computations have been performed for otherwise rectangular detectors with the end bevelled at some angle α . The theoretical increase in effective length is plotted, for germanium of index 4.0, in Figure 4. The optimum bevel angle is approximately 18° , where effective lengths an order of magnitude larger than the actual absorption depths are feasible. Because of the high index of germanium, high-angle incident rays will be refracted near normal, so that the technique can be effective even for a fast, wide angle optical system. Note that bevelling at about 28° allows up to at least $\pm 6^\circ$ internal (refracted) angular range ($\pm 25^\circ$, f/1 incident) while nevertheless still permitting a substantial reduction (≈ 3.5) in absorption length.

480-3009

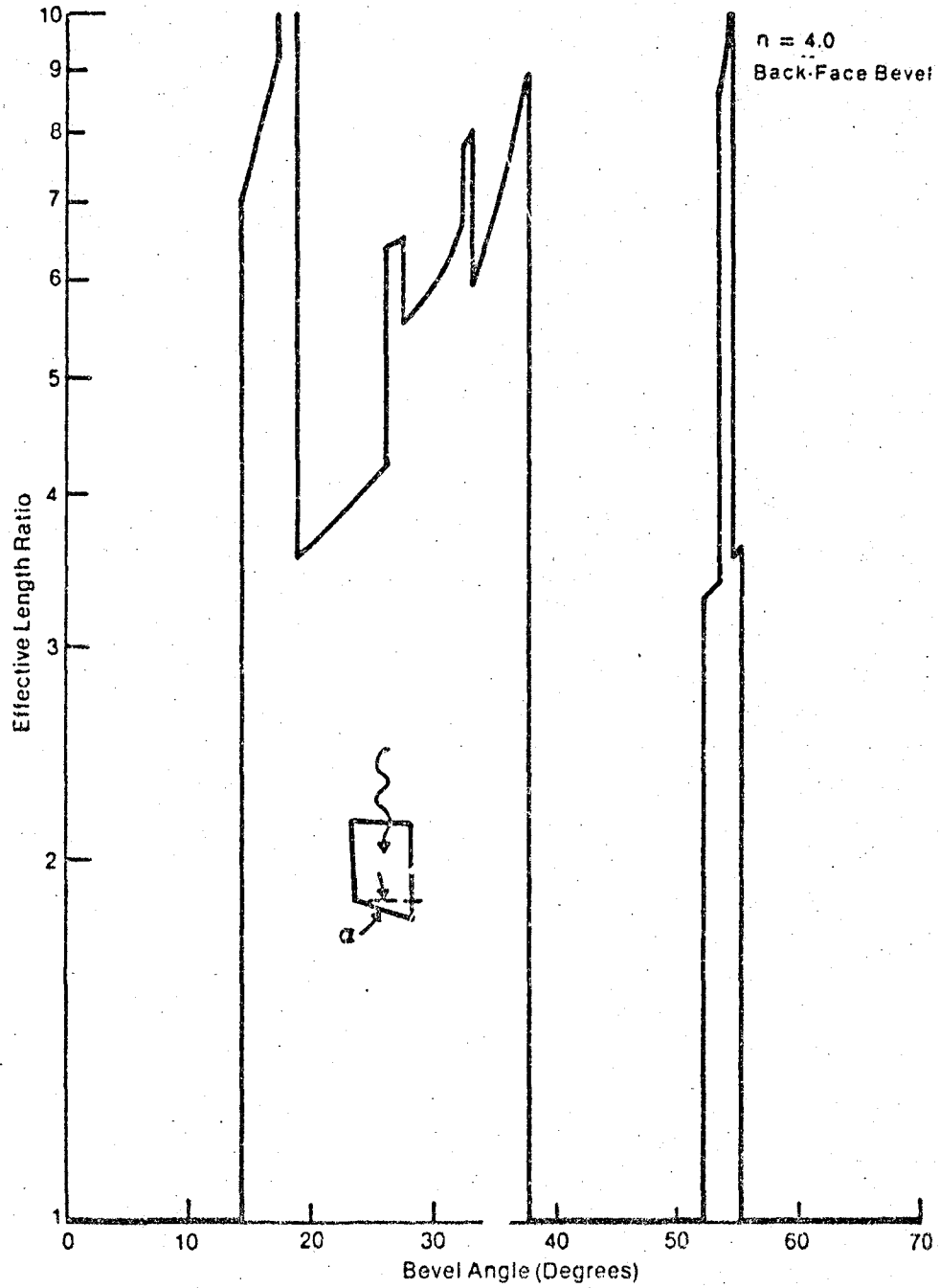


FIGURE 4 EFFECTIVE ABSORPTION DEPTH VS BEVEL ANGLE

ORIGINAL FILED
OF POOR QUALITY

3.3 Signal Processing

Historically, when extrinsic photoconductors have been used for long wavelength infrared detection under low background conditions, state-of-the-art performance has been realized by operating each such detector with a contiguously located cooled impedance matching source follower preamplifier load-resistor and low-noise, high input impedance cryogenic MOSFET as shown in Figure 5.

579-3075

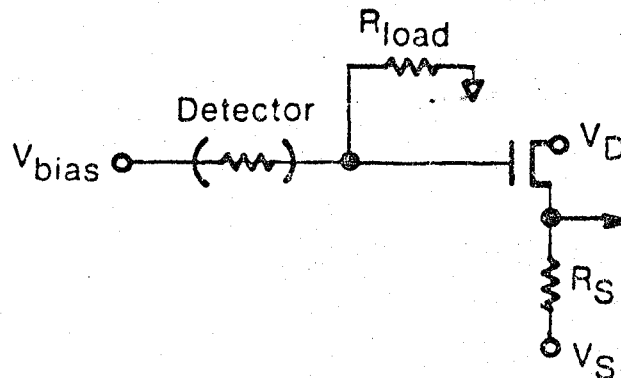


FIGURE 5 : Conventional Cryopreamplifier Circuit

The bandwidth and dynamic range of such a circuit is often extended by making the load resistor the feedback element of a high-loop-gain transimpedance amplifier. For astronomical applications, where very faint objects may be observed over long periods of time, dc stability (or very low frequency $1/f$ noise) are clearly important. DC drift proved to be such a critical issue in the design of the IRAS focal plane for example (Ref. 10) that a special transistor (the ZK111) was developed for this application and used differentially in matched pairs, because the standard devices customarily used for higher frequency military LWIR sensors were found wanting. Such a configuration also poses numerous problems related to packaging and assembly, power dissipation etc.; difficulties which become particularly onerous for two dimensional arrays. In the present context, where arrays of up to 64^2 pixels are under consideration such an approach becomes quite untenable. For large

mosaics, on-focal-plane multiplexing is mandatory to reduce the interconnects and data channels to viable numbers. Simply multiplexing the preamplifier outputs is insufficient however. Radically new approaches to device architecture are required; some form of sampling system is necessary, with at least an order of magnitude lower per channel power dissipation than that of the conventional preamplifier.

Numerous schemes for reading out mosaic arrays of detectors have been conceived from time to time and Aerojet has, over the years, had some direct experience with most if not all of the basic types. Certain of the readout concepts are inherently inappropriate for low background Ge:Ga and may therefore be rejected summarily. Amongst these we may include the charge injection readout and lateral direct charge transfer schemes which are appropriate only for MIS charge storage detectors such as the AMCID [eg Ref.11&12] and which demand a fully monolithic transparent electrode type of configuration. Also the pulsed or coded bias (orthogonal carrier wave) approaches are appropriate only for very slow responding detector [Ref 13] or for systems which do not aspire to background limited performance [Ref 14]. Ge Ga detectors are fast compared with data rates of interest and although the SIRT and other space astronomical instruments will operate at very low backgrounds, they nevertheless can potentially achieve background limited performance through sufficiently long term integration.

In order that the maximum benefit be realized from the use of a large mosaic of detectors it is almost axiomatic that the bandwidth of each device should be restricted, prior to sampling, and multiplexing, to a value less than, or of the order of, the sample rate. This ensures that the data is not under-sampled and that the inherent, detector noise limited, performance is maximized. This might be accomplished naturally, through selection of inherently slow response detectors (as in Aerojet's pulse-biased PbS mosaics [Ref 13]) or by using pre-sampling signal conditioning circuitry. The former approach, as pointed out above, is not consistent with the fast response of typical extrinsic photoconductors, while the latter is too unwieldy and inflexible.

A more usual alternative is to use an integration sampling approach that provides, for each detector, an associated storage element (usually a capacitor) in which data (charge) can be continuously accumulated between

readout events, thus imposing a $\sin x/x$ type bandwidth limitation. A variety of such schemes have been devised from time to time. The essential features are a corresponding array of capacitances to which the detectors are connected, and a means for addressing and reading the accumulated charge on each capacitor before clearing or resetting it to some nominal zero reference from time to time. The key to efficient operation is the high duty cycle use of the capacitor for near continuous integration of the detector response. Generally it is only in this way that we can assure bandwidth limiting of the detector noise, and avoid undersampling or "folding" of high frequency noise in the system information passband at the sample frequency and below. Clearly this requirement implies that there shall be a capacitor dedicated to each and every detector pixel. The sizing of this capacitor in relation to the amplitude of the detector photocurrent, the permissible voltage swing during integration, and the noise of the subsequent interfacing and sampling electronics determines the sensitivity and dynamic range of the system.

As discussed above monolithic structures are precluded by the mechanical, opto-electronic and MIS properties of Ge:Ga. A hybrid scheme coupling the Ge:Ga detectors to a silicon integration capacitance array and readout multiplexer, and providing for the separate optimization of each, is indicated.

3.3.1 General Performance Considerations for an Integration Sampled System

The essential features of the integration sampling scheme, consisting of the detector, integration capacitance, reset switch and sensing amplifier and sample-and-hold are illustrated in Figure 6.

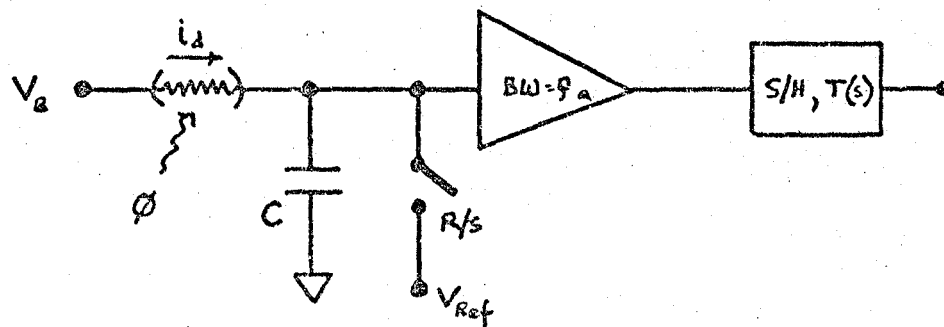


Figure 6 Basic Integration Sampling System

improvements through a variety of modifications and embellishments.

The detector is biased at some dc potential V_B and the photocurrent i_d is integrated on the capacitance C . From time to time the sample-and-hold senses the values, suitably amplified, of the voltage on the integration capacitance. The capacitor is then reset to the reference voltage (which will be taken as zero volts for the purposes of this analysis) and the integration cycle starts anew. The amplifier has some bandwidth f_n and an equivalent input noise spectrum $v_{na}(f)$. The sampling action on this noise may be represented by a transfer function $T(f)$.

The amplitude of a sample may be defined in terms of the change in the charge ΔQ_s or voltage ΔV_s induced at the integration capacitance by the photocurrent during the integration interval ΔT . Thus

$$\Delta V_s = \Delta Q_s / C = \frac{1}{C} \int_0^{\Delta T} i_d dt = e \eta G \phi \Delta T / C$$

where ϕ is understood as the average photon flux on the pixel during the sampling interval. Note that the concepts of "signal" and "dc background" have no real meaning for a single sample, but rather are attributes of a sequence of samples.

The detector is debiased by the voltage excursion ΔV_s at the integration node so that for linearity (ie. constant gain G) we demand

$$\Delta V_s \ll V_B$$

or $C \gg e \eta G \phi_{max} \Delta T / V_B$

Thus linearity and dynamic range are clearly enhanced by maximizing the integration capacitance.

The detection limit δQ_a rms coulombs/sample (ie. the smallest detectable charge) set by sampling the wide-band noise δv_a of the amplifier is

$$\delta Q_a = e \eta G \Delta T \phi_{min} = C \delta v_a = C \left\{ \int_0^{f_n} [v_{na}^2(f) T^2(f) / (1 + f_c^2)] df \right\}^{1/2}$$

There is therefore an inherent design conflict between the desire to maximize responsivity and minimize NEP by minimizing integration capacitance, and the need to maximize linear dynamic range by maximizing C .

which it is measured the sensing system may or may not be the limiting noise source. For large enough samples the detector g-r noise will become dominant. The minimum g-r contribution is represented by two full shot-noise contributions

$$\delta Q_{gr} \geq \sqrt{2e\Delta Q_s}$$

and as pointed out above (Section 2.3.1), dependent on the wavelength and temperature of the source, the actual value of the generation component may be larger due to boson-bunching.

If measured directly with respect to some fixed system zero each sample would include a so-called "kTC" contribution representing the error in resetting to the dc reference supply (which is itself assumed to be noiseless). The "kTC" noise is equivalent to Johnson noise, and in fact may be thought of as arising out of the integration of the Johnson noise current of the charging circuit resistance. It results in a wideband rms noise reset error

$$\delta v_r = \sqrt{kT/C}$$

or equivalently, in terms of the residual charge on the integration capacitor,

$$\delta Q_r = \sqrt{kTC}$$

In practice, samples are not measured referenced to some arbitrary fixed system zero. To minimize the effects of the dc drifts and to permit ac coupling of the system, ΔV is usually measured as the difference between two samples representing the end and beginning of each integration interval, and measured immediately before and immediately after reset respectively. The effect of this delayed differential sampling is to suppress low frequency system noise corresponding to periods long compared with the delay τ between samples. In mathematical terms delayed differential sampling of a waveform $v_u(t)$ is equivalent to sampling the modified waveform $v_u(t) - v_u(t + \tau)$. In the frequency domain the transfer function relating the spectral content of the latter to that of the former original waveform is

$$|T(f)| = 2 \sin \pi f \tau$$

which peaks at $f = 1/2\tau$ and is attenuated by a factor of two at $f = 1/\tau$.

The two basic approaches to delayed differential sampling are illustrated in Figure 7 and differ in subtle but important ways. In true correlated

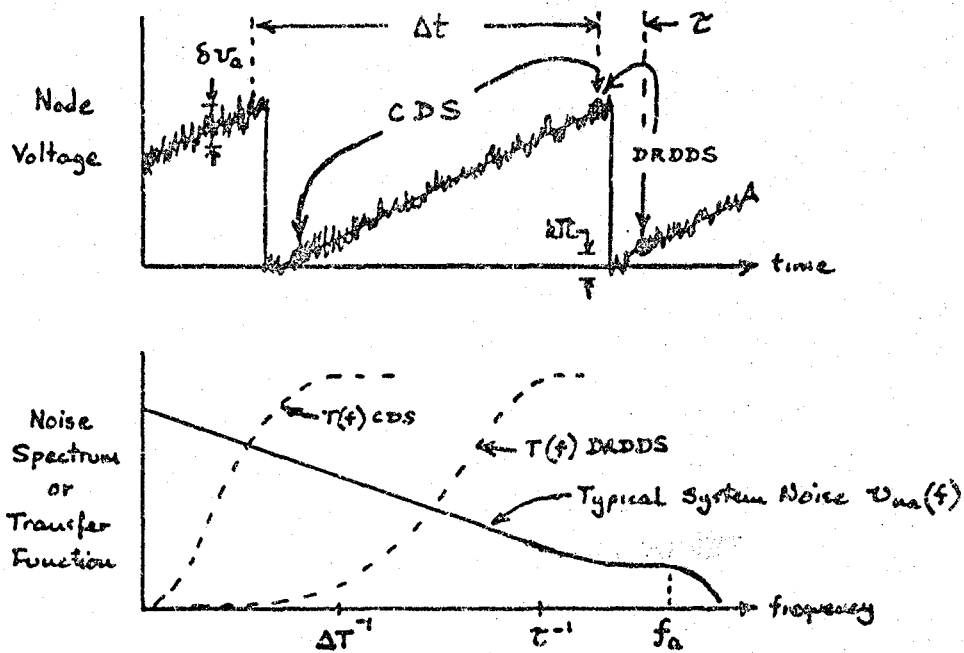


Figure 7 COMPARISON OF CDS AND DRDDS

double-sampling (CDS), measurements are made at the beginning and end of a single integration interval so that the delay time is approximately equal to the sample integration time ΔT . The advantage of CDS is that the kTC noise contribution is eliminated. System baseline drifts on the timescale of the integration time ΔT will be observed however. Moreover this approach may be inconvenient in some multiplexed systems inasmuch as during the integration interval (the frame time) other channels must be examined and data must be stored for a complete frame. Furthermore effective correlation may actually be totally lost if the interface component undergoes any radical change of state (being turned off for instance) during the reading of the other devices multiplexed on the channel. For example, the thresholds of certain cryo-MOSFETs have been observed to vary by as much as ± 5 mV as they are turned on from time to time.

The alternative to CDS is the "delta-reset" delayed differential sampling (DRDDS) which compares measurements made before and after a single reset operation. This operation can be performed in a few microseconds so that low frequency $1/f$ noise and dc drift in the electronics are essentially eliminated, though two kTC noise contributions are now included. If sufficiently fast, the speed of each dual sampling operation can be independent of the overall sampl-

ing rate. Thus for DRDDS system noise can be independent of sampling rate and signal processing can also be ac coupled at a fixed high frequency. The low pass corner frequency is chosen to permit settling to the required accuracy during the time available for sampling. Since both CDS and DRDDS require the same total number of sampling and reset operations within a frame time their bandwidth requirements are not sensibly different.

3.3.2 CCD and Monolithic Architectures

In principle at least, the applicability of CCDs to meet the integration sampling requirement is rather obvious. A CCD-multiplexer input scheme is shown in Figure 8 which is analogous to the conventional cryogenic-preamplifier circuit used for discrete extrinsic PC detectors as shown in Figure 5. The circuit is most useful where currents are high and dc isolation is required between detectors and readout. Its principal disadvantages are that a high-value load resistor must be provided for each detector, and that the response bandwidth is limited in the same way as for discrete cryogenic-MOSFET channels. At the expense of increased complexity, the need for a resistor can be eliminated (for small currents) by allowing the detector current to charge or discharge the input capacitance, while maintaining an average operating point

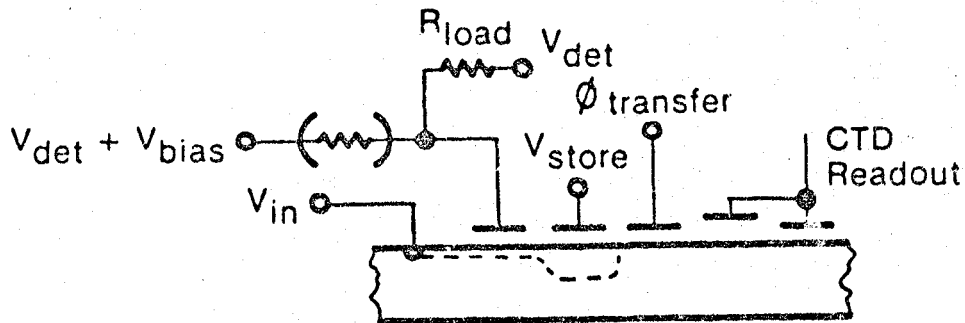


FIGURE 8 Voltage Mode CCD-Input

either by incorporating a reset switch or possibly reversing the detector-bias-voltage polarity from time to time. Clearly however the system must suffer from the same dc drift problems as the conventional discrete MOSFET preamplifiers in addition to any noise introduced by charge transfer and readout.

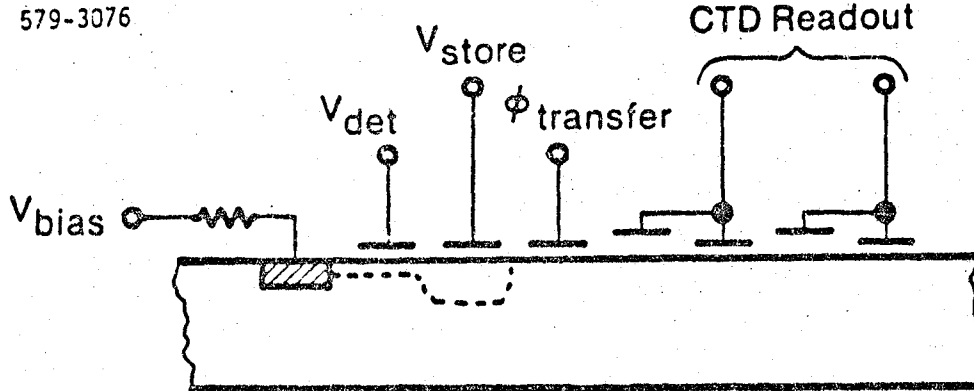


FIGURE 9 Direct Injection CCD Input

The alternative "direct injection" configuration illustrated in Figure 9 avoids the need for load resistors and has been used extensively and successfully for high-background applications in which detector currents are comparatively large. Under low-background conditions however such devices suffer from severe bandwidth and injection-efficiency difficulties. The circuit behaves like a common-gate MOSFET with the input diffusion acting as the source and the storage-potential well as a virtual common drain. The input time constant is given approximately by C/g_m where C is the total capacitance (detector plus stray) of the node, and g_m is the transconductance of the equivalent MOSFET. At very low currents g_m is directly proportional to current and hence to photon flux. Under low background conditions the response time is therefore not only slow, which might be tolerable in a long dwell staring system, but will also tend to vary continuously as the background and signal operating conditions of the system are varied. Additionally transfer noise, due to the "sticking" of some varying fraction of the charge samples in slow and intermediate surface states (Ref 15) has limited the performance of surface channel silicon CCDs under cryogenic temperature conditions to sampling

noise levels of 500 to 10^3 e/sample at best near 10 K. The noise mechanism is related to that which is believed responsible for $1/f$ noise in a conventional MOSFET preamp. At 2 to 3 K additional surface state traps which are thermalized at the higher temperatures may be expected to become active leading to further degradation.

The principal system advantages of charge transfer type readout are the ability to perform on-focal-plane TDI, and the ability to perform second level multiplexing to provide a single channel output from a two dimensional array. Neither attribute is particularly useful in this context where the sensor will likely be operated in a staring rather than scanning mode, and the mosaic will likely be constructed as an ensemble of separate linear arrays. The directly coupled CCD is ideal theoretically from the response standpoint in that the input integration capacitance can be large compared with the capacitance of the readout stage, thereby independently maximizing linear dynamic range and responsivity, and true CDS is also possible with delay times comparable to those of the DRDDS mode. Consequently, though in practice the CCD has so far been found inferior for small signal operation at cryogenic temperatures, future developments may make a reassessment necessary in situations where narrow response bandwidth is not a driving issue.

3.3.3 MOS Switch Multiplexers

An alternative to the charge transfer readout is the direct accessing of the integration capacitor (with resetting from time-to-time) using MOS switches. A variety of such schemes have been widely used in photodiode as well as LWIR arrays. The simplest version of this generic type is the direct access charge sensing scheme illustrated in Figure 10 where each unit cell consists of only a single MOSFET switch which isolates the photocurrent integration capacitance from the output buss. To "read" a particular pixel its switch is turned on causing the charge to be "shared" with the output buss capacitance C_b .

The buss and node are then both restored to the reference voltage by the reset switch.

The sample amplitude is represented by the change in the output voltage of the sensing amplifier which can be measured before and after accessing the detector node, or in DRDDS mode before and after reset. The former method eliminates kTC noise as in true CDS sampling.

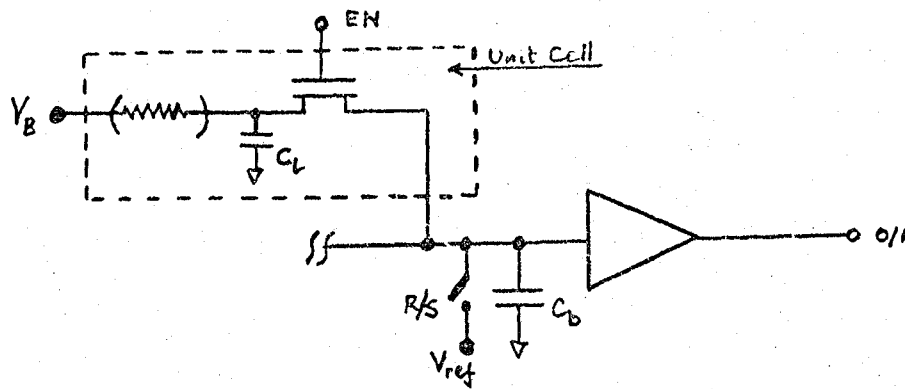


FIGURE 10 Direct Access MOS-Switch MUX

In its simplest form this scheme violates the general design principles enunciated in Section 3.3.1 above inasmuch as the readout capacitance which includes the total buss capacitance tends to be large, and is certainly larger than the integration capacitance. In this sense there is actually a gain loss during readout compared with the voltage developed on the integration capacitance.

Heller (Ref 16) has proposed modifications to the output buss, utilizing a saturated series transistor and precharge (as opposed to reset) switch. Constant voltage is maintained and a total transfer of charge is effected to a small output capacitance much in the manner of a bucket brigade circuit. Jespers et al. (Ref 17) have suggested adding a feedback loop to speed up the charge transfer. The modified circuit is shown in Figure 11a. An alternative solution is the use of a charge sensitive amplifier at the output as shown in Figure 11b where the (charge-to-voltage) gain is totally dependent upon the feedback capacitance.

The advantage of such schemes is that, with full charge transfer to a common readout capacitance, pattern noise (pixel-to-pixel response nonuniformity) is virtually eliminated, except for the non uniformity of the detector elements themselves. This is an important consideration in high speed video systems, but may be less germane to the situation of interest here where the data rates are slower and the inherent detector nonuniformity may be quite large (~ 10 to 20% perhaps). The disadvantage is that, though these alternative schemes modify

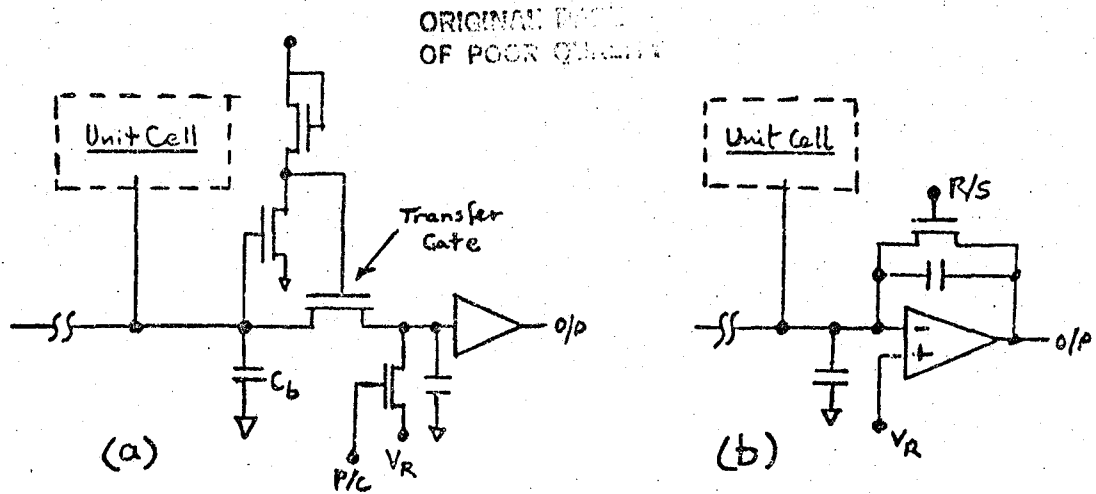


FIGURE 11 High Responsivity Output Stages for Direct Access MUX

the transfer function, they cannot improve upon the signal-to-noise characteristics of the basic circuit - and may well degrade it.

It is our premise that maximizing signal-to-noise ratio and optimizing ultimate system sensitivity should be paramount as design goals. Since the detectors are large and a hybrid linear array ensemble is contemplated space is not a primary issue. An alternative to direct access charge sensing is the use of individual buffer amplifiers as shown in Figure 12. This represents a substantial increase in pixel complexity and, through the threshold and capacitance variations of the individual buffer amplifiers, a source of increased

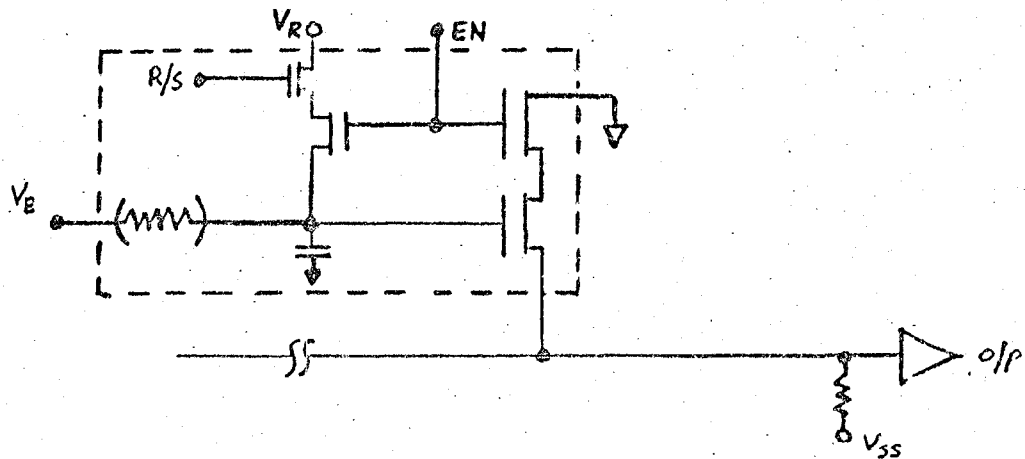


FIGURE 12 Buffered Access MOS-Switch MUX

pattern noise. Nevertheless readout capacitance is minimized, maximizing responsivity, and this type of circuit is potentially capable of a system noise limited performance below 100 rms electrons/sample. Though most of the actual circuits with which Aerojet has had experience have operated in the vicinity of 150 rms el/sample (albeit at data rates measured in Ksps per pixel) this type of circuit is presently believed to represent the state of the art in low-noise cryomultiplexing.

3.4 Application of Uniaxial Stress

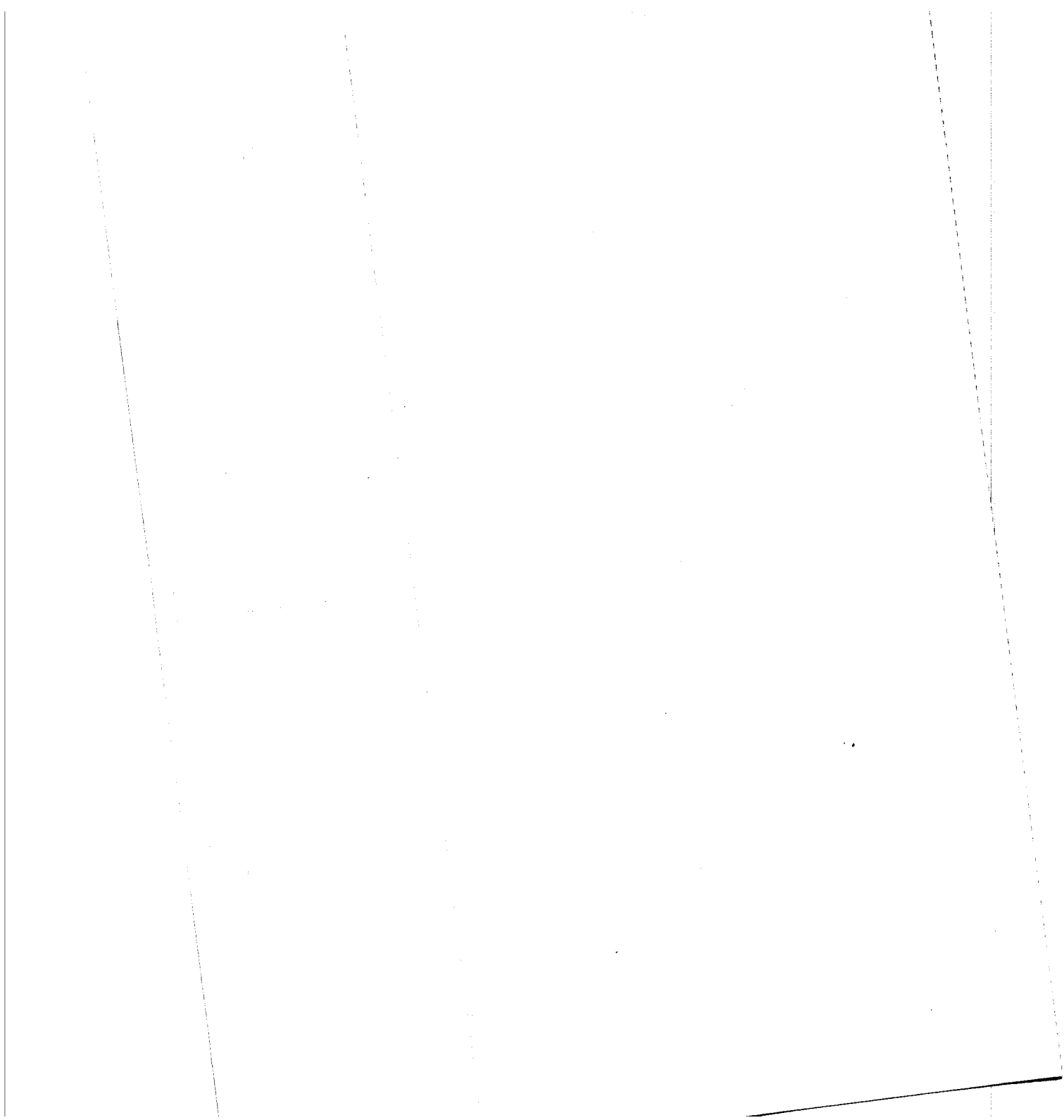
The spectral response of Ge:Ga can be extended beyond its normal long wavelength limit near 125 μm by application of uniaxial stress. Approximately 90 Kpsi is required to extend the long wavelength limit to 200 μm , stressing in the (100) direction having the greatest effect (Ref 5). Providing such a load in a stable reproducible manner at 2 K is certainly non trivial. Three general approaches for application of the 90,000 psi uniaxial stress were investigated:

- o Fabrication with materials which will differentially contract during cooling to provide the necessary force.
- o Incorporation of a spring component such that the detectors can be pre-stressed at room temperature to some level which will provide the necessary force when cooled to the operating temperature.
- o Inclusion of a mechanical ram for achieving the force.

Based on the study, this last method appears to be the most practicable means for satisfying the design objectives.

3.4.1 Thermally Induced Stress

In the first concept investigated the required force is developed by thermal contraction. Essentially, the array is mounted in a nest or frame where the fit in the direction of the applied force is held to extremely close tolerances. As the frame contracts during cooling to the 2 K operating temperature the detectors are stressed as required by differential contraction of the frame



with respect to the germanium. To enhance the effect on a given length of germanium a low thermal contraction shim might be added to the compressed column as shown in Figure 13. By selecting the frame and shim material, proportioning the geometry, and accurately determining the required fit, it would be possible to predict the applied force at the operating temperature to the extent that the thermo-mechanical properties of the materials are accurately known.

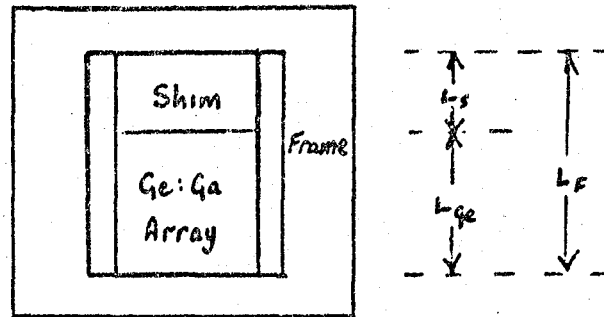


Figure 13: Stressing by Thermal Contraction

The advantage of this approach is its extreme simplicity and minimum of components. The disadvantages include the scarcity of potentially suitable frame and shim materials with appropriate values of expansion coefficient and Young's Modulus, and the extreme sensitivity of system effectiveness to the precision of the parts fabrication and to the detailed thermo-mechanical properties of the component materials which are imperfectly known at cryogenic temperatures.

Preliminary computations were performed for a variety of potentially suitable frame and shim materials to identify viable candidates and the dimensions of the structure necessary to develop the required loading. The analysis assumed that, for a frame sufficiently massive and hard that it is not subject to bending, brinelling, or other distortion,

$$\text{Contraction of Germanium} = \text{Contraction of Frame}$$

$$- \text{Contraction of Shim.}$$

The net contractions of the germanium and of the shim material are assumed to be the sums of their thermal contractions (ΔL) and their compressive strains

($\sigma L/E$) due to the stress σ developed in the stack. The net contraction of the frame by contrast is given by the difference between the thermal contraction and stress induced elongation. Thus we may write

$$\Delta L_{Ge} + \sigma L_{Ge}/E_{Ge} = \Delta L_F - \Delta L_s - \sigma (L_F/E_F + L_s/E_s)$$

and since the length of the frame L_F is just the sum of the germanium and shim we may recast this in the form

$$\frac{L_s}{L_{Ge}} = \frac{(\Delta L/L)_{Ge} - (\Delta L/L)_F + \sigma \left(\frac{1}{E_{Ge}} + \frac{1}{E_F} \right)}{(\Delta L/L)_F - (\Delta L/L)_s + \sigma \left(\frac{1}{E_s} - \frac{1}{E_F} \right)}$$

Inserting appropriate values for the stress (σ Kpsi) and for the thermal contractions ($\Delta L/L$ in/in) and Young's moduli (E) of the various materials, the size of shim (and frame) required can be estimated. Properties of some candidate materials are listed in Table 1.

TABLE 1 : PROPERTIES OF CANDIDATE STRUCTURAL MATERIALS

Material	Modulus of Elasticity in Tension E 10 ⁶ psi	Strain	Thermal Contraction $\frac{\Delta L}{L}$, mil/in			
			T = 300 K 350 K 400 K 450 K			
			T = 300 K	350 K	400 K	450 K
Germanium	15	6.00	.98	1.28	1.58	1.89
Tungsten	59	1.53	0.39	1.12	1.34	1.56
Beryllium	44	2.05	1.43	2.05	2.69	3.39
Nickel	30	3.00	2.40	3.08	3.81	4.55
CRES	29	3.10	3.56	4.22	5.12	5.96
Tantalum	27	3.33	1.35	1.70	2.05	2.39
Low Expansion						
Ni Alloys	24	3.75	0.12	0.14	0.17	0.29
Invar	21	4.29	0.12	0.14	0.17	0.29

Table 2 summarizes the shim size calculated to be necessary, for various combinations of shim and frame materials, to generate a 90 Kpsi stress in a 0.4 inch germanium stack (ten 40 mil detectors) at 3 K. Various assembly temperatures from 300K to 450K were considered. In deriving these results it was assumed

TABLE 2. Shim Size (In.) Required for 90 Kpsi Stress
in 0.4 Inch Germanium Stack

(a) For $\Delta T = 300$ K								
Shim	Frame	W	Be	Ni	ST.St	Ta	Ni Alloys	Invar
W		-1.27	-2.44	-1.02	1.38	-2.31	-1.82	-1.28
Be		-1.02	-1.18	-1.88	1.96	-1.15	-.88	-.88
Ni		-.58	-.61	-.68	-.85	-.61	-.56	-.56
CRES		-.46	-.46	-.48	-.51	-.45	-.45	-.45
Ta		-.69	-.74	-.89	-1.39	-.74	-.64	-.64
Low Exp. Ni Alloys		-.88	-.99	-1.38	-5.06	-.98	-.79	-.79
Invar		-.75	-.81	-1.01	-1.84	-.80	-.69	-.69

(b) For $\Delta T = 350$ K								
W		-1.74	-3.82	4.37	.91	-2.56	-1.22	-1.22
Be		-.89	-1.12	-1.84	11.87	-1.01	-.77	-.77
Ni		-.54	-.57	-.63	-.77	-.56	-.51	-.51
CRES		-.43	-.43	-.44	-.46	-.43	-.43	-.43
Ta		-.68	-.77	-.96	-1.76	-.73	-.62	-.62
Low Exp. Ni Alloys		-.96	-1.25	-2.32	4.32	-1.11	-.81	-.81
Invar		-.80	-.95	-1.39	-6.78	-.89	-.71	-.71

TABLE 2. (Continued)

(c) For $\Delta T = 400$ K

Shim	Frame	W	Be	Ni	ST.St	T	Ni Alloys	Invar
W		-1.76	-11.99	1.82	.53	-2.94	-1.17	-1.17
Be		-.79	-1.05	-1.84	3.12	-.90	-.69	-.69
Ni		-.49	-.52	-.57	-.70	-.51	-.48	-.48
CRES		-.39	-.39	-.39	-.39	-.39	-.39	-.39
Ta		-.67	-.80	-1.09	-4.55	-.72	-.61	-.61
Ni Alloys		-1.04	-1.75	-15.53	.99	-1.29	-.84	-.84
Invar		-.86	-1.22	-2.63	1.79	-1.00	-.74	-.74

(d) For $T = 450$ K

W		-1.78	.67	1.05	.34	-.34	-1.16	-1.16
Be		-.69	-.98	-1.72	1.87	-.79	-.63	-.63
Ni		-.46	-.48	-.51	-.61	-.47	-.45	-.45
CRES		-.37	-.36	-.35	-.33	-.36	-.37	-.37
Ta		-.66	-.86	-1.31	4.05	-.72	-.60	-.60
Ni Alloys		-1.10	-.31	3.01	.51	-1.45	-.86	-.86
Invar		-.90	-1.68	-51.20	.70	-1.10	-.76	-.76

that the frame would be designed with sufficient cross-section that strain in this member would not exceed 0.0002 inches - a slight modification of the above formulae.

Negative values indicate that the particular combination is inherently unsuitable. Only positive values - of which there are few - correspond to a potentially viable design choice. As can be seen the only window frame material for assembly at 300 K would be CRES with the shim material either tungsten or beryllium, though in either case the overall size is excessive. As the allowable temperature differential increases to $\Delta T = 450^{\circ}\text{C}$ other window frame materials can be used viz. nickel, beryllium, and the list of shim materials grows to include tungsten, beryllium, low expansion coefficient Ni alloys, and Invar. All these materials are capable of elastic behavior at stresses up to 90 Kpsi at 3 K (See NBS Monographs 13 and 63).

The disadvantage of this approach is the inability to absolutely predict differential contraction between the array and the array mount at the 2 to 3K operating temperature. Secondly, sizing of the array and frame to the accuracy required for the successful application of this method would be difficult. The mechanical simplicity of this approach makes it attractive but assembly into a practical working array could be difficult. The requirement for such large shims was disappointing, but could probably be accommodated.

Assembly at elevated temperature is considered impractical. However, the head of the frame could be attached to the legs with screws and the legs could be shorter than the germanium/shim stack so that a preload at room temperature could be applied. Joint shims could be included to allow for manufacturing tolerances. The separable frame would also facilitate the assembly operation. Modifications such as this do tend to compromise the simplicity of the package, however. If a portion of the force must be applied mechanically, then it seemed appropriate to apply the majority for the force as a preload. This reasoning led to consideration of the second and third methods.

3.4.2 Spring Loading

By application of the required force through the use of a spring member, it was hoped that the force could be applied at room temperature and that the spring constant could be selected such that the required force of about 1600 lbs

could be predicted by preloading to some lesser value at room temperature and allowing the contraction of the main frame during cooldown to provide the additional force required.

Two types of spring members were considered; Belleville spring washers and simple beam type flat springs. In both cases, it was quickly determined that development of the necessary force and deflection within a reasonable package size is not feasible.

In the case of a flat spring (e.g. Figure 16) the basic formulae are:

$$P = \frac{48 f EI}{L^3} \quad (\text{Simply supported beam with load applied at center}).$$

P = Load

f = Max deflection

E = Modulus of elasticity

I = Moment of inertia, $\frac{bt^3}{12}$ for rectangular beam of width b and thickness t

L = Length between supports

b = Width of beam

t = Thickness of beam

Solving the Beam Dimension:

$$\frac{bt^3}{L^3} = \frac{P}{4fE}$$

Similarly, the max stress in a simply supported beam with the load at the center is:

$$S = 1.5 FL / bt^2$$

so that

$$t = SL^2 / 6fE$$

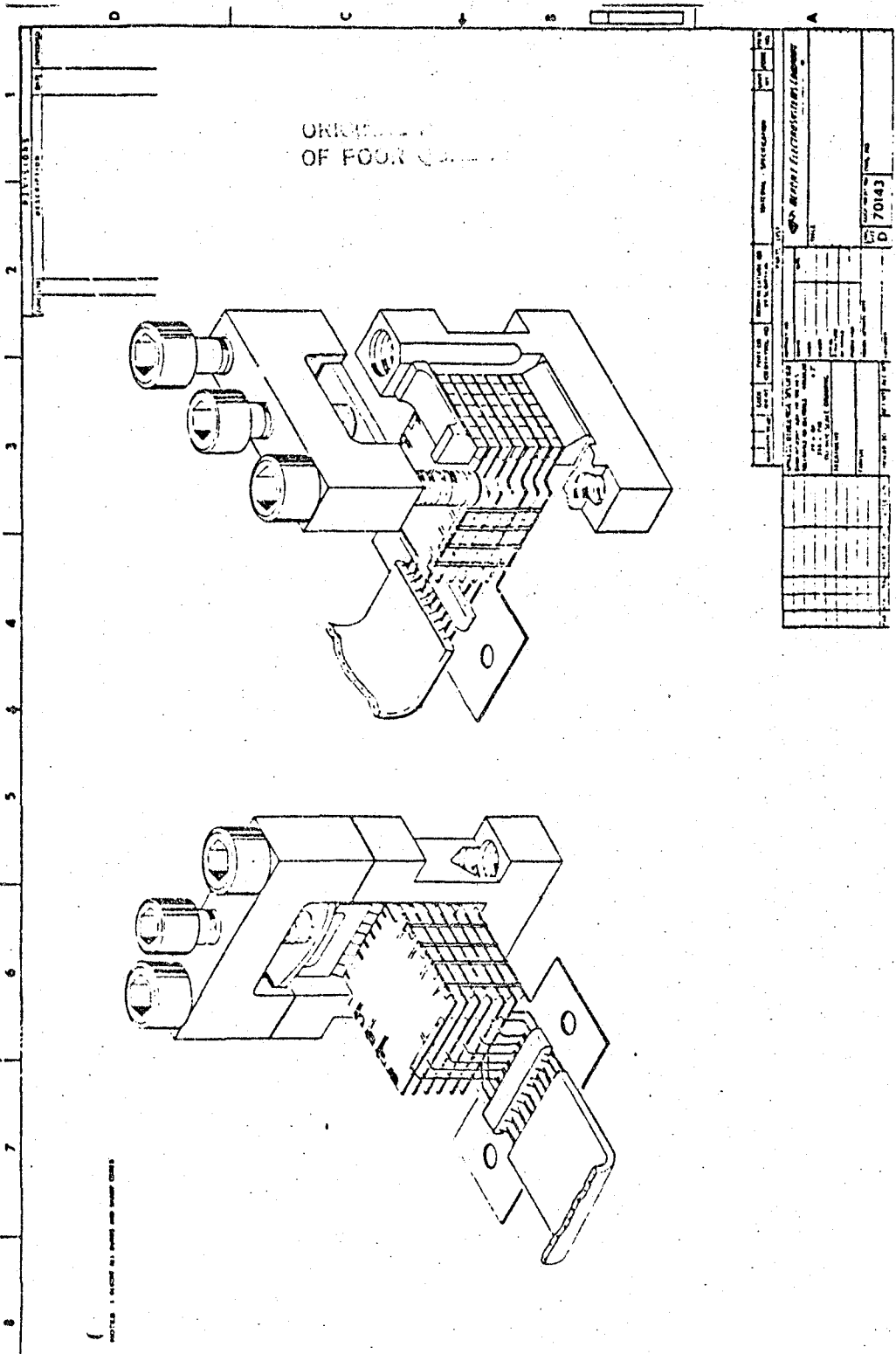


Figure 15 - Alternative Spring Loaded Ram Design Approach

Now, if practical values are substituted for L, S, f, and E,

$$L = 0.5, S_{\text{yield}} = 150,000 \text{ psi}, f = .024 \text{ and } E = 30 \times 10^6$$

We get the thickness $t = 0.087$ in. which is the maximum thickness of the beam without exceeding the yield stress. Using the value of t and substituting back in equation 2, we get the width b to be 1.05 inches.

Although the above values are assumed, they are reasonable. The maximum yield of 150,000 psi is probably higher than would be practical for a material that has to operate at 2 to 3 K. This value is approximately 80% of the ultimate strength of full hard 304 CRES at room temperature. The 300 series CRES can operate at the low temperature and the tensile strength increases as the temperature is lowered. A beam that is 1 inch wide and applying force on a .050 in. wide detector does not appear desirable. The beam could be divided into four leaves and stacked which would provide approximately the same load and stress value, but an uncertainty due to friction between the leaves would be introduced. Finally, these numbers were developed for a flexure distance of only .0024 in. A larger value would be desirable to take advantage of the spring rate of the beam since the 2.4 mils represents the amount germanium must deflect due to its own elasticity. Control of such a small deflection however, is not much easier than if no spring were present. Based on these considerations, a similar analysis using the Belleville washer approach was performed.

The analysis and design of a Belleville spring loading system is a good deal more complex than for a simple beam and requires a tedious trial and error type solution. A number of iterations were performed and it soon became apparent that a suitable washer could not be designed within practical size limits without parallel stacking. Stacking would theoretically increase the load in proportion to the number of washers used. However, it is reported by the Associated Spring Corporation that friction between the washers causes an apparent "hysteresis" in the load deflection curve which is of the order of 6% for each washer added. For a typical "off the shelf" Belleville, a 1 in. OD by 1/2 in. ID washer would provide a force of 540 lbs. to the flattened position. Thus, three washers could possibly be used in this application yielding a potential 18% uncertainty. In addition to the loading uncertainty, the packaging of a Belleville of this size such that its load is applied on a nominal 0.05 x 0.40 in.² detector stack would be cumbersome. Based on these considerations the

Belleville approach was also rejected as impractical. The 90 kip stress level requirement and the relatively small deflections which are necessary with either type of spring to limit spring stresses would appear to indicate that special spring components would not be practical and that the elasticity (Young's Modulus) can provide the necessary resilience.

The curves and equations which were used during the study have been reprinted in Appendix F. They were originally printed in a DESIGN HANDBOOK SPRINGS AND CUSTOM METAL PARTS published by the Associated Spring Corporation, Bristol, Conn.

3.4.3 Mechanical Ram Loading

The third (and recommended) approach investigated is to apply the pressure with a ram screw. Some rough estimates of the size required for the frame were made and the numbers appeared feasible. As stated previously, the elasticity of the germanium column of detectors would result in a shortening of the column by .0024 inches. If the frame material was made of Invar 36 and the two columns transmitting the load (~ 1600 lb) were square posts .2 in. on a side, a stretch of .0004 would result. Thus, a total excursion of the ram screw of .0026 in. would be required (not considering the elasticity of the screw). This value would require a very fine pitch in the ram screw which would not be practical. However, if the ram were made into a differential screw such that the lead of the screw is the difference of the two pitches, a practical system is possible. For this design, 32 x 33 threads per inch results in a lead of approximately .001 in. per revolution.

Invar 36 was selected for the housing because it has adequate yield strength, approximately 95,000 psi at room temperature and over 160,000 at the operating temperature, and because its thermal contraction is minimal between room temperature and liquid helium temperature. Contraction due to the cool-down will be about .0005 in. which can be taken into account during the preloading operation. The principal disadvantage of Invar is its weight. Other materials could be chosen with better strength to weight ratios, but the ductility at cryogenic temperature and the low thermal expansion coefficient were considered to be more important. During layout of the recommended package, material was removed where possible to reduce weight so that the completed assembly will weigh approximately 3 ounces less tape cables and connectors.

4. STRAWMAN DESIGN

Consideration of the principal design alternatives as discussed in Section 3 above has led to the conclusion that the FIR Ge:Ga mosaic array should be constructed as an ensemble of transverse biased linear subarrays, utilizing a MOS switch buffered access type of multiplexer and stressed as necessary by a preloaded screw ram. The design concept detailed below is specifically for a 7 x 7 pixel square array with approximately 0.04 inches square active areas on 0.045 inch centers for an 80% or greater fill factor. However because of its modular nature the design is readily extensible in either direction, the limits being set by the strength of structural materials, the size of suitably uniform Ge:Ga crystal material, and total thermal power dissipation.

4.1 Mechanical Assembly

The following thermo-mechanical design goals for the physical configuration of the array were established at the beginning of the design and trade-off study:

- The mechanical package must be capable stressing the detectors uniaxially to a value of 90,000 psi
- The array and electronics must operate at a temperature of 2 to 3 K with dissipation less than 100 μ W/channel during readout.
- A low impedance thermal path must be provided between the electronics portion of the package and the telescope cold station
- Construction materials must maintain suitable mechanical properties at the low operating temperature
- The array position must be maintained during cool-down and after repeated temperature cycles
- The array must be baffled to prevent stray energy from falling on the active detector areas
- Array electronics must be located as close as practical to the detectors to minimize coupling capacitance
- The detector electronics subassemblies should be capable of being tested at the subassembly level

- The array should be capable of disassembly for repair of replacement of components.
- The array frame should be able to accommodate a cold stop and or baffling and should not vignette when used with a fast optical system, say $f/1$ to $f/1.5$.

The mechanical design which was evolved is illustrated in Figure 17 and detailed in the group of drawings which comprise Appendix J. An interface with the telescope cold station was assumed which may or may not be realistic. However, the mounting can be modified during a detailed design without impacting the basic concepts offered here. The recommended approach employs a rigid frame with a pressure foot (beam) for application of the force. The force is applied to the foot by means of a differential ram screw. Preliminary calculations (see Appendix H) indicated that the method would be feasible and a more detailed examination of the mechanical and thermal loads was performed on the resultant design to confirm this. Stress calculations performed on certain portions of the design where excessive deformation was considered possible are included as Appendix H of this report.

A segmented transverse electrode configuration is preferred over any monolithic transparent-electrode mosaic concept. The choice of loading, however, can be either along a row (module) of detector elements or along a column, normal to the module axis. The latter was selected because it permits fabrication of the detector elements by cutting and polishing a rod, seven elements long (in this case), mounting it on the electronics substrate (a 0.005 inch sapphire board), and wire electro-discharge-machining (EDM) the slots required to separate the rod into individual detector elements. The configuration of a module is illustrated in Figure 18.

The detector rod, bias cut on one side and polished on four sides, is metalized with nickel on the bottom and gold on the top and assembled to the substrate by soldering with indium to vacuum deposited titanium/nickel pads on the sapphire. The attachments also serve as signal connections for the seven detectors. The interconnect traces on the substrate are also vacuum deposited except the material is titanium/gold. Ti/nickel pads are utilized where subsequent attachment with indium is required either because gold and many other metals form undesirable intermetallic compounds with indium or because indium soldering would be difficult. Ti/gold is used for the electrical interconnects

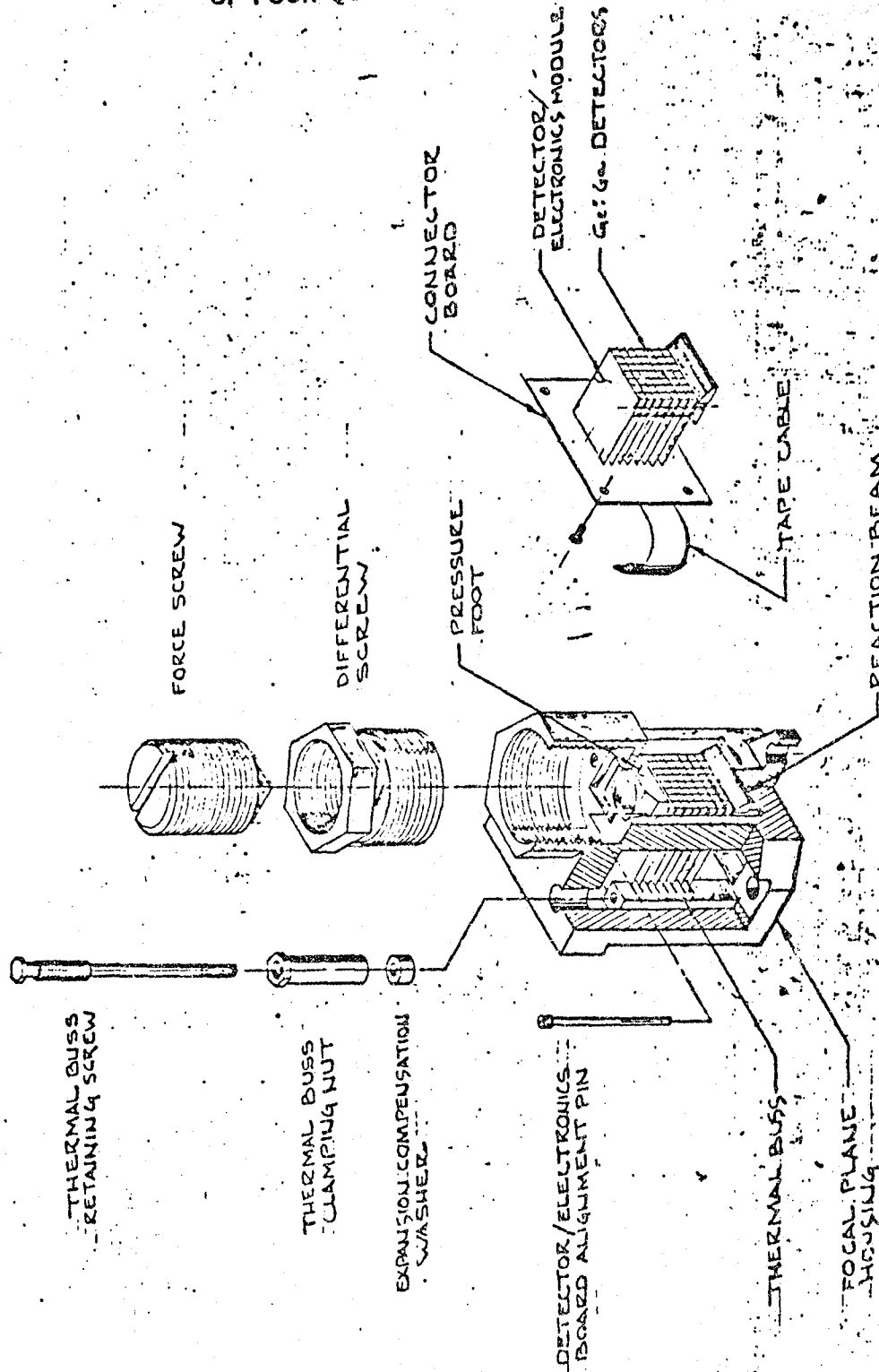


Figure 17 - Conceptual Design of Modular Stressed

Ge:Ga

ORIGINAL PAGE IS
OF POOR QUALITY

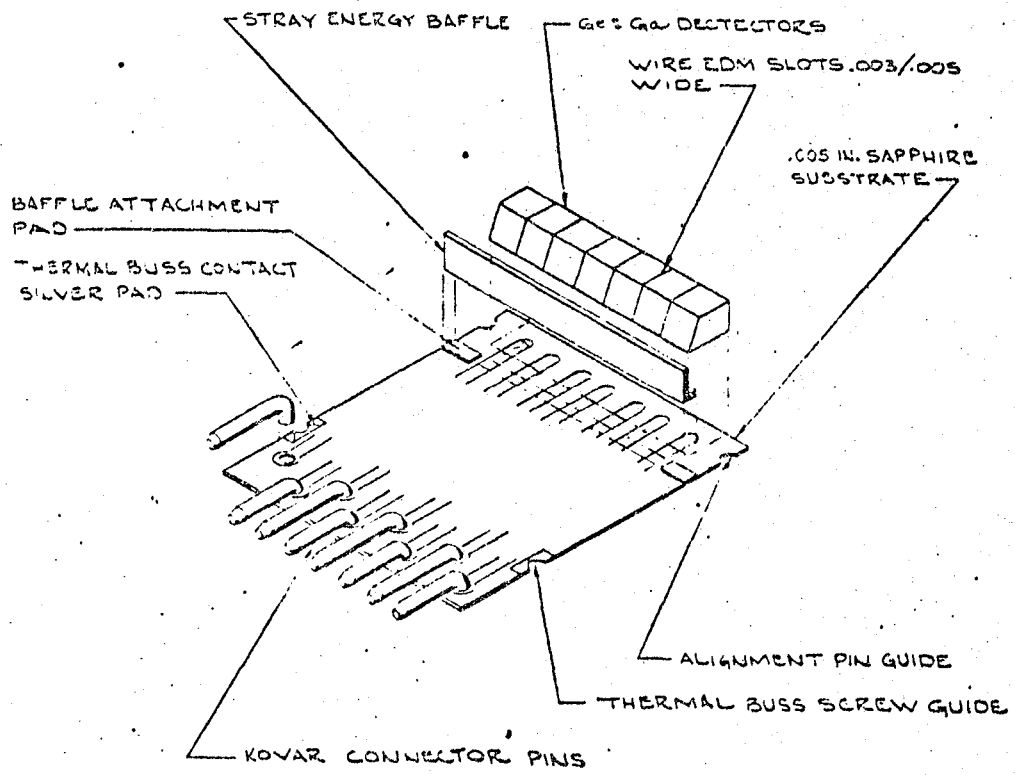


Figure 18 Linear Array Detector/Electronics Module Concept

to facilitate thermocompression or thermosonic bonding using gold wire between the devices and the substrate.

The bottom surface of each substrate is coated with Ti/Au followed by electroplated Au approximately .001 in. thick. This gold serves as a pressure pad to provide bias to the set of detectors located on the next board down in the stack. Electrical contact with the detectors (for bias) is accomplished by the 90 Kip stress when the boards are stacked because the force application is normal to the gold pad and compressed in the frame. By soldering the detectors on one side and making pressure contact on the other, the capability for disassembly is preserved.

Prior to assembly Kovar connector pins, positioned on .050 in. centers are furnace brazed onto the substrate as shown using copper/silver eutectic filler. During this operation, the pins are held precisely in position with a carbide fixture. The stray energy baffle should be made from alumina ceramic which has been metalized with Ti/Au on the surfaces facing the detectors and with Ti/Ni where the baffle is to be attached to the substrate using indium solder. Fixturing will be required during the soldering operations for both the detector installation and the baffle. Finally, the under surface of the substrate will be metalized and plated with .002 to .003 in. of silver to provide a low impedance thermal path from the heat generating electronic devices and external interconnects on the upper surface of the substrate to a collecting thermal buss which then attaches to the cold station.

Final assembly of the modules would involve attachment of the various multiplexer circuit chips using semi-cured epoxy film type adhesives to the substrate followed by stitching with .001 gold wire between the devices and the interconnecting traces which have been vacuum deposited on the boards.

The completed detector/electronics subassemblies would then be ready for testing with seven channels functioning and all of the circuitry accessible prior to assembly into the 49 element module. In addition to the seven detector/electronics subassemblies an eighth board will be incorporated containing the clocking and other array-common electronic functions. The mosaic would then be assembled by plugging the subassemblies into the inter-connect board/tape cable assembly, one at a time to complete the eight board module. Fixturing can be provided to engage in the alignment notches to ensure correct location of each board. The completed subassembly is then installed in the housing.

Figure 17 preceeding illustrates the assembly of the entire focal plane. The housing which includes the pressure frame is fabricated from Invar 36. The approximately 1600 lb. force on the detector array is applied by means of a differential screw bearing on a tungsten carbide faced pressure foot which in turn applies the force to the detector/electronics module stack. The reaction is from a tungsten carbide beam which in turn bears on the base of the frame.

Assembly consists of inserting Detector/Electronics Module into the housing from the rear with the pressure foot held in its proper position and attaching the connector board to the frame with four 0-80 pan head stainless steel screws. The Detector/Electronics Board Alignment Pins are then inserted in the housing such that the straight shank portion of the pins engage alignment notches in the sides of the electronic substrate boards and in the pressure foot. These pins provide array alignment and also prevent buckling of the column of detectors because the pin keys to both the housing and into the substrate and pressure foot notches.

The Force Screw is inserted so that the square end engages in the broached square hole in the housing. (The square prevents rotation when the differential screw is turned). A removable shim approximately .010 in. is then inserted between the pressure foot and the first board. The differential screw is then installed so that it simultaneously engages the threads on the housing and on the force screw.

The differential screw is similar in appearance to a pipe bushing. Its internal threads are .375-33 and the external threads are .500-32. Both threads are right hand and the pitch is selected such that a 360° rotation of the differential advances the force screw approximately 0.001 in net:

$$\text{External pitch} - \text{Internal Pitch} = \frac{1}{32} - \frac{1}{33} = .00095$$

During assembly the differential is engaged with the .010 in. shim in place. After engagement, the shim is removed and the force screw will begin to apply pressure after approximately 10 turns. The total number of threads on the differential OD is approximately 14 so that the last four turns will apply the force to the detector array. The housing design incorporates a hexagonal shape about the threaded section so that distortion will not occur during the pre-loading. During initial set up, it is expected that a load cell would be temporarily inserted in place of the detector module so that the actual force/torque or force/turns relationship can be established for the screw system.

The last item in the assembly will be the installation of the thermal buss. This element is fashioned with a row of slots which engage the electronic substrate boards and is machined from fine silver to provide maximum thermal conductivity. After it is slipped into position retaining screws are passed through holes in the busses to engage in notches in the substrates. The retaining screws are made of 303 CRES with a #1-72 thread at the bottom to engage in the housing. At the top a #3-56 Clamp Screw of 303 Cres is installed followed by a .096 in. long Invar 36 washer. The screw was sized to safely apply a pressure of 10,000 psi to the thermal pads on the substrates. Calculations (see Appendix G) indicate that a torque of 9 oz-in. on the clamping nut will provide the required 10,000 psi clamping pressure with a resulting stress in the screw of approximately 9000 psi. The expansion compensation washer was determined to be .096 in. long which adjusts the thermal contraction of the screw system to the contraction of the detector/electronics module. Thus, the clamping forces will be maintained from room temperature down to the array operating temperature. The other end of the thermal buss bolts directly to the telescope cold station to provide the least thermal resistance.

4.2 Thermal Conductivity Considerations

A thermal path to the cold station of the telescope which is independent of the focal plane housing is considered essential for this array because:

1. The heat sources are active devices which are located on the electronics substrates. Without such a direct thermal buss in this design the heat would be required to flow from the devices, through the sapphire to the germanium detectors, and even through up to six alternating layers of sapphire and germanium, a tungsten carbide anvil, an invar housing and finally through a bolted joint to the cold station. The unequal path lengths for the seven detector rows could result in large temperature differentials between detectors and unacceptably high temperatures for some of the elements.

2. The thermal conductivity of nickel-iron alloys is quite low.

Specific data was not located for the thermal conductivity of Invar 36, but representative conductivities for several other nickel alloys and the other array materials are listed below for comparison

<u>Material</u>	<u>Conductivity at 2 K to 4 K, Watt cm⁻¹ K⁻¹</u>
Monel	.009
3 & 7 CRES	.0025
Silver	3-100 (Depending on purity)
Sapphire	.15
Germanium	.05

As indicated, the resistance through the frame and through the germanium detectors would be poor, but conductivity from the device, through the sapphire, and through a silver buss would be excellent by comparison. Note however that in this temperature regime thermal conductivity values tend to be extremely dependent on material purity and temperature dependence is pronounced.

For the above reasons a silver conduction path is included between the sapphire boards and the heat sink. Silver is chosen because of its high thermal conductivity at 2-3 K and in order to achieve this high conductivity, the silver must be pure.

The conduction path consists of two parts. Each sapphire board is coated with .002 in. of silver on its underside. This coating picks up the heat dissipated on the board and conducts it over to one of two silver pedestals.

The pedestal accepts heat from all seven sapphire boards which fit into slots in the pedestal and are clamped into place. All contacting areas in this joint must be clean. The pedestal then conducts the heat received from the boards down into the heat sink.

The actual temperature difference achieved between detectors and the heat sink will depend on the purity of the silver and the cleanliness of the joints.

It is estimated that with a total maximum heat load on all eight sapphire boards of 80 milliwatts including conduction by the tape cables, the temperature difference can be kept below 0.1 K with this approach.

Of a 17 mW orbit average power dissipation budget at the 2K heat station of the SIRT/MIC, the cabling would consume less than 1 mW. A tape or collated cable of some 25 wires should be sufficient to access a 7 x 7 pixel array. (see Table 3 following for listing of electronic assignments). Though more difficult to work with than the more standard copper or constantan, nickel cables usually provide the best combination of thermal and electrical conductivity. Based on the data of Figure A (Curve #1) we would expect a thermal conductivity in the range of 0.5 to 0.8 W cm⁻¹ or lower for (impure) nickel wire or sheet in the 2K to 100K range. A 0.0012 inch diameter (or equivalent) conductor heat stationed at 80K would provide a maximum 16 μ W/ft⁻¹ load at 2K, or 0.2 mW for a two foot long by 25-conductor cable, with electrical resistance less than 0.1 ohms. A constantan cable of the same thermal conductance would exhibit an electrical resistance in excess of 500 Ω .

4.3 Electronic Design and Performance

The multiplexer unit cell shown in Figure 12 above (Section 3.3.3) can be implemented in a variety of ways ranging from a discrete MOSFET chip hybrid to a custom IC. Since most qualified manufacturers of infrared detectors now have ready access to custom - MOS capability Aerojet would recommend the latter course for flight hardware implementation. Use of commercially available chips would certainly be appropriate and more economical for preliminary technology demonstrations however.

Major design issues which must be resolved include the design, location and architecture of the multiplexer address and readout electronics and the magnitude of the integration capacitance.

4.3.1 Addressing Electronics

For an operational array the ensemble of multiplexer unit cells (e.g. as illustrated in Figure 12) must be accompanied by a suitable set of addressing electronics (often referred to as "scanning electronics") which will provide the proper sequence of ENABLE and RESET signals.

A multiplexer made up of unit cells as shown in Figure 12 requires addressed sequences of both ENABLE and RESET logic pulses. By providing an

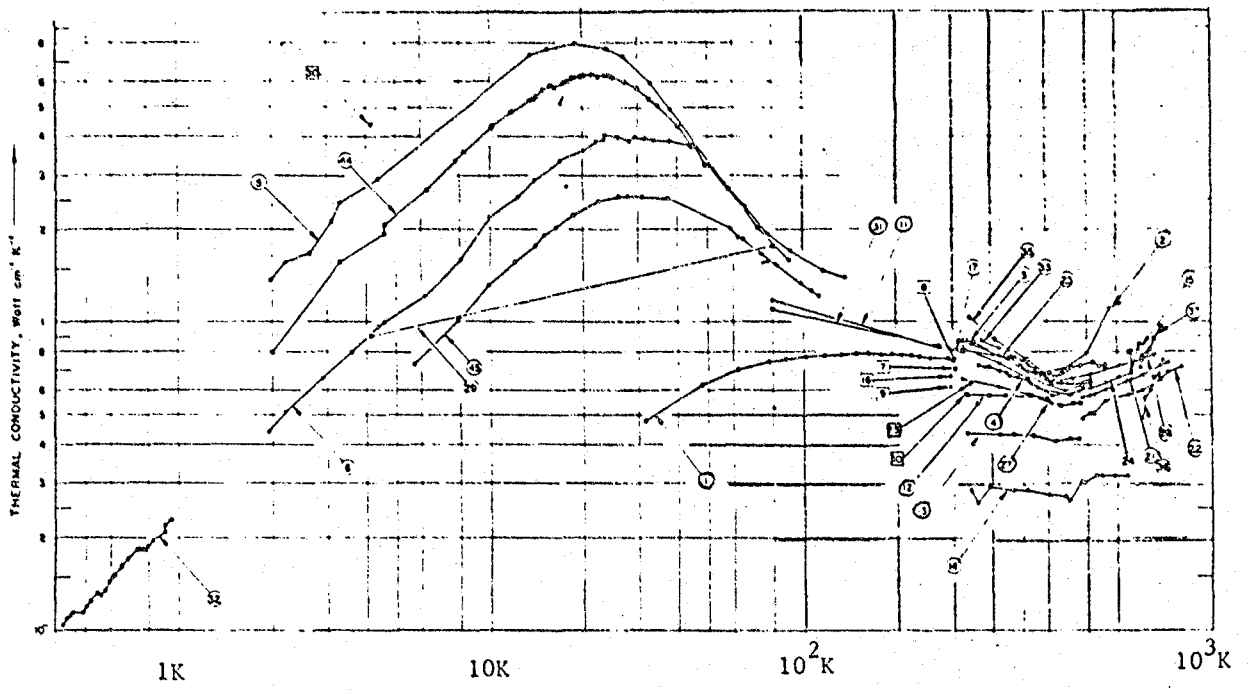


Figure 19 Thermal Conductivity of Nickel

RESET signal lines is eliminated, and a single RESET pulse train can suffice for the whole array. This revised unit cell is illustrated in Figure 20.

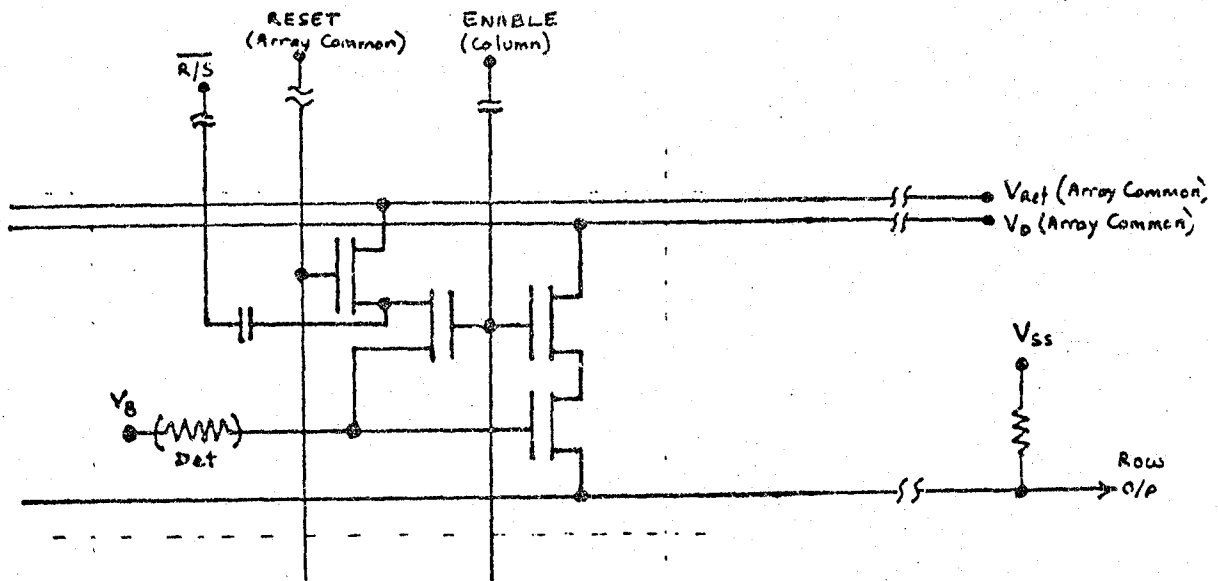


Figure 20. Proposed Multiplexer Unit Cell

The waveforms then required to operate the whole array are shown in Figure 21.

It is customary to generate these pulses using CMOS logic to conserve thermal power dissipation. Recent Aerojet measurements for two 74C193 CMOS counters and three 74C154 CMOS decoders totaled 15 mW operated at 5K and 50 KHz. The switching point (P-N device balance) of these ICs was virtually unaffected by cooling to cryogenic temperatures while the switching time - as measured by a ring oscillator stage delay - was reduced by about a factor of 3 by cooling. We conclude that CMOS can therefore be used fairly freely under cryogenic conditions.

On a monolithic two dimensional multiplexer, such as those used for large silicon detector arrays and HgCdTe hybrids for example, it is desirable to incorporate on-chip "scanners". In this case however, where a single linear array multiplexer will be provided on each board, provision of separate scanners for each would be thermally untenable, and it is therefore proposed that a single set of scanners be provided with output signals distributed to the individual array boards via the "mother" board.

ORIGINAL PROJECT
OF POOR QUALITY

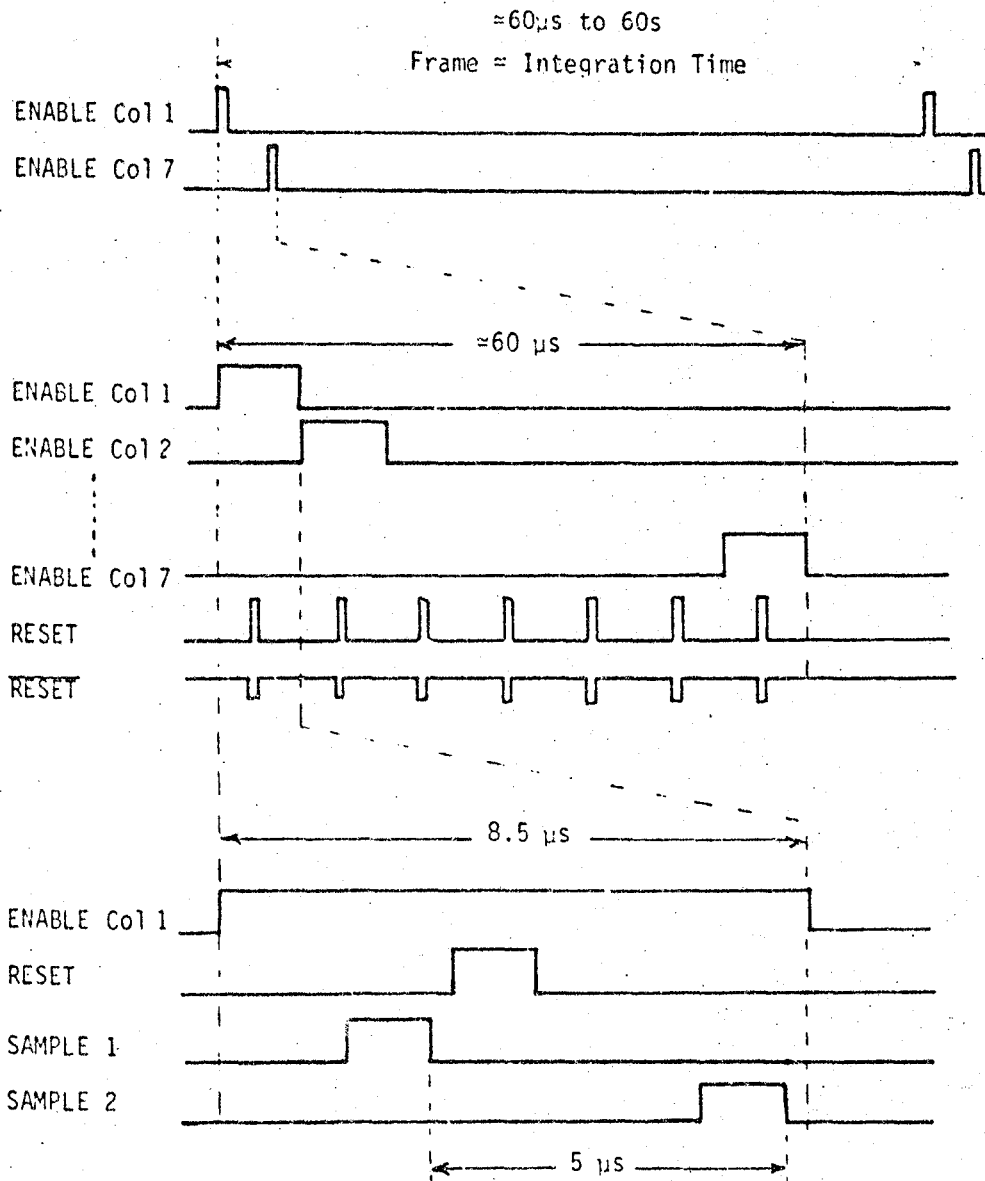


Figure 21. Waveforms Required to Drive Mosaic Multiplexer

The scanner circuitry could be mounted on a separate on-focal-plane board, located nearby at some intermediate cryo-cooled stage, or even incorporated in the external electronics. The interconnects required to operate arrays of 8 and 16 pixels per multiplexed channel are summarized in Table 3 for on- and off-focal-plane scanners. A binary decode type of on-focal-plane address logic has been assumed here since this permits external selected access of columns on an 'as required' basis. If random access is not necessary, then a shift register or counter/decoder system with a strobe for frame initializing would permit a further small reduction in lead count.

For modest sized arrays of 8^2 to 16^2 elements (say) the number of extra leads required for off-focal-plane location of the scanners is not large. The small increase in thermal load from the additional cabling (say 0.1 mW) is certainly preferred to the several mW power dissipation of typical low power CMOS counter or decoder chips if operated continuously in standby or at low clock rates. In the case of a low duty-cycle system, turned on only during a small fraction of the orbit, or using burst readout at low frame rates, the orbit average of the scanner's dissipation would decrease and the tradeoff equation could be reversed. For logistical convenience however, external electronics is certainly recommended where feasible.

4.3.2 Multiplexer Charge Integration Capacity

In a monolithic custom IC multiplexer with bump bonded monolithic detectors it is possible to reduce the node integration capacitance to the vicinity of 0.2 pf without making component devices so small that source follower g_m or switch on-state conductance becomes an issue. However in the proposed Ge:Ga structure it is inevitable that the large detector (~ 0.3 pf) and interconnect pattern(s) on the circuit board (≥ 0.1 pf say) will increase the minimum achievable capacitance, probably to more than 0.5 pf.

The maximum detector bias for Ge:Ga is of the order of 2 to 5 V/cm or 0.2 to 0.5 volts for the proposed 0.04 inch square device size. Higher bias fields induce excess dark currents and noise due to impact ionization of the easily ionized gallium doping. Significant non-linearity will result from debiasing the detectors if the integrated photo-current causes the node voltage excursion to approach saturation at the detector bias. For design purposes a 50 mV upper limit is proposed (10 to 20% of the bias) allowing the accumulation of up to 2.5×10^{-14} amp-seconds (1.5×10^5 electrons)

Table 3 Interconnects Required for Array Operation

	On Focal Plane Scanner		Off-Focal Plane Scanner	
	8 X N	16 X N	8 X N	16 X N
Output Channels	N	N	N	N
Interdigitated Grounds	N	N	N	N
RESET Pulse	1	1	1	1
<u>RESET</u> Pulse	1	1	1	1
Reset Reference	1	1	1	1
Det. Bias	1	1	1	1
Drain Supply	1	1	1	1
Address Code	3*	4*	-	-
ENABLE	-	-	8	16
Scanner Supply	3	3	-	-
Temp. Sensor	2	2	2	2
Total	13+2N	14+2N	15+2N	23+2N

* Could be reduced to 2 (a strobe and clock) if random access to array columns is not required.

on the minimum 0.5 pf capacitance. Assuming a modest detector responsivity in the vicinity of 5 A/W (see Figure 1 and also Appendix A), or 0.06 electrons per photon at 100 μm , this represents an upper limit on the order of 2×10^6 photons/sample for the dynamic range or approximately 4 seconds integration at the 5×10^5 ph/pixel/sec maximum anticipated background flux. At longer integration times, or higher backgrounds the response would tend to become excessively non-linear as the system saturated, though it should in principle remain calibratable. Linear dynamic range could be extended by adding node capacitance but only at the expense of increasing system noise.

Note that linear dynamic range cannot be increased by decreasing detector bias unless response is itself superlinearly dependent on bias.

4.3.3 Multiplexer Noise and Data Rates

Two noise sources in the multiplexer set the basic lower limit on detection sensitivity. These are the reset kTC noise and the wideband noise of the output source-follower which is double sampled in the external signal processing. Other possible multiplexer noise sources are random timing fluctuations which introduce small variations in the integration or reset intervals, and power supply variations which can cause clock and logic pulse amplitude variations. The latter can effect system noise when inserted into the signal channel by capacitive coupling.

Aerojet [Ref 18] has measured the noise and operating characteristics of typical PMOS transistors at temperatures down to less than 3K. Under these lowest temperature conditions noise was within a factor of two of that measured at more conventional cryo-MOSFET temperatures (8-16K say). For the M104 test sample for example, which is representative of moderately good quality cryo-PMOS (though not the ultimate state of the art), the noise spectrum was dominated by low frequencies by a $1/f$ component of the approximate form

$$n_{1/f}(f) \simeq Kf^{-1/2} \text{ rms } \mu\text{V}/\sqrt{\text{Hz}}$$

where

$$K = 2.5$$

At high frequencies this merges into a white noise component of amplitude approximately

$$n_w \sim 15 \text{ to } 20 \text{ nV}/\sqrt{\text{Hz}}$$



To the white noise of the MOSFET we must also add the noise (presumed white) of the signal processing pre-sampling circuits. The system bandwidth will be limited at some frequency f_a by the sampling electronics.

Referring to the noise model of Section 3.3.1 above the rms output noise of a unity gain double sampling system of differential delay τ , and with these MOSFET noise components as input, is of the form

$$v_u^2 = \int_0^{\infty} (k^2 f^{-1} + n_w^2) (2 \sin \pi f_a \tau)^2 (1 + f^2/f_a^2)^{-1} df$$

where the second and third terms are the effective transfer functions of the double sampling and bandwidth limiting circuits elements respectively. The noise equation may be recast in the form

$$v_u^2 = 4k^2 \int_0^{\infty} \frac{\sin^2(ax/2)}{x(1+x^2)} dx + 4f_a n_w^2 \int_0^{\infty} \frac{\sin^2(ax/2)}{(1+x^2)} dx$$

where the dimensionless parameter $a = 2\pi f_a \tau$ on which the $1/f$ term depends is the differential delay τ expressed as a number of system response time constants. Clearly response will be attenuated (and sensitive to timing errors) unless a is large enough that the system can respond completely to the reset operation at the input.

These integrals are solvable in the form [Ref 19]

$$v_u^2 = k^2 \left\{ e^a E_1(a) - e^{-a} Ei(a) + 2 \log a + 2\gamma \right\} + \pi f_a n_w^2 (1 - e^{-a/4})$$

where γ ($= 0.5772\dots$) is the Euler-Mascheroni constant and $E_1(x)$ and $Ei(x)$ are the standard exponential integral functions. These functions may be evaluated from tabulations (e.g. Ref. 20) or, for large values of a , by using the asymptotic expansions yielding

$$v_u^2 = 2k^2 \left\{ \gamma + \log a - \sum_{m=1}^{m \leq a/2} (2m-1)!/a^{2m} \right\} + \pi f_a n_w^2 (1 - e^{-a/4})$$

For a = 2 the rms value of the 1/f noise term is 1.49K while for a = 4 to 20 it climbs slowly from 1.94 to 2.67. Since the measured signal response will vary as $(1-e^{-a})$ a value near a = 2 would be optimum in the absence of the white noise term and neglecting the noise impact of random errors in the value of τ . In practise a somewhat higher value is probably preferred to ensure settling after reset.

Based on the M104 data a total 1/f noise of the order of 5 rms μ V should be observed for a \approx 4. For the M104 with a capacitance near 0.8 pf, the 1/f term would be equivalent to an rms noise integration sample as small as

$$\delta q_{1/f} \approx \frac{(5 \times 10^{-6})(8 \times 10^{-13})}{(1.6 \times 10^{-19})} = 25 \text{ rms el/sample}$$

In a custom multiplexer with lower capacitance the noise will likely be greater. A rule of thumb used at AESC to predict probable noise levels for a FET technology is that $KC^{3/2}$ is constant and for a smaller 0.2 pf device (0.5 pf total) we might expect up to 50 e/s from the 1/f term. The "white" noise component, including contributions from the signal processing electronics, will generate an equivalent sample noise of the form

$$\delta q_w = \frac{C n_w}{1.6 \times 10^{-19}} \sqrt{\pi f_a (1 - e^{-a/4})}$$

which for a = 4, c = 0.5 pf and $n_w = 20 \text{ nV}/\sqrt{\text{Hz}}$ is approximately

$$\delta q_w \approx 0.1 \sqrt{f_a} \approx 0.08 \sqrt{\tau^{-1}} \text{ rms el/sample}$$

For a $\tau = 5 \mu\text{sec}$ sample delay time (requiring a system bandwidth $f_a = 130 \text{ KHz}$ for a = 4) white noise sources will contribute approximately 25 rms electrons to the sampling noise. The contribution is already small and there is therefore no compelling reason to attempt to use longer values of correlation delay in order to reduce f_a . Note that the 1/f component depends only on the relative value (a) and not on the absolute values of f_a and τ .

Substantially longer values of delay time may unnecessarily complicate the design of the sample-and-hold circuitry. Shorter delay times requiring faster response bandwidth would not only tend to increase the white noise contribution unnecessarily, but would also increase the line-driving

capability required of the multiplexer. A 50 to 100 pf cable capacitance is likely and for a typical 2 to 3 Kohm multiplexer cell output impedance (1/gm) achieving better than 1 MHz bandwidth would require additional on-focal plane line-drivers and their attendant power dissipation. In the SIRT application where overall data rates are low there is no compelling reason to stress this design area.

The KTC or reset noise originates in the Johnson noise of the resistance of the reset circuit. The temperature T in the reset noise equation

$$\delta q_r = \sqrt{kTC} / e$$

therefore refers to the effective channel temperature in the reset MOSFET switch which will clearly be greater than the nominal focal plane temperature. Guessing at an effective value of T in the 10 to 20 K range we would expect the reset noise contribution to be of order

$$\delta q_r \approx 50 \text{ to } 75 \text{ rms electrons}$$

The total noise from fundamentally unavoidable noise sources will be of order

$$\delta q = \sqrt{\delta q_{1/f}^2 + \delta q_w^2 + \delta q_r^2} \sim 90 \text{ rms el./sample}$$

This is well within the design objective derived in Section 2 (Figure 1). Note that these noise sources are independent of sampling rate. Additional noise sources may be manifest however, depending on the system design and operational details. Random timing errors and power supply stability are clearly potential contributors.

Unless grossly awry, timing drift will show up as noise only to the extent that integrated flux is present and will thus be akin to g-r noise except that it will be directly proportional to integrated flux rather than to its square root. Timing error contributions can arise from varying integration intervals and from varying correlation delay in the sampling circuits.

At the highest background levels (5×10^5 p/sec/pixel) and at the nominal 5 frames per second address rate the total integrated photon count is 10^5 per sample and since the quantum yield of a typical Ge:Ga detector (5 A/W at 100 μ m say) is not likely to be much better than 6% of the stored charge

will be greater than 10^4 electrons/sample. A 0.1% clock and timing stability which should be readily achievable would ensure that contributions from this source remain negligible compared with g-r and system noise even at extended integration times.

The sample amplitude measured after a delay of (a) system response time constants after reset is a fraction $(1 - e^{-a})$ of the full value. If clock or one-shot delay instabilities cause the value of (a) to fluctuate an apparent noise source will be generated. Similarly as for integration interval errors we would wish to keep the effective signal fluctuations to less than 0.1% - that is

$$\frac{\delta S}{S} = \frac{e^{-a} \delta a}{(1 - e^{-a})} \leq 10^{-3}$$

For large values of a this reduces to a requirement

$$\delta a \leq 10^{0.43 a - 3}$$

For a nominal value $a = 4$ δa must be no greater than 1/20 implying approximately 1% stability in the delay interval. At $a = 5$ the requirement is relaxed to about 7%.

5 CONCLUSIONS AND RECOMMENDATIONS

We have concluded, as a result of this study, that physically an optimum mosaic design for Ge:Ga detectors must differ substantially from the approaches currently in vogue for extrinsic silicon devices, but that stressed Ge:Ga mosaic arrays of several hundred pixels are feasible. A design consisting of stacked linear array modules, laterally biased is preferred for Ge:Ga to provide optimum responsivity, to control crosstalk, and to permit uniaxial stressing of the detectors to extend long wavelength spectral coverage. Electrically however the switched MOSFET multiplexer used for large silicon on silicon hybrid arrays remains the preferred readout method for Ge:Ga detectors. The modular array architecture of the latter renders the efficiency of on focal plane address scanners doubtful. For arrays up to 16^2 elements off focal plane scanners will be preferred.

A drawing package for a 7 x 7 element version of the design is attached as Appendix J, and the important design and performance parameters are summarized in Table 4. Such an array should be capable of meeting all of the established performance requirements.

In arriving at this point design concept certain assumptions and/or extrapolations were made that should certainly be substantiated by measurements prior to committing to a detailed focal plane design. Among the most important of these are

- The bevelling of detector to promote internal reflection and quantum efficiency enhancement
- Intermittent activation for burst readout of the array at very low frame rates and temperatures.

Additionally certain design concepts were rejected, or excluded a priori on the basis that the underlying technologies were not sufficiently developed that reduction of the concepts to practise could be anticipated with any assurance. Among the technologies in which progress should be monitored for potential impact in opening up new alternative design approaches we may identify

TABLE 4: CONFIGURATION AND PERFORMANCE SUMMARY

<p>ARRAY CONFIGURATION</p> <ul style="list-style-type: none"> • Array Size • Pixel (Detector) Size • Stress Loading • Electrical Interface • Thermal Interface 	<p>Stacked Linear Arrays</p> <p>7 x 7 pixels on 0.045 inch centers</p> <p>0.040 inch x 0.040 inch (80% fill)</p> <p>Preload Ram Screw</p> <p>32-pin Connector terminating 30 x 0.00125 in \varnothing x 24 in (or TBD)</p> <p>Nickel Collated Cable</p> <p>TBD inch² at $\leq 2.4K$</p>
<p>DETECTOR CONFIGURATION</p> <ul style="list-style-type: none"> • Material • Doping Density • Counterdoping • Absorption Length 	<p>Lateral Bias Extrinsic Photoconductor</p> <p>p-type Gallium Doped Germanium (Ge:Ga)</p> <p>2×10^{14} to 3×10^{14} Ga/cm³</p> <p>10^{11} ($\pm 30\%$) N/cm³</p> <p>2mm with 18° Bevel</p>
<p>MULTIPLEXER CONFIGURATION</p> <ul style="list-style-type: none"> • Address Scanners • Output Channels • Node Capacitance • S/F MOSFET • EN MOSFET • R/S, R/S EN MOSFET 	<p>Switched PMOS Source Followers</p> <p>CMOS External</p> <p>7 (7 pixels/channel)</p> <p>0.5pf to 0.8pf (incl. MUX 0.2pf, Det 0.3pf)</p> <p>$V_{th} \approx V_{ds} \leq 5V$, $I_{ds} \sim 100\mu A$, $g_m \geq 300\mu S$</p> <p>$R_{ON} \leq 10^3$ ohms, $R_{OFF} \geq 10^{14}$ ohms, $V_{th} \approx 2V$</p> <p>$R_{ON} \leq 10^5$ ohms, $R_{OFF} \geq 10^{14}$ ohms, $V_{th} \approx 2V$</p>
<p>OPERATING REQUIREMENTS</p> <ul style="list-style-type: none"> • Array Temperature • Scanner Voltages • Detector Bias • Drain Supply • Reset Reference Voltage • Frame Timing Instability & Drift • Sample Correlation Time 	<p>$\leq 2.5K$ at Detectors, $\leq 2.4K$ at thermal sink</p> <p>+3V/-5V</p> <p>Variable 200 to 500mV</p> <p>0V</p> <p>Variable -0.2 to +0.2V</p> <p>$\leq 0.1\%$</p> <p>5 μS $\pm 50nS$</p> <p style="margin-left: 150px;">} 1% Reg. low freq & $\leq 10\mu V \sqrt{Hz}$ at $f \geq 30 KHz$</p>

TABLE 4: ARRAY CONFIGURATION & PERFORMANCE SUMMARY (Cont.)

PERFORMANCE	
o NEP (λ_{\max}) - Broadband - Low $f \ll f_s$	$\leq 8 \times 10^{-18} f_s$ rms Watts $\leq 1.1 \times 10^{-17} \sqrt{f_s}$ rms $W/\sqrt{\text{Hz}}$
o Wavelength Range	40-120 μm (to 200 μm with 90 Kpsi loading)
o Detector Dark Resistance	$\geq 10^{14} \Omega$ (design goal at 2.5K)
o Responsivity (Peak)	$\geq 4 \text{ A/W}$
- Gain (ac & dc)	$\geq 20\%$ } $\eta G \geq 0.05 \text{ el/photon}$
- Quantum Efficiency (In Band)	$\geq 25\%$ }
o Multiplexer Noise (wideband)	≤ 200 rms el/sample ($\sim 4 \times 10^3 \text{ ph}$)
o Maximum Linear (5%) Signal	1.5×10^5 el/sample ($\sim 3 \times 10^3 \text{ ph}$)
o Dynamic Range (max S/N)	$\sim 10^3$
o Minimum Frame Time	60 μsecs approx. ($f_s \leq 1.6 \text{ k}\mu\text{s}$)
o Maximum Frame Time (for 10% of saturation)	Depends on Flux but $\geq 5 \dots$ design goal for dark resistance limited system
o Crosstalk - Optical	$\leq 1\%$
o Crosstalk - Electronic	$\leq 3\%$
o Thermal Power Dissipation	
- Cables	$\leq 1 \text{ mW}$
- Mux Cells	$7 \times 500 \mu\text{w} = 3.5 \text{ mW}$ during readout only
- Scanner	Off Focal Plane
o Weight Excluding Tape Cables	3 oz. approx.

- low temperature CCD multiplexers in alternative materials such as GaAs.
- Impurity band versions of Ge:Ga, Ge:Sb or Ge:B detectors and epitaxial growth of germanium by CVD or MBE methods.



6 REFERENCES

1. Shuttle Infrared Telescope Facility Phase A Concept Description, AMES Research Center, August 28, 1981.
2. NASA Statement of Work (PR SPT-2459) Dec. 4, 1979
3. P. R. Bratt, N. N. Lewis, R. L. Nielsen, Ge:Ga and Ge:Be Photoconductive Detectors for FIR Astronomy from a Space Platform SP 2 Symposium on Utilization of Infrared Detectors, Jan. 17 and 18, 1972 at Los Angeles, Calif.
4. C. M. Parry and J. B. Parkinson, Hardened Detectors/Circuits Study Volume I - Hardened Infrared Line Scanner Focal Plane Technology Final Technical Report, Contract DASG60-75-C-0032/P00042 Oct. 1976 (SECRET).
5. A. Kasanskii et al. Solid State Commun. 24 (1977) p 603.
6. D. H. Dickey and J. D. Dimmock J. Phys. Chem. Solids, 28 pp 529-542 (1967).
7. e.g. M. Garbury, Optical Physics, NY Academic Press, 1965 pp 418-421.
8. E. E. Haller, N. M. Haegel, W. L. Hansen and P. N. Burke, Ge:Ga Far Infrared Photo-conductors. Final Report for Period July 1, 1981 to Nov. 30, 1982, NASA Contract No. W-12, 606.
9. D. K. Schroeder et al., IEEE J. Solid State Circuits, SC-13 (Feb. 78) p. 180.
11. C. M. Parry et al., Hardened Mosaic Technology Study - VI Mosaic Device Development, Final Technical Report, Contract DASG60-77-C-0032/P0003, Sept. 1978 (SECRET).
12. C. R. McCreight and J. H. Goebel, Applied Optics 20, p 3189 (1981)
14. C. M. Parry Coded Bias Mosaics. Paper presented at SPIE Symposium, Washington (April 1980).
15. See for example: Charge Coupled Devices & Systems (M. J. Howes and D. V. Morgan, Ed.) Wiley 1979.

(Sept. 1975).

17. P. G. A. Jespers et al., IEEE J. Solid-State Circuits, Vol. SC-12, p 232 (1977).
18. Cryogenic Switched MOSFET Characterization - Aerojet ElectroSystems Co. Final Report #7165 prepared for NASA AMES under PO A80598B (JMM) (March 1981).
19. Integral solved by A. F. Schrey in 1978 and documented anonymously in C. M. Parry and J. B. Parkinson, Hardened Mosaic Technology Study, Vol. 1, Appendix A; AESC Report 5715, 29 September 1978. (Secret. Appendix A is unclassified). An apparently similar solution is derived in unevaluated integral form by R. J. Kansy IEEE J. Solid State Circuits, Vol. SC-15, 373 (1980).
20. M. Abramowitz and I. A. Stegun, Handbook of Mathematical Functions; NBS AMS-55 (1964), Table 5.1 and 5.2.

APPENDIX A

ANALYTICAL DESCRIPTION OF Ge:Ga PHOTORESPONSE

The literature on Ge:Ga, particularly as it pertains to its performance as an infrared detector, is both fragmented and frequently in apparent conflict. With very few exceptions reported measurements on any given device are extremely limited in scope and in many cases test conditions have been incompletely defined. A similar situation existed in the late 60s for the shorter wavelength Ge:Cu, Ge:Cd and Ge:Hg devices and the then nascent extrinsic silicon materials.

A theoretical and semi-empirical modelling framework has subsequently evolved by which the performance of the latter can be accurately described over a wide range of operating conditions and detector geometries, and resolving most of the apparent discrepancies. Though developed at about the same time that the germanium devices were being almost totally superseded by silicon it has nevertheless been observed that the same general framework applies in both cases. In fact the crucially important first identification of secondary time constant response phenomena with the internal space charge relaxation mechanism was made by R. L. Williams (A9) in connection with Ge:Hg.

Aerojet has attempted to analyze the available photodetector data for Ge:Ga within the framework of the silicon electro-optical performance model, resolving many of the apparent discrepancies in the data base in the process. Based upon this analysis parametric models of detector performance as a function of device geometry, and doping and counterdoping concentrations has been performed, leading to recommended configurations and value ranges for these key parameters.

A1. Optical Performance

The optical performance of low-background Ge:Ga can be described well analytically.

The optical cross section of gallium dopant in germanium is well described by

$$\sigma(\lambda) \propto \lambda^{8/3} (\lambda_c - \lambda)^{1/4} \quad (1)$$

where σ is the optical cross section (cm^2/atom)

λ is the wavelength

λ_c is the cutoff wavelength (determined by the energy level)

(This form is characteristic of As and Bi in silicon, but it is not a universal law.) For $\lambda_c = 125 \mu\text{m}$ and a peak cross section of $\sigma_{pk} = 9 \times 10^{-15} \text{cm}^2$ at $115 \mu\text{m}$, proportionality (1) yields optical cross sections from $50 \mu\text{m}$ to peak that are within 12% of those given in the Statement of Work (PR SPT-2459, Dec. 4, 1979).* Also, at $8.3 \mu\text{m}$ proportionality (1) predicts $1.5 \times 10^{-17} \text{cm}^2$, which compares favorably with $2 \times 10^{-17} \text{cm}^2$ (0.02cm^{-1} for $10^{15} \text{Ga}/\text{cm}^3$) measured at 77°K by Newman and Tyler (Phys. Rev. 105, p. 885-886, Feb. 1, 1957). Therefore, it appears we have a good description of the optical absorption properties of Ge:Ga.

Quantum efficiencies summarized in Table AI computed with the Aerojet analytical model (assuming $\lambda = 95 \mu\text{m}$) usually agree well with measured values reported by Haller, Hansen, and Hubbard (A4) (which measurements were close to $95 \mu\text{m}$, except where stated, though they do not report wavelength).

The analytical model for quantum efficiency, including such related considerations as optical crosstalk and the effect of inducing total internal reflections to substitute for placing the detector in an integrating cavity, are described in detail in Appendix B following.

*Some semiempirical extrapolations from doped-silicon technology suggest the peak cross section for a p-type dopant with $\lambda_c = 125 \mu\text{m}$ in germanium should be around $\sigma_{pk} \sim 10^{-14} \text{cm}^2$.

Table AI-Comparison of Measured and Calculated Quantum Efficiency

<u>Detector</u>	<u>Measured Q. E.</u>	<u>Calculated Q. E.</u>
LBL 583-4.8	Not reported	12.9 (3.4 at 51 μm)
LBL 108-8.2	~ 4 (25%**)	3.2 (64 μm)
LBL 108-8.2	7.5 (8.5**)	7.2
LBL 112-15.8	~ 50	29.1
LBL 112-18.0	25	32.1
LBL 112-21.0	23	21.7
Hoboken 41B-122	5	12.3

*U. Arizona (other measurements by U.C. Berkeley)
 **Value originally reported, before reevaluation.

A2. Electrical Performance

The electrical performance is not yet describable to the accuracy of the optical performance, and it cannot be so describable unless the counter-doping density in each detector is known.

The lifetime is describable to a good approximation by

$$\tau = \frac{1}{\beta N_c} = \frac{E}{\kappa N_c} \quad (2)$$

where N_c is the counter-doping density, and the constant κ is not yet well known for Ga in germanium. Martini and McMath (A10) give data for Ge:Ga implying $2-5 \times 10^{-4} \text{V-cm}^2/\text{sec}$ for fields of 200 to 2000V/cm (temperature unspecified), but no data for fields of order 1V/cm. The present best estimate of κ is $\kappa = 4.8 \times 10^{-3} T^{-4} \text{V-cm}^2/\text{sec}$, where T is in Kelvins.

The mobility components are presently computed as follows:

Lattice

$$\frac{1}{\mu_L} = \frac{T^{1.5}}{3.1 \times 10^7} \left(\frac{\text{V-sec}}{\text{cm}^2} \right) \quad (3a)$$

Charged Carriers (Conwell-Weisskopf)

$$\frac{1}{\mu_c} = \frac{N_c \ln(1 + 8.0 \times 10^8 T^2 N_c^{-2/3})}{1.68 \times 10^{18} T^{1.5}} \quad (3b)$$

Neutrals

$$\frac{1}{\mu_n} = \frac{N_d - N_c}{1.1 \times 10^{20}} \quad (3c)$$

Carrier-Velocity Limit

$$\frac{1}{\mu_v} = \frac{E}{v^*} \quad (3d)$$

where

T is temperature (K)

N_c is counter-doping density (atom/cm³)

v^* is carrier velocity limit (cm/sec)

E is electric field (V/cm)

At present we are linearly adding the reciprocal mobilities of Equations 3a to 3c and then root-sum-squares (rss) adding Equation 3d.



Table AII-Summary of Photoconductive Properties of Ge:Ga

<u>PARAMETER</u>	<u>BEST VALUE</u>	<u>PROBABLE FACTOR OF UNCERTAINTY</u>
Cutoff wavelength, λ_c	125 μm	1.1
Peak optical cross section, σ_{pk}	$9 \times 10^{-15} \text{cm}^2$	1.3?
Single-surface reflectance, ρ_1	36%	1.04
Recombination parameter, $\kappa = \beta E$	$4.8 \times 10^{-3} \text{T}^{-4} \text{V-cm}^2/\text{sec}$	3
Optimum doping density, N_d	$2 \times 10^{14} \text{Ga/cm}^3$	1.5
Minimum achievable counterdoping, $N_c \text{ min}$	$4 \times 10^{10} \text{atom/cm}^3$	3
Maximum bias field	1V/cm	depends on N_c
Carrier velocity limit, v^*	$7 \times 10^6 \text{cm/sec}$	2
Dielectric relaxation ratio, $\tau^* \text{ max}$	$\leq 10^4$	3

τ^* Represents ratio of DC-to-AC response.

A3. Small-Signal Photoresponse Model

The model for small-signal photoconductive gain in silicon has been compared with limited data available on several different Ge:Ga photoconductors, and agreement is good more often than not. C. M. Parry (A11) has shown that for signals small compared with dc background that photoconductive gain may theoretically be represented by

$$G(f) = \frac{\mu V \tau_0 / L^2}{1 + i 2 \pi f \tau_0} \left[1 + F(x_1, x_2, i, x_0, \Delta) \right] \quad (4)$$

where

$$F = e^{-k_3 x_0} \frac{\sinh k_3 \Delta}{k_3 \Delta} \frac{(1 - e^{k_4 L}) e^{k_3 L}}{e^{k_4 L} - e^{k_3 L}} + e^{-k_4 x_0} \frac{\sinh k_4 \Delta}{k_4 \Delta} \frac{(1 - e^{k_3 L}) e^{k_4 L}}{e^{k_3 L} - e^{k_4 L}} \quad (5)$$

$$-\frac{1}{x_1} \equiv k_3 = -\frac{\phi}{L} \left[1 + \sqrt{1 + \frac{f_0 \psi(f)}{f_1 \phi^2}} \right] \quad (6a)$$

$$-\frac{1}{x_2} \equiv k_4 = -\frac{\phi}{L} \left[1 - \sqrt{1 + \frac{f_0 \psi(f)}{f_1 \phi^2}} \right] \quad (6b)$$

(Note that $x_1 < |x_2|$ always.)

$$\psi(f) = \frac{(1 + i2\pi f \tau_0)(1 + i2\pi f \tau_\rho)}{1 + i2\pi f \tau_1} \quad (6c)$$

$$f_0 = \frac{q\mu(a_0 + p_0)}{\epsilon_0 \epsilon_r} \quad (6d)$$

$$f_1 = \frac{\mu kT}{qL^2} \quad (6e)$$

$$\phi = \frac{qV}{2kT} \quad (6f)$$

$$\tau_0 = \frac{1}{\beta(a_0 + p_0)} = \frac{V/L}{\kappa(a_0 + p_0)} \quad (\text{hole lifetime}) \quad (7a)$$

$$\tau_1 = \frac{1}{\beta p_0} = \frac{V/L}{\kappa p_0} \quad (\text{ionized-acceptor lifetime}) \quad (7b)$$

$$\tau_\rho = \frac{\epsilon_0 \epsilon_r}{q\mu p_0} \quad (\text{dielectric relaxation time}) \quad (7c)$$

- and a_0 is ionized acceptor concentration due to counterdoping (i.e., same as counterdoping density)
- d is optical depth of the detector
- f is frequency
- k is Boltzmann's constant (1eV/11,605 K)
- p_0 is ionized acceptor concentration due to photon and thermal generation (usually $p_0 \ll a_0$)
- q is electron charge (1.6022×10^{-19} coul)
- x_0 is the center-of-illumination distance ($0 < x_0 < L$)
- x_1 is a screening length for one electrode ($x=0$)
- x_2 is a measure of the screening length for the other electrode* ($x=L$)
- E is bias field ($E = V/L$)
- G is photoconductive gain
- L is interelectrode spacing
- T is temperature (K)
- V is bias voltage
- β is recombination-rate coefficient ($\beta = \kappa/E$)
- ϵ is permittivity of free space (8.8542×10^{-14} farad/cm)
- ϵ_r is dielectric constant
- η is quantum efficiency
- κ is a recombination coefficient (often more nearly constant than β)
- μ is mobility
- τ is lifetime (various subscripts, per Equations 7)
- ϕ is photon flux (photon/cm²sec)
- Δ is the half-width of the illumination

For full illumination of the detector, $x = \Delta = L/2$; so that Equation 5 becomes

$$F_1(x_1, x_2) = \frac{-(1-e^{-L/x_2})(1-e^{-L/x_1})}{e^{-L/x_2} - e^{-L/x_1}} \frac{x_2 - x_1}{L} \quad (8)$$

*May be positive or negative.



If thermal generation is negligible,

$$p_0 = \phi \frac{n}{d} \tau_0 \quad (9)$$

At low voltages and lowest frequencies, including dc, $F_1 = -\frac{x_1}{L}$, which is a very small negative number. Thus

$$G(10-f) = G(dc) \approx \frac{\mu V \tau_0}{L^2} \quad (10)$$

For very high voltage it can be shown from Equations 6 and 9 that

$$F_1 \approx -1 + \frac{1}{2} k_4 L + \frac{1}{6} (k_4 L)^2 \quad (11)$$

where $k_4 L \approx \frac{1}{2} \frac{f_0}{f_1} \frac{\psi}{\phi}$. For lowest frequencies (dc, or $2\pi f \ll \frac{1}{\tau_1}$), $\psi = 1.0$, and so from Equation 4,

$$G(dc) = \frac{1}{2} \frac{q\mu E}{\epsilon_0 \epsilon_r \kappa} \quad (12)$$

In the mid-frequency range (ac, $\frac{1}{\tau_p} \ll 2\pi f \ll \frac{1}{\tau_0}$), $\psi = \tau_1 / \tau_p$, and so from Equation 4,

$$G(ac) = 0.5 - \frac{L^2}{6\mu V \tau_0} \approx 0.5 \quad (13)$$

The ratio of dc-to-ac photoconductive gains at very high voltages is therefore the ratio of Equations 12 and 13,

$$\frac{G(dc)}{G(ac)} = \frac{\tau_1}{\tau_p} = \frac{q\mu E}{\epsilon_0 \epsilon_r \kappa} \quad (14)$$

While Equation 14 is usually viewed as a ratio of the ionized-impurity and dielectric-relaxation time constants, it is easily seen here that it may alternatively be viewed as a ratio of carrier and dielectric-relaxation velocities. For typical values $\epsilon_r \sim 16$, $\kappa \sim 10^{-4}$ V-cm²/sec and $\mu E \leq 10^7$ cm/sec it can be shown that Equation 14 is limited to the order of 10^4 . In practice, such ratios are not achieved due to voltage breakdown.



Computations of photoconductive gain have been made for Ge:Ga as a function of bias voltage and frequency, and they are shown in Figures A1 and A2 (note differences in mean wavelengths). The principal inaccuracy should be due to the poorly-known value of $\kappa = \beta E$, which is here taken to be

$$\kappa = 0.0048T^{-4}V\text{-cm}^2/\text{sec} \quad (15)$$

(Neither κ nor β is normally independent of electric field, E but κ tends to be more nearly constant at moderate and high fields.*) Eugene Haller's (A5) very-low-counter-doping-density material ($\sim 4 \times 10^{10}$ atom/cm³), 583-4.8, would exhibit a slope of 2.0 in Figure A2, particularly in the vicinity of 1V/cm bias field ($V_b = 0.1V$). If its peak responsivity at 4.2 K is between 6 and 110 amp/watt, it would imply between about 3×10^{-4} and 1.5×10^{-5} V-cm²/sec. Another detector, LBL 112-15.8, also exhibits slope 2 near 0.3V/cm, and a steeper slope at higher fields. (Both detectors approach constant β near 0.1V/cm bias field.)

However, SBRC material of doping and counter-doping densities ostensibly close to those of 583.-4.8 more nearly approximate constant β , about 3×10^{-3} cm³/sec at 2.5 K and 1.6×10^{-4} cm³/sec at 3 K, up to about 1V/cm bias** Above this field at 3 K there may be some suggestion of transition towards constant κ . If these data are correct, it also implies an exceptionally great temperature dependence for β and κ , much worse than suggested in Equation 15. On the other hand, if Moore's data for dc response are accurate also at 1Hz, implying $\sim 4 \times 10^{-4}$ cm³/sec, then the dependence of Equation 15 appears reasonable.

A compendium of low-temperature Ge:Ga detector measurements is given in Table AIII. Calculations and measurements of responsivity, quantum efficiency and photoconductive gain are compared. The counter-doping density was measured only for the SBRC detector. Thus, it is possible the true value of κ should be a factor of 3 higher than Equation 12, which correspondingly the estimated

*M. Martini and T.A. McMath (A10) show for Ge:Ga the field-dependence of β between 200 and 2000V/cm β decreased from 8×10^{-7} to 2×10^{-7} cm/sec, while κ varied about 3×10^{-4} V-cm/sec by a factor of two. No low field data were reported.

**W. J. Moore, Final Technical Report, Part I, Gallium-Doped Germanium, Evaluation of Photoconductors; NASA CR-152,222 (NRL Memorandum Report 3939), April 12, 1979.

counterdoping densities of the other detectors would be reduced by the same factor.

One nearly-complete set of experimental measurements is available for three detectors from a single Ge:Ga crystal, #112. These measurements are compared with corresponding calculations in Table AIII. (For Ge:X crystals with unknown counterdoping density, it is being assumed 3×10^{11} atom/cm³ near the seed end, which E.E. Haller suggests is typical for growths from graphite crucibles. Equation 15 is also assumed. While the mean wavelength could vary slightly with absorption depth, this variation is ignored. All other parameters are fixed by the experiment.) The agreement between calculations and measurements is unexpectedly good, particularly because the signal was roughly an order of magnitude more intense than the background. The agreement constitutes good confirmation of the validity of the small-signal model above.

The agreement between calculations and measurements in all of Table AIII is good more often than not.* However, the inconsistency of the quantum-efficiency measurements for the SBRC 4-5B1-1 detector remains to be explained.

The wide variance for the two U. Arizona measurements of 108-8.2 remains to be explained, inasmuch as no difference in experimental conditions has yet been uncovered. Calculations agree with only one of the two sets.

Agreement for the Hoboken material is unacceptably poor. Perhaps the counterdoping density exceeds 10^{12} n-atom/cm³.

Agreement for the Aerojet detector and for Eugene Haller's 583-4.8 material is good to excellent. Also for 108-17.9.

Overall, comparison of calculations and measurements reasonably confirms the validity of the computational method for design of low-background Ge:Ga focal planes.

*We may describe as "good" responsivities and quantum efficiencies which agree within a factor of 1.5 and photoconductive gains which agree within a factor of 2.



A4. Analytical Predictions

Analytical predictions of detector performance have been made in accordance with the method outlined above. (Slight approximations have been made for the complex arithmetic.) Eugene Haller's #583-4.8 material has been taken as the standard of high-quality material. A discrete parallel-electrode detector 1mm thick has been arbitrarily selected for photoconductive-gain computations. For a cold-body spectrum, computations of photoconductive gain as a function of frequency, for several bias voltages, are shown in Figure A1. The rise in gain at low frequencies results from dielectric relaxation; it is a memory effect, and it can be minimized by reducing the ac photoconductive gain to around 0.37 (or less). For a hot-body spectrum similar data are shown in Figure 2 as a function of bias voltage for several frequencies. The lower set of curves ($N_c = 4 \times 10^{11}$ atom/cm³) shows the poorer performance expected with materials grown from graphite crucibles. If memory effect is detrimental in a particular application, it may be better to reduce the bias field towards 0.5V/cm.

Computations of 100 μ m responsivity have been made for similar material (2.0×10^{14} Ga/cm³) in both lateral-electrode and monolithic configurations. Monolithic arrays should be able to approach 10 amp/watt peak responsivity, while lateral-electrode ($L = 0.5$ mm) detectors should be able to exceed it.

Bevelled detectors could provide sufficient optical enhancement to approach 25 amp/watt. If memory effects are excessive with the optically-enhanced detectors, a reduction of bias field would minimize them while still yielding better response than with the standard lateral-electrode configuration. E.g., at 0.5V/cm bias field the x4.5 optically-enhanced detector, 3mm long, would still yield 17.2 amp/watt around 1kHz, with only a 3% memory effect (more response) at 2.5Hz, though with nearly 200% more at 0.1Hz or dc. Backgrounds lower than 2×10^8 photon/cm²-sec would proportionately lower the frequency at which memory effect becomes significant. Quantum efficiency for a 3mm optically-enhanced detector at 100 μ m would be 59%, compared with 31% for the standard configuration; at 40 μ m they would be 19.6% and 5.2% respectively.

For the standard lateral-electrode configuration a 3mm-long detector would be BLIP for an NEP of 8.2×10^{-18} watt/ $\sqrt{\text{Hz}}$. ($\leq 10^{-16}$ watt/ $\sqrt{\text{Hz}}$ is required.) Thus, it seems evident that adequate detector performance will be achievable, while allowing considerable flexibility of design.

A12

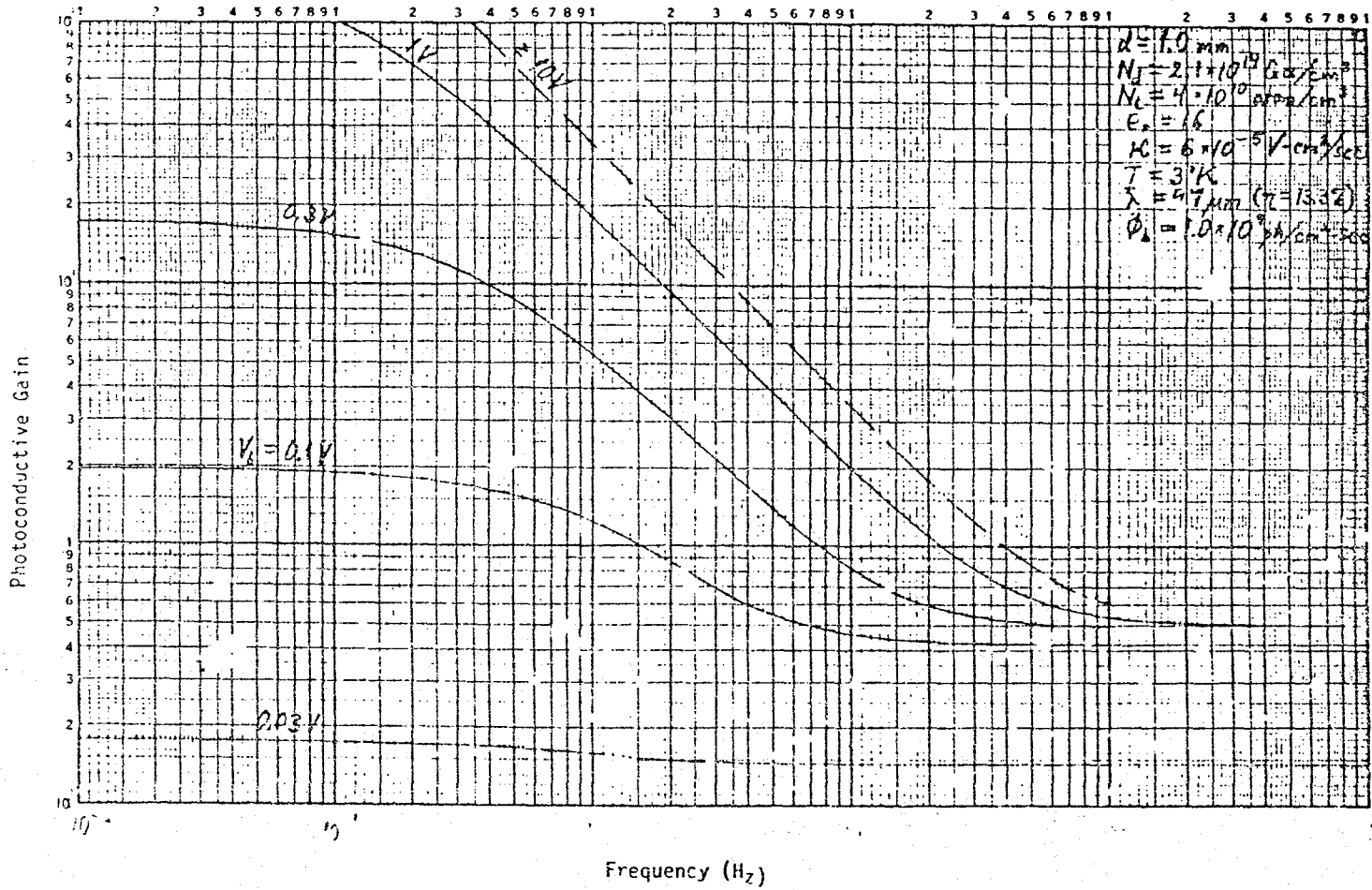


FIGURE 1. PREDICTED FREQUENCY RESPONSE OF HIGH-GRADE GaAs

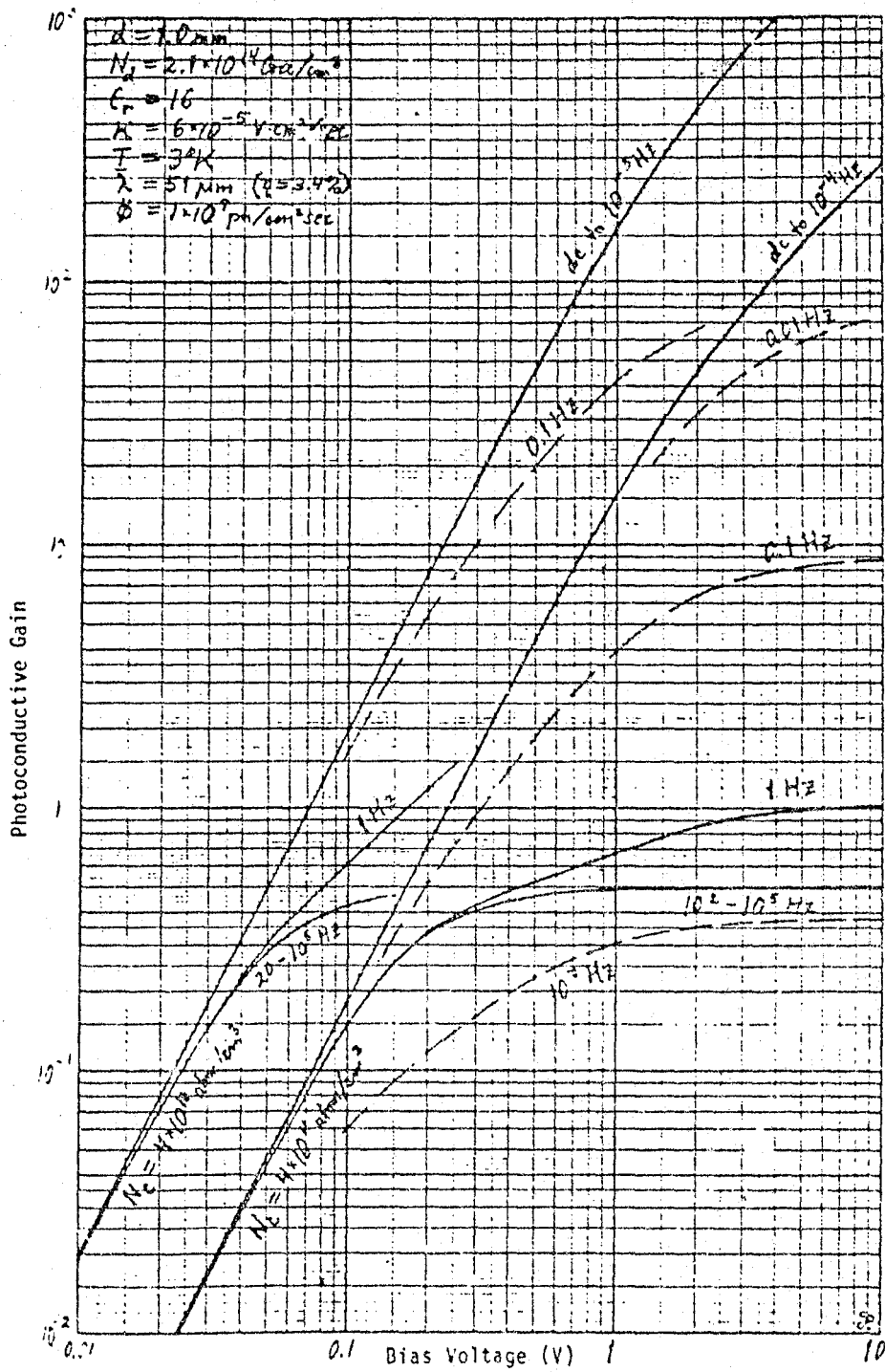


FIGURE 2. PREDICTED BIAS CURVES FOR LWIR Ge:Ga

Detector Absorption Thickness (nm)

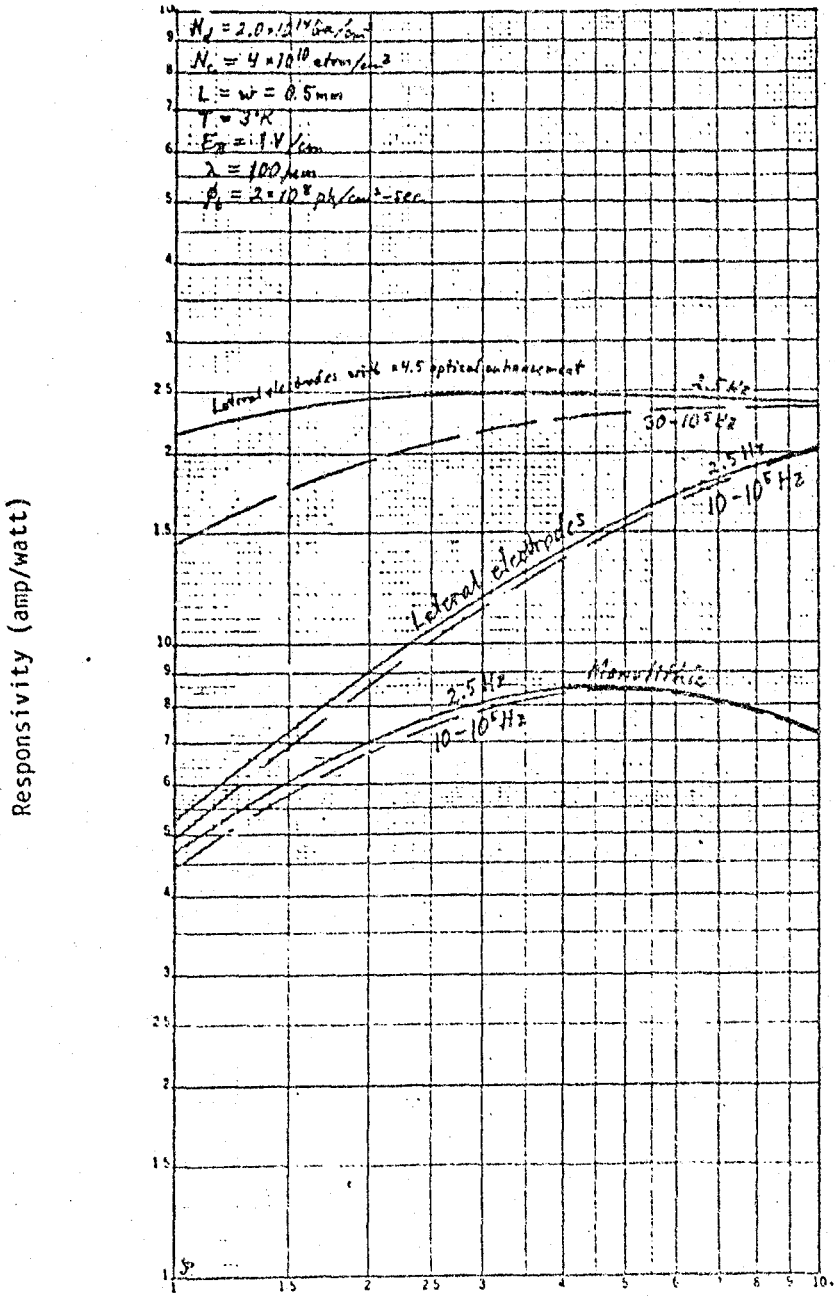


TABLE VIII
Comparison of Calculated vs Measured Ge Ge Detector Performance for Representative Sets of Data

Detector ID	Ref.	Int. Fab.	Meas.	M _d (cm ² /m ²)	M _c (cm ² /m ²)	A _d (cm)	A _c (cm)	L (cm)	V _{bias} (volts)	T _d (°K)	T _{pk} (°K)	Bandpass (Hz)	I (mA)	φ _b (ph/cm ² -sec)	f (Hz)	ε _{ph}		n		R ₁ (cm ² /m ²)	R ₂ (cm ² /m ²)	
																meas.	calc.	meas.	calc.			
1000-5-8	A1	Subey	Yes	2.3x10 ¹⁶	(3x10 ¹¹)	0.15x0.15	0.15	0.15	0.72	2.9	500	82-125	107	2.3x10 ¹⁰	20		0.70	0.21	0.21	0.21	3.56	1.69
588C-4-5B1-1	A2,3	Pratt	Moore/AEL	2.7x10 ¹⁶	8x10 ¹⁰	0.09x0.15	0.10	0.05	0.07	2.5	59.5	40-110	76	7x10 ⁹	0		[0.36]	0.24	0.24	0.24	0.90	23.9
"	"	"	"	"	"	"	"	"	0.05	3.0	"	"	"	1	1	[0.04]	0.36	0.36	0.36	0.90	6.9	
"	"	"	"	"	"	"	"	"	"	"	"	"	"	0	0	[-1.7]	1.7	"	"	7.4	25.1	
"	"	"	"	"	"	"	"	"	"	"	"	"	"	1	1	[-1.9]	1.6	-0.07	-0.07	8.3	24.2	
18L581-4-8	A4	Ballier	Low/Daz	2.1x10 ¹⁶	4x10 ¹⁰	0.25x0.25	0.10	0.0	0.06	2.3	500	40-	64	5.3x10 ⁹	5	7	0.195	0.038	0.038	0.40	0.59	
"	"	"	Scorey/UC	"	"	"	"	"	0.10	4.7	Fabry-Perot	"	51	6x10 ¹⁰	26	7	0.031	>0.031	>0.031	110	7.10	
"	"	"	Roehren/UC	2.1x10 ¹⁶	4x10 ¹⁰	0.10x0.10	0.10	0.10	0.20	3	18.5	"	94	4.7x10 ⁹	150	"	[0.07]	0.34	0.34	0.34	11.6	2.5
"	"	"	"	"	"	"	"	"	0.04	"	"	"	94	4.5x10 ⁹	"	7	[-0.38]	0.4	0.4	11.6	2.5	
18L108-8-2	A4,7	"	Roehren/UC	1.1x10 ¹⁶	(3x10 ¹¹)	0.5x0.5	0.10	0.0	0.15	3	18.5	40-	95	4.8x10 ⁹	150	"	[0.18]	0.075	0.075	1.04	2.0	
"	"	"	Low/Daz	"	"	0.5x0.5	0.10	0.0	0.15	2.3	300	40-	84	5.1x10 ⁹	5	5	[1.8]	0.03-0.055	0.031	2.9	0.36	
"	"	"	"	"	"	0.25x0.25	0.10	0.0	0.20	2.3	"	"	"	5.3x10 ⁹	5	7	0.30	0.30	0.30	0.55	0.50	
18L108-17.9	A6	"	Low/Daz	2.10x10 ¹⁶	(4.4x10 ¹¹)	0.25x0.25	0.10	0.0	0.20	2.3	500	40-	64	5.3x10 ⁹	5	7	0.18	0.056	0.056	0.060	0.57	
18L112-15.2	A6	"	Roehren/UC	2.0x10 ¹⁶	(1x10 ¹¹)	0.10x0.10	0.10	0.10	0.20	3.0	18.5	"	95	4.8x10 ⁹	150	"	[0.16]	1.0	1.0	12.1	8.7	
"	"	"	"	"	"	"	"	"	0.75	"	"	"	"	4.8x10 ⁹	"	"	[-0.22]	0.5	0.29	8.1	9.1	
18L112-18.0	A6	"	"	2.6x10 ¹⁶	(3.8x10 ¹¹)	0.25x0.25	0.25	0.25	0.75	"	"	"	"	5.1x10 ⁹	"	"	[0.08]	0.25	0.32	1.5	1.4	
18L112-21.0	A5	"	"	4.0x10 ¹⁶	(4.8x10 ¹¹)	0.15x0.15	0.10	0.0	0.175	"	"	"	"	1.9x10 ⁹	"	"	[-0.23]	0.73	0.27	4.1	1.1	
Roehren	518-122	A6	Roehren/UC	7.0x10 ¹⁶	(3x10 ¹¹)	0.5x0.5	0.10	0.0	0.30	3	18.5	"	95	4.8x10 ⁹	150	"	[0.15]	0.05	0.12	0.38	4.1	

() Guaranteed [] computed from other measurements. † in cavity; φ_b in ph/sec. *recalculated by AELC (without and with a boson correction).

REFERENCES TO APPENDIX A

- A1. Yee, James, Stressed Gallium Doped Germanium Detector, Final Report; Aerojet ElectroSystems Company, July 1980, Contract NAS5-25975. Also, private communications from James Yee.
- A2. Moore, W. J., Final Technical Report, Part I, Gallium-Doped Germanium, Evaluation of Photoconductors; NRL Memorandum Report 3939, NASA CR-152,222, April 12, 1979.
- A3. Bratt, P. R., and Lewis, N. N., Final Technical Report, Development of Doped-Germanium Photoconductors for Astronomical Observations at Wavelengths from 30 to 120 Micrometers; Santa Barbara Research Center, NASA-CR-152,046, 31 October 1977. Also, private communications from P. R. Bratt.
- A4. Haller, E. E., Hansen, W. L., and Hubbard, G. S., Ge:Ga Far Infrared Photoconductors; Lawrence Berkeley Laboratory Progress Report for 1 May to 31 December 1979. Also, private communications from E. E. Haller.
- A5. Haller, E. E. and Hansen, W. L., Ge:Ga Far Infrared Photoconductors; Lawrence Berkeley Laboratory Progress Report for 1 January to 31 October 1980.
- A6. Haller, E. E., Hueschen, M. R., and Richards, P. L., Ge:Ga Photoconductors in Low Infrared Backgrounds; Applied Physics, Letter 34 (8), p. 495-497 (15 April 1979). Also, private communications from M. R. Hueschen.
- A7. Hueschen, M. R. and Richards, P. L., Letter to Craig McCreight/NASA-Ames, 3 May 1979.
- A8. Low, Frank J., Letter to Craig McCreight/NASA-Ames, 3 April 1979.
- A9. Williams, R. L., J. App. Phys. 40, 691 (1969) and Infrared Physics 9, 37 (1969).
- A10. Martini, M. and McMath, T. A., Field Dependence of the Capture and Re-emission of Charge Carriers by Shallow Levels in Germanium and Silicon; Solid State Electronics 16, p. 129-142, February 1973.
- A11. Parry, C. M. and Parkinson, J. B., Hardened Detector/Circuit Development (U), Vol. I; Aerojet ElectroSystems Co. Report 5059, Appendix B (Unclassified), September 1974. Secret. Some terminology here has been altered for possibly improved clarity.

APPENDIX B

OPTICAL EFFICIENCY & CROSSTALK



B1 GENERALIZED MODEL FOR QUANTUM EFFICIENCY AND CROSSTALK

The transmission of the front surface is $(1 - r_1)$, where r_1 is the reflectance of the front surface (about 36%, except far from normal incidence). Each pass through a detector of thickness, d , will traverse an oblique path of $s = d/\cos\theta$, yielding an absorption of $1 - e^{-\alpha s}$, where $\alpha = N_x \sigma(\lambda)$ is the absorption coefficient in cm^{-1} . For normal incidence the total absorption (quantum efficiency) in the detector will be

$$\begin{aligned} \eta &= (1 - r_1) \left[1 - e^{-\alpha s} \right] \left\{ 1 + r_2 e^{-\alpha s} + r_2 r_1 e^{-2\alpha s} + r_2^2 r_1 e^{-3\alpha s} + \dots \right\} \\ &= \frac{(1 - r_1) \left[1 - e^{-\alpha s} \right] (1 + r_2 e^{-\alpha s})}{1 - r_1 r_2 e^{-2\alpha s}} \end{aligned} \quad (1)$$

For non-normal incidence ($\theta \neq 0$), the quantum efficiency and crosstalk should be represented by truncated series of the form of Equation 1. Define j' , the number of optical double-passes in travelling a lateral distance X ,

$$j' = \frac{X}{2d \tan\theta} \quad (2)$$

Then the number of complete double-passes may be defined as

$$j = \text{Int} (j') \quad (3a)$$

and the remaining fraction as

$$\delta = \text{Frac} (j') \quad (3b)$$

For $\delta < 0.5$ the final (fractional) pass will be in the direction of incidence, while for $\delta > 0.5$ it will be back towards the direction of incidence. The absorption may then be expressed as

$$\frac{n}{1-r_1} = \left[1 - e^{-\alpha s} \right] \frac{(1 + r_2 e^{-\alpha s}) - (r_1 r_2 e^{-2\alpha s})^{j+1}}{1 - r_1 r_2 e^{-2\alpha s}} + \Delta(\delta) \quad (4a)$$

where the absorption of the fraction pass is

$$\begin{aligned} \Delta &= r_1^j r_2^j e^{-2j\alpha s} \left[1 - e^{-(2\delta)\alpha s} \right], \quad 0 \leq \delta \leq 0.5 \\ &= r_1^j r_2^j e^{-2j\alpha s} \left[1 - e^{-\alpha s} \right] \\ &\quad + r_1^j r_2^{j+1} e^{-(2j+1)\alpha s} \left[1 - e^{-(2\delta - 1)\alpha s} \right], \quad 0.5 < \delta < 1.0. \end{aligned} \quad (4b)$$

The angle-from-normal in the detector, θ , is related to the angle-of-incidence in vacuum, θ' , by

$$\sin \theta = \frac{1}{n} \sin \theta' \quad (5)$$

where in germanium cryogenic $n \approx 3.98$.

Quantum efficiency can, in principle, be determined from an integration of Equation 4 over all angles of incidence and all points of incidence (weighted according to a distribution determined by the upstream optics). Crosstalk contributions could similarly be determined by differences of Equation 4 for X_2 's and X_1 's.

B-2 ANALYTICAL SIMPLIFICATIONS

For many computational purposes, Equations 2 - 5 are unduly cumbersome. For incidence angles, θ' , up to $30 - 40^\circ$, Equation 5 may be approximated by

$$\theta = \theta'/n \quad (6)$$

with less than 5 - 10% error. For no more than another 1% error, $\tan \theta$ in Equation 2 may be replaced by θ expressed in radians (or $\pi \theta/180$ if expressed in degrees). For $j \gg 1$ an enormous simplification may be achieved in Equation 4 by smoothing the fractional contribution, Δ ,

$$\eta = (1 - r_1) \frac{[1 - e^{-\alpha s}] \left[(1 + r_2 e^{-\alpha s}) - (r_1 r_2 e^{-2\alpha s})^{j+1} \right]}{1 - r_1 r_2 e^{-2\alpha s}} \quad (7)$$

$$\text{with } j = j' \approx \frac{X}{2d\theta} \approx \frac{nX}{2d\theta'} \quad (8)$$

$$\text{and } s = d/\cos\theta \approx d(1 + \theta^2/2) \approx d \quad (9)$$

Equation 9 yields an error no greater than 1.5%. Thus, Equations 2-5 are greatly simplified, including the elimination of Equation 3.

The greatest error in absorption, η , would occur for $x \rightarrow 0$, where Equation 7 remains finite, but such a case already defies the $j \gg 1$ condition.

ORIGINAL DOCUMENT
OF POOR QUALITY

B-2 QUANTUM EFFICIENCY AND CROSSTALK

The effective quantum efficiency of the detector, $\bar{\eta}$, is now determined by an integration over the distances and incidence-angles of interest. For Cartesian coordinates and a weighting function,

$$\bar{\eta}(\lambda) = \frac{\int_0^{\theta_m} \int_{x_1}^{x_2} \int_{y_1}^{y_2} \eta(\theta, x, y, \lambda) w(\theta, x, y) dy dx d\theta}{\int_0^{\theta_m} \int_{x_1}^{x_2} \int_{y_1}^{y_2} w(\theta, x, y) dy dx d\theta} \quad (10a)$$

while for polar coordinates

$$\bar{\eta}(\lambda) = \frac{\int_0^{\theta_m} \int_{r_1}^{r_2} \int_0^{2\pi} \eta(\theta, r, \phi, \lambda) w(\theta, r, \phi) r d\phi dr d\theta}{\int_0^{\theta_m} \int_{r_1}^{r_2} \int_0^{2\pi} w(\theta, r, \phi) r d\phi dr d\theta} \quad (10b)$$

where θ_m is the maximum incidence angle provided by the optics. In most practical cases the weighting function in Equation 10b will be independent of ϕ ; so that integration may be replaced by 2π . For an extended black-body source, $w(\theta) = \cos\theta \sin\theta$, with the first term due to projected area and the second due to solid angle.

For quantum-efficiency computations with Equation 10, $x_1 = y_1 = r_1 = 0$. For crosstalk computations, these lower-limit dimensions are finite, as determined from the detector dimensions.

B3 CROSSTALK COMPUTATIONS

Computations of crosstalk have been made for optically-enhanced Ge:Ga detectors and are shown in Figure B1. (These computations were made ray-at-a-time according to the pattern of Equations 1 - 5, but with modification for an average 4.5x enhancement of the first optical pass only.) It is easily seen that at all angles the initial pass attenuates to about 37% of its initial absorption rate, while after the first reflection at $x = x_1$ it attenuates very rapidly. Since less than 15% of the total absorption occurs after the first reflection, and since it attenuates very rapidly thereafter, it can be neglected for most purposes. Thus, crosstalk to the adjacent detector may be computed by

$$\begin{aligned} \Delta n_1 &= \frac{1}{L} \int_0^L \int_x^{x_1} \left. \frac{dn}{dx} \right|_0 e^{-x'/\bar{x}} dx' dx \\ &= \left. \frac{dn}{dx} \right|_0 \frac{1}{L} \int_0^{x_1} \left(e^{-x/\bar{x}} - e^{-x_1/\bar{x}} \right) dx \\ &= \left. \frac{dn}{dx} \right|_0 \frac{\bar{x}}{L} \left[\bar{x} \left(1 - e^{-x_1/\bar{x}} \right) + x_1 e^{-x_1/\bar{x}} \right] \end{aligned} \quad (11)$$

Equation 11 assumes no null space between detectors.

Equation 11 has been solved for cases of $F/24$, ^{and} $F/4.5$ optics, along with parameters describing the absorption, as shown in Table B1.

TABLE B.II
COMPUTED CROSSTALK TO ADJACENT Ge:Ga DETECTOR

	$\lambda(\mu\text{m})$	$\Delta\eta_1$	$d\eta/dx \text{ (mil}^{-1}\text{)}$			$\bar{x}(\text{mil})$	$x_1(\text{mil})$	$x_2(\text{mil})$
			$x = 0$	$x = x_1$	$x = y_2$			
F 24	110	1.50%*	0.5493	0.200	0.0575	1.165	1.178	1.439
F 24	70	2.22%	0.2277	0.150	0.0491	2.811	1.178	1.439
F 4.5	110	7.9%*	0.1036	0.038	0.0108	6.178	6.245	7.633
F 4.5	70	11.8%	0.0430	0.028	0.0093	14.901	6.245	7.633

* To be compared with 47% total quantum efficiency

(x_1 represents the first reflection, from the back surface, while x_2 represents the next reflection, from the front surface. x_2 conditions are not used in Equation 11.) There will be negligible crosstalk to more distant detectors, as x_1 (and x_2) are very much smaller than the 50-mil center-to-center spacings of the detectors.

The optical crosstalk within the focal plane will be very small for F/24 optics, only around 4%. Larger angles would result in significantly larger crosstalk to the adjacent detector, as shown by the computations for F 4.5 optics. If there is any null space between detectors the crosstalk will be substantially reduced below Table I values, while a 6.2 mil null space would virtually eliminate it even for F 4.5 optics.

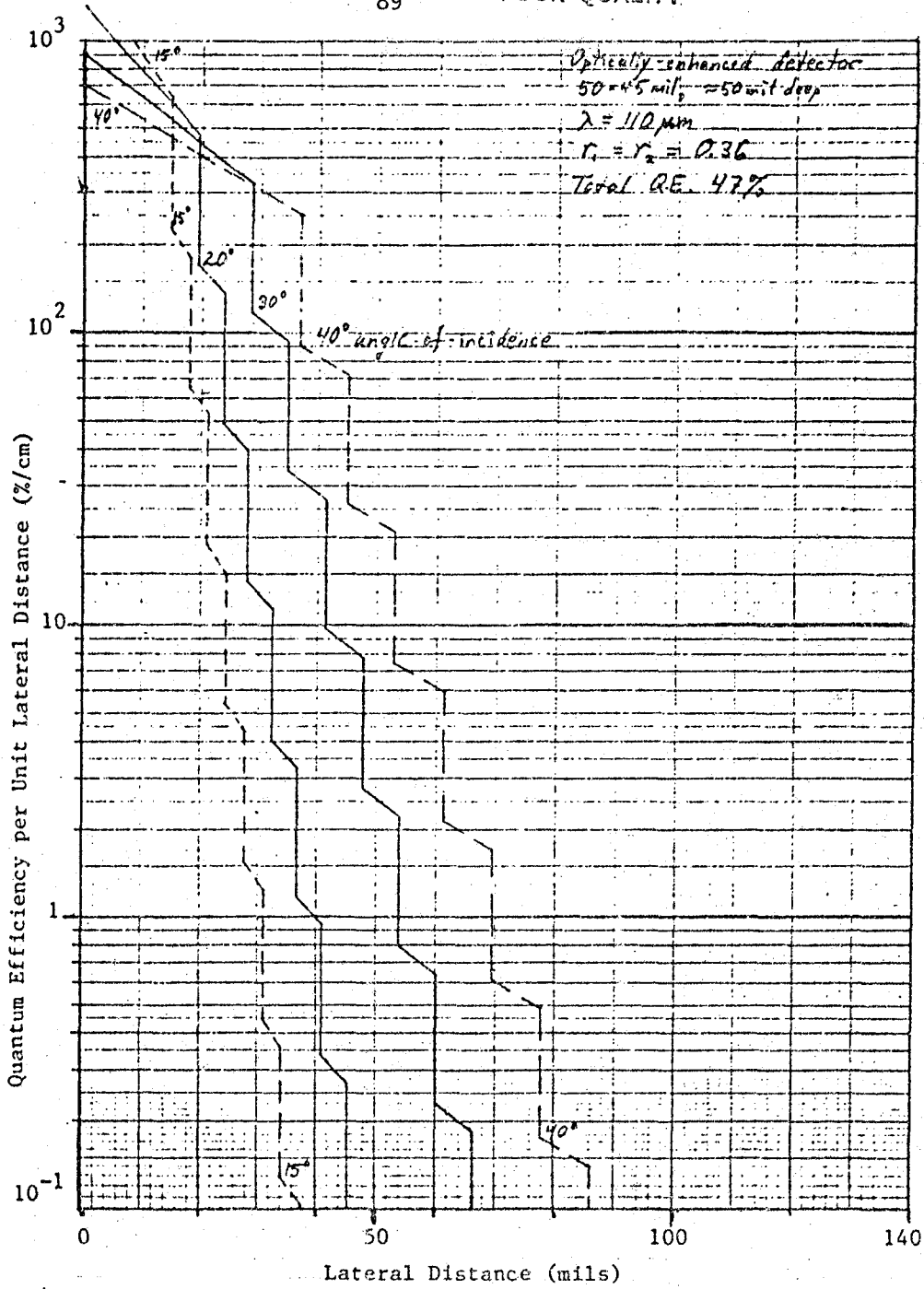


Figure B1 Crosstalk Reflectance in Ge:Ga

ORIGINAL COPY
OF POOR QUALITY

APPENDIX C

INSTABILITY OF STRESSED GERMANIUM COLUMNS

The Euler critical load criterion was used to estimate the potential maximum size of a monolithic stressed germanium element. The Euler load formula establishes the maximum stable length that a column design such that a small lateral force will not cause buckling and failure. The formula is usually presented in the form

$$P_{cr} = \pi^2 EI / L^2$$

where

E = Young's modulus (15×10^6 lb/in² for Ge)

and I = Least moment of inertia about the direction of load as axis.

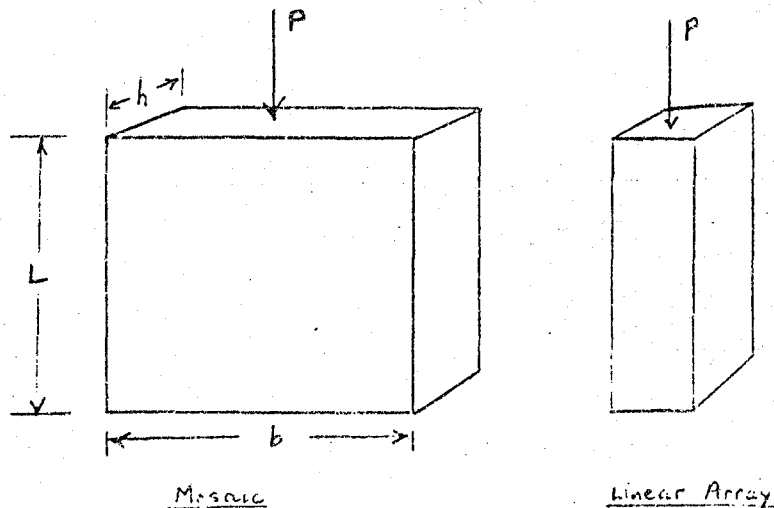


Figure C1 Geometry of Stressed Germanium Modules

Referring to Figure C1

$$I = b h^3 / 12 \quad \text{in}^4$$

and the critical stress for a column of length L is

$$\sigma_{cr} = P_{cr} / A = \left(\frac{\pi h}{L} \right)^2 \frac{E}{12}$$

In structural and machine element design, the use of the Euler load criteria is not always appropriate since the stress in the material must be below the proportional limit. In the case of single crystal germanium, however, the proportional limit and the ultimate strength are nearly equal and the crystal remains elastic up to the point of failure. The column must also be sufficiently long such that failure is due to elastic instability and not due to simple compressive stress. Again, for purposes of this calculation, the aspect ratio is forced into the "long column" regime where the Euler formula applies by setting the critical stress equal to the applied stress and solving for the length at which this stress becomes critical. Finally, the end conditions, or attachment method, establish the relationship between the effective length and the actual length. The formulae above represent the pin-ended condition, and although the column in this instance is flat ended and constrained, (which would theoretically support a load four times greater than the pin ended condition) most designers use the actual length as the effective length.

For a 90 K psi load the maximum aspect ratio (length over minimum dimension) is

$$(L/h)_{max} \leq \pi \sqrt{E/12\sigma} \approx 12$$

For a factor of two safety factor we use

$$L/h \leq 6$$

For a monolithic mosaic of 1 cm absorption depth the allowed length L would be as high as 6 cm - or 60 detector elements. However fully monolithic mosaics are precluded by other considerations such as material (and bias) uniformity requirements, crosstalk and risk of transparent electrode technology.

A monolithic stack of laterally biased detectors in a linear array form - with a rear surface bevel to permit reduced volume - would have a minimum dimension of the order of the pixel size so that the maximum module size is about 6 elements if stressed along the axis of the array.

APPENDIX DTRANSPARENT ELECTRODE DESIGN FOR FIR GERMANIUM

Transparent electrode design for extrinsic detectors represents a compromise between the need for high carrier concentration for low sheet resistance on the one hand, and the need for reduced carrier concentration to avoid free carrier absorption of long wavelength photons on the other. For Si:X detectors Schraeder et al. have provided an excellent summary of these issues in terms of the simple Drude model for free carrier absorption showing rather excellent agreement between theory and measurement.

For FIR germanium the same formulas and concepts apply in principle. The situation is complicated however by the fact that lower carrier concentrations are necessary to maintain transparency in the extreme IR. At these lower concentrations dopant ionization energy will not be fully depressed and some carrier freezeout will be expected. Note that for FIR Ge:Ga the available contact dopant species are the same as the detection species (i.e. Ga) or exhibit very similar ionization energy (e.g. boron). Since no detailed data is available concerning the dependence of gallium/boron ionization energy on concentration, and since the freezeout will be mitigated to some indeterminate extent by impact ionization and hopping conduction, the actual dependence of carrier concentration on contact doping density is rather uncertain. Estimated upper and lower bounds are plotted in Figure D1. Also plotted is the approximate dependence of the mobility of free holes in p-type germanium, based on the data compiled in Reference D1.

For silicon Schroeder (Ref D2) has demonstrated satisfactory near quantitative agreement between measurement and the simple Drude models of free carrier absorption and conductivity. For a contact carrier density profile $p(x)$

ORIGINAL
OF POOR QUALITY

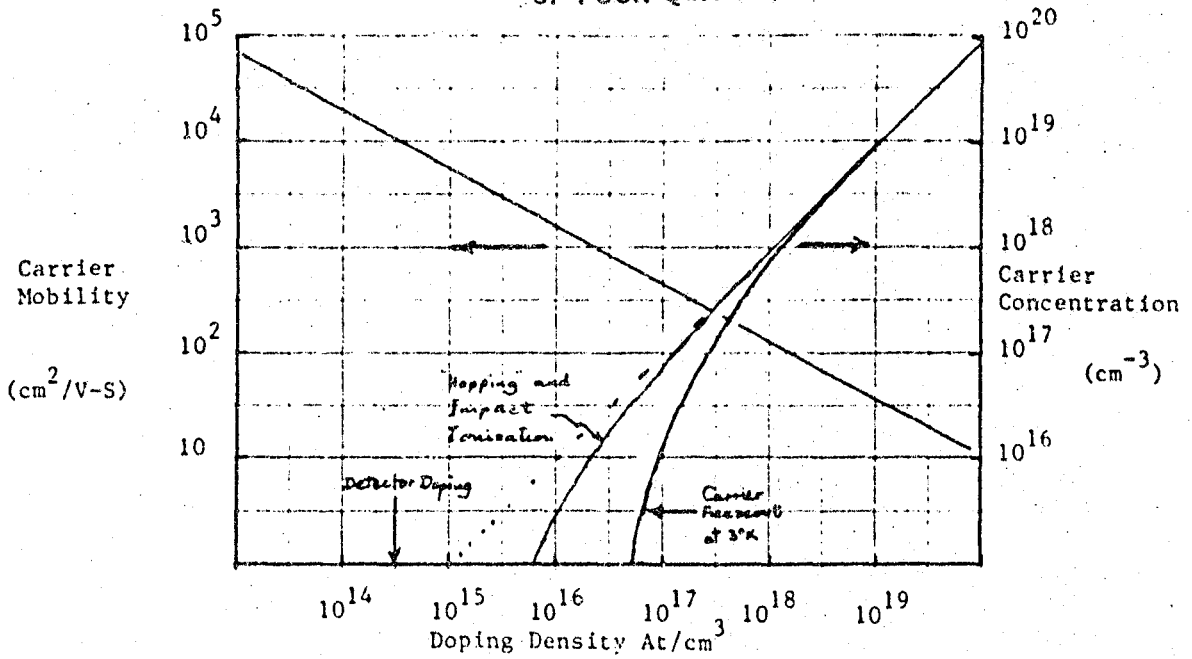


Figure D1 Carrier Concentration and Mobility

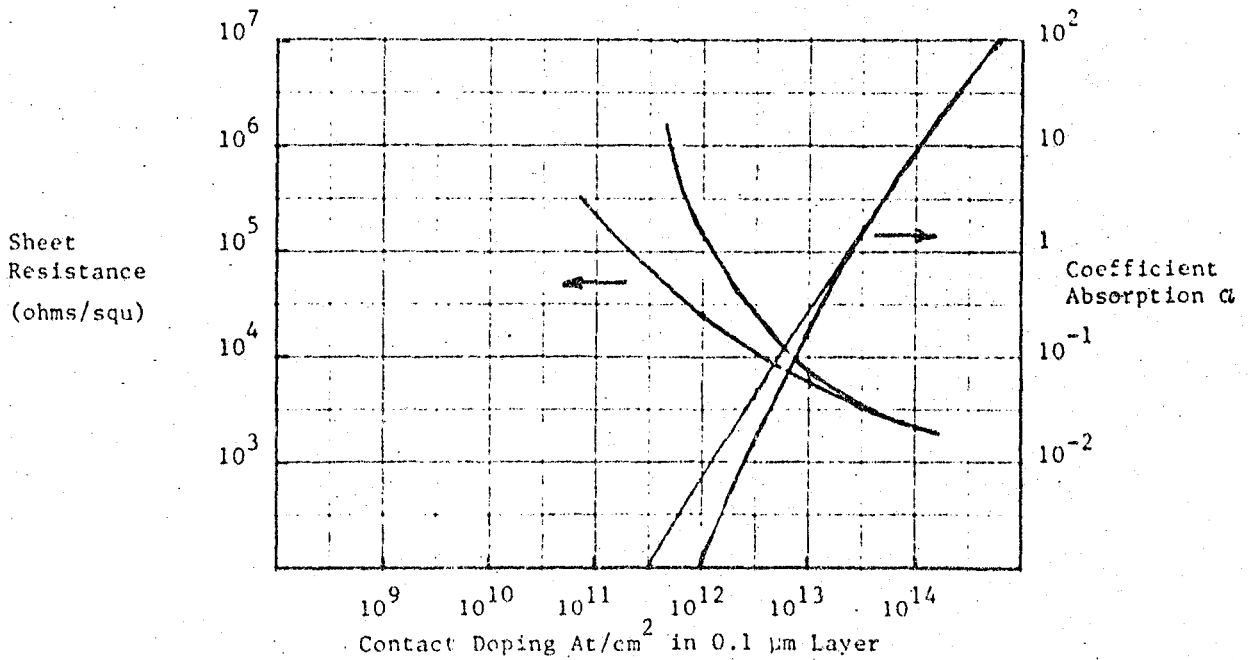


Figure D2 Transparent Contact Properties

the absorption at wavelength λ is given by

$$A = 1 - e^{-\int \alpha(x) dx}$$

where

$$\alpha(x) = q^3 \lambda^2 p(x) / \{4\pi^2 \epsilon_c c^3 n m^* \mu\}$$

Adjusting Schroeder's measured coefficients to reflect the difference between the values of refractive index n , and effective mass m^* , for silicon and germanium yields an expected absorption coefficient for a germanium contact of the form

$$\alpha = \int \alpha(x) dx \approx 2 \times 10^{-12} \int [p(x)/\mu(x)] dx$$

while the sheet resistance of the contact would be

$$R_{\square} \approx 6 \times 10^{23} / \int p(x) \mu(x) dx$$

The values of absorption coefficient α and sheet resistance R_{\square} plotted for a germanium contact in Figure D2 were computed using these relationships and the carrier concentration data of Figure D1. For the purposes of this computation the contact doping was assumed to be uniform in a 1000 Å layer, a 10^{12} atom/cm² doping corresponding to a doping density $p(x)$ of 10^{17} atoms/cm³.

Based on Figure D2 it would seem that doping below the mid- 10^{12} /cm² range is required to assure transparency at 200 μ m while doping in the vicinity of 10^{12} atom/cm² or greater is necessary for sufficiently low sheet resistance - for low background detectors 10^6 ohms per square or less. Thus while an FIR transparent contact appears feasible, the permissible doping range is very restricted and, considering the rather approximate nature of the analysis, must be viewed as a high risk until actually demonstrated.

Ref. D1 M. Neuberger EPIC Germanium-Data Sheets. AD 610828 (Feb. 1965)

Ref. D2 D. K. Schroeder et al. IEE Journal of Solid State Circuits, SC-13, P 180 (Feb. 1978).

APPENDIX E

VULNERABILITY TO SPACE RADIATIONS

Average detector cross-sections to trapped protons and electrons, and corresponding average pulse amplitudes, have been calculated as functions of detector size for doped-germanium low-background detectors in Space Shuttle orbits (≤ 600 km altitude). Average cross-sections are typically in the range 0.004 to 0.23 cm^2 , and average pulse amplitudes typically in the range 0.15 to 3×10^6 carrier pairs. In the worst location of a space shuttle orbit doped-germanium detectors of 1 mm-cube size will generate about 75 pulse/second with 10^5 carrier-pairs average amplitude, and about 4 pulse/sec with 10^6 carrier-pairs average amplitude, (the pulse rates and amplitudes are independent of dopant). Significant noise-pulse rates could occur during 25% of a worst-case 460-km circular orbit of 40° inclination when the southerly extreme occurs in the South Atlantic Magnetic Anomaly.

E-1 Detector Vulnerability Model

Event rates for particle ionizations may be determined from the average projected area. For rectangular detector and for omnidirectional charged particles travelling in straight lines this is one-fourth of the convex surface area, or

$$\bar{A}_p = \frac{Lw + wd + dL}{2} \quad (1)$$

where L , w , and d are the electrically-active dimensions. The average pulse amplitude is the total ionization rate divided by the pulse rate,

$$\begin{aligned} h_a &= \phi K \left(\frac{\text{rad-cm}^2}{\text{particle}} \right) \frac{100}{1.6 \times 10^{-12}} \left(\frac{\text{eV}}{\text{rad-gm}} \right) \frac{(\text{cp})}{2.6 (\text{eV})} 5.32 \left(\frac{\text{cm}}{\text{cm}^3} \right) \frac{Lwd (\text{cm}^3)}{\bar{A}_p} \quad (2) \\ &= \frac{1.277 \times 10^{14} K Lwd}{\bar{A}_p} \text{ carrier pairs (cp)} \end{aligned}$$

where K (the ^{dose} per particle) is a characteristic of the energy spectrum of the ionizing flux.

Simple approximations, suitable for hand computation, are sometimes desired for proton-dose calculations. For a power-law incident flux,

$$\phi(E) dE = nB E^{-(n+1)} dE \quad (3)$$

where B and n are constants (and which, obviously, must be cut off at some low energy), such an approximation has been found at Aerojet by numerical analysis of cases where n is in the range $1 \leq n \leq 4$.

Defining the cumulative flux as

$$\begin{aligned} \phi(>E) &= \int_E^{\infty} \phi(E) dE \\ &= B E^{-n} \end{aligned} \quad (4)$$

the dose, D , at a given depth of penetration may be expressed as

$$D = \left[\frac{D}{\phi}(E_0) \right] \phi(>E_0) F \quad (5)$$

where E_0 is the minimum energy required of a proton in order to penetrate the shielding to the given depth, the shielding factor*, F , is

$$F = F_1 F_2 \quad (6)$$

where $F_1 = 0.5 n^{3/4}$ and $F_2 = 7/(7+4n)$

and $\frac{D}{\phi}(E) = 3.2 \times 10^{-6} E^{-0.75} \frac{\text{rad(Si)}}{\text{protons/cm}^2} \quad (7)$

* Note: The term F_2 in Equation 6 is the fraction of omnidirectional protons penetrating a slab shield referenced to the omnidirectional flux above the minimum energy to penetrate (at normal incidence). The term F_1 accounts for the greater ionizing effect from protons slowed down by the shielding.

To obtain dose per penetrating proton, K, use

$$K = F_1 \frac{D}{\phi}(E) \quad (8)$$

For electrons $K \approx 3 \times 10^{-8}$ rad-cm²/electron (most materials) and for South Atlantic protons ≥ 50 MeV (typical for penetration of satellite-structure effective shielding) $K \approx 13 \times 10^8$ rad-cm²/proton. For determination of K for protons, use Equations 7 and 8 above. The exponent n may be estimated from the flux-energy distributions of NSSDC/WDC-A-R&S 76-06 (For example see Figures E8 and E9)

E2 Ionization Rates in Shuttle Orbit

In a worse-case shuttle orbit the radiation-environment maxima will be at the 460 km maximum altitude:

$$1 \times 10^3 \text{ protons/cm}^2\text{-sec } (>50 \text{ MeV}) \text{ } 34^\circ\text{S } 37^\circ\text{W}$$

$$2 \times 10^5 \text{ electrons/cm}^2\text{-sec } (<0.5 \text{ MeV}) \text{ } 32^\circ\text{S } 38^\circ\text{W}$$

(and S. auroral zone)

$$2 \times 10^4 \text{ electrons/cm}^2\text{-sec } (>5 \text{ MeV}) \text{ } 32^\circ\text{S } 38^\circ\text{W}$$

Typical structure and shielding would be equivalent to about 25% of the total solid angle having only 2-3 gm/cm² protection, thus allowing some electrons as low as 5 MeV and some protons as low as 50 MeV to reach the detectors.

For a 1 mm cube Ge:X detector ionization response may be estimated by analysis in terms of the effective detector cross-section \bar{A} and the average pulse height (carrier pairs) generated.

	$\bar{A}(\text{cm}^2)$	$h_{\text{avg}}(\text{cp/pulse})$
Protons	1.5×10^{-2}	1.1×10^6
Electrons	1.5×10^{-2}	3×10^5
Photons (1 MeV)	1.5×10^{-4}	3×10^5

(For comparison with Aerojet experimental measurements on detectors of this size, see J. B. Parkinson and T. G. Moore, Hardened Space Sensors (U); AFML-TR-71-139, July 1972. Secret.)

Pulse rates for the highest So. Atlantic Anomaly fluxes, in the absence of dedicated shielding, would be for protons

$$\dot{N}_p \approx (0.25) 1 \times 10^3 \frac{p^+}{\text{cm}^2\text{-sec}} 1.5 \times 10^{-2} \approx 4 \text{ pulse/sec}$$

$$h_a \approx 1.1 \times 10^6 \text{ cp}$$

and for electrons/bremsstrahlung

$$\dot{N}_e \approx (0.25) 2 \times 10^4 \frac{e^-}{\text{cm}^2\text{-sec}} 1.5 \times 10^2 \text{ cm}^2 \approx 75 \text{ pulse/sec}$$

$$\dot{N}_b \approx (\sim 0.5) 2 \times 10^5 \frac{e^-}{\text{cm}^2\text{-sec}} (0.5 \frac{\text{MeV}}{e^-}) \frac{0.5 \times 13}{1500} 1.5 \times 10^{-4} \frac{\text{cm}^2}{\text{MeV}} \approx 0.03 \text{ pulse/sec}$$

$$h_a \approx 3 \times 10^5 \text{ cp}$$

Computation results are summarized in Table I.

The noise-pulse rates for other orbits will be less severe, although the pulse amplitudes will be little affected. E.g., for 300 km altitude and 23° inclination the pulse rates would be only about 1.1 pps from protons and 11 pps from electrons. For polar orbits significant pulse rates would occur for no more than 10% of the worst orbit. For inclinations less than 5° no significant pulses would occur (< 0.1 pps due to cosmic rays). The pertinent proton and electron maps at 300 km and 500 km altitudes are shown in Figure 1-4.*

The influence of detector size on proton pulse rates is shown in Figure 5 by means of the average cross section to charged particles (same as average projected area). The influence on pulse amplitudes is shown in Figure 6; the average amplitudes from electrons are around 25% of those from protons. The pulse amplitude distribution for detectors thin in one dimension is well approximated by $P(> h) = \exp(-h/h_a)$; for detectors near cube shape there are fewer pulses at very large and very small amplitudes. For comparison with Figure 6,

* Taken from E. G. Stassinopoulos, World Maps of Constant B, L, and Flux Contours; NASA SP-3054, 1970.

TABLE I
 PARTICLE IONIZATIONS
 1 mm CUBE OF GERMANIUM

ALT	PARTICLE	FLUX	E_{MeV}	$N \text{ sec}^{-1}$	\bar{h}_{crpr}
460 Km. @ 33°S	Protons	1×10^3	> 50	4	1.1×10^6
	EL & BR.	2×10^5	> 0.5	.03	3×10^5
2×10^4		> 5	75		
300 Km @ 23 S	Protons	3×10^2	> 50	1.1	1.1×10^6
	Electrons	1.5×10^5	> 0.5	.02	3×10^5
3×10^3		> 5	11		

ES

proton average pulse amplitude for detectors of a non-square (2:1) cross section are shown in Figure 7.

Dedicated shielding could practically eliminate electron pulses (< 0.01 pps), though proton pulse rates cannot feasibly be reduced by an order of magnitude.

The following computations are presented to illustrate the method of estimating predicted pulse rates from space-radiation environments.

Protons:

$$\text{Pulse rate } \dot{N}_p \sim \frac{7}{7+4n} \dot{A}_p \phi (> E_{c,p}) \sim 5 \times 10^3 \phi_p (> 50 \text{ MeV})$$

where n is the exponent for proton flux $\phi_p = \phi_{po} E^{-n}$ (Here $1.5 \lesssim n \lesssim 2$.)

Electrons:

$$\text{Pulse rate } \dot{N}_e \sim \left(\frac{\Omega}{4\pi}\right) \bar{A}_e \phi_e (> E_{c,e} \sim 5 \times 10^{-3} \phi_e (> 3.75 \text{ MeV}))$$

where the minimum shielding likely pertains to $0.25 \lesssim \frac{\Omega}{4\pi} \lesssim 0.05$. (From the in-board side of the platform electrons will probably not penetrate.)

Bremsstrahlung:

$$\text{Pulse rate } \dot{N}_{br} \sim \frac{\phi_e (> 0) \bar{E}_e - \bar{E}_e - 2}{E_{br}} \frac{\bar{E}_e - 2}{1500} A_Y \sim 2 \times 10^{-8} \phi_e (> 0)$$

where $\bar{E}_e \sim 0.2$ MeV, perhaps $E_{br} \sim 0.3$ MeV, and $A_Y \sim 5 \times 10^{-6} \text{ cm}^2$.

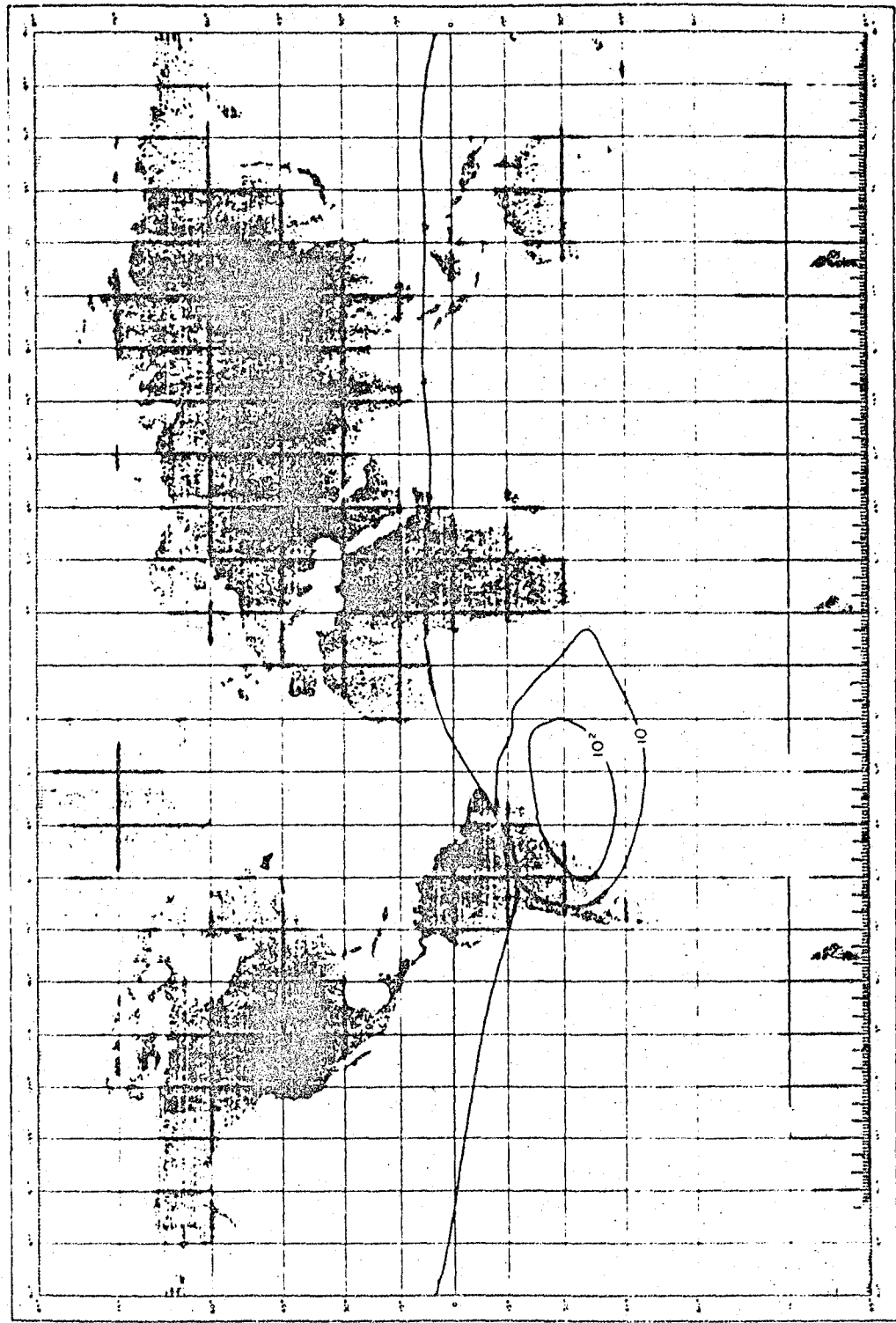
Cosmic Rays:

Fluxes $\sim 1 \text{ p/cm}^2\text{-sec}$ yield $\dot{N}_{cr} \sim 10^{-2}$ pps per detector and are ignored here. $\bar{A}_p = \bar{A}_e \sim 1.5 \times 10^{-2} \text{ cm}^2$, and "7(7 + 4n)" accounts for oblique penetration of isotropic protons. Electron pulses can be virtually eliminated by increasing the minimum shielding from an assumed 2.9 gm/cm^2 (0.42 inch Al) to 4 gm/cm^2 ; the peak bremsstrahlung pulse rate in the South Atlantic Anomaly would be 0.03 pps/detector. Not much can feasibly be done to reduce the proton rate.

Symbols

\bar{A}_p	Average projected area (averaged over 4π steradians)
\bar{A}_x	Average projected area sensed by "x" particles
A_Y	Average effective cross section to gamma rays (or bremsstrahlung)
$E_{c,x}$	Cutoff energy for "x" particles (i.e., the minimum energy required for "x" particles to penetrate the shielding)
\bar{E}_x	Average energy for "x" particles
h_a	Average pulse amplitude, in carrier pairs; same as h_{avg}
n	Power-law exponent for proton spectral-energy distribution, $\phi_p (>E) \propto E^{-n}$
K	Average dose per ionizing particle
N_{br}	Pulse rate due to bremsstrahlung
N	Pulse rate due to cosmic rays
N_x	Pulse rate due to "x" particles
x	protons (p), electrons (e or e^-), or bremsstrahlung (br)
Z	Atomic number of the shielding material
ϕ_x	Flux rate density of "x" particles (usually above some energy, E) in "x"/ cm^2 -sec
Ω	Solid angle, in steradians (especially the angle representing thinnest shielding)

FIGURE 1. PROTON FLUX CONTOURS-E > 50 MEV ALTITUDE = 300KM



ORIGIN
OF PROTONS

FIGURE 2. PROTON FLUX CONTOURS - E > 50 MEV ALTITUDE = 500 KM

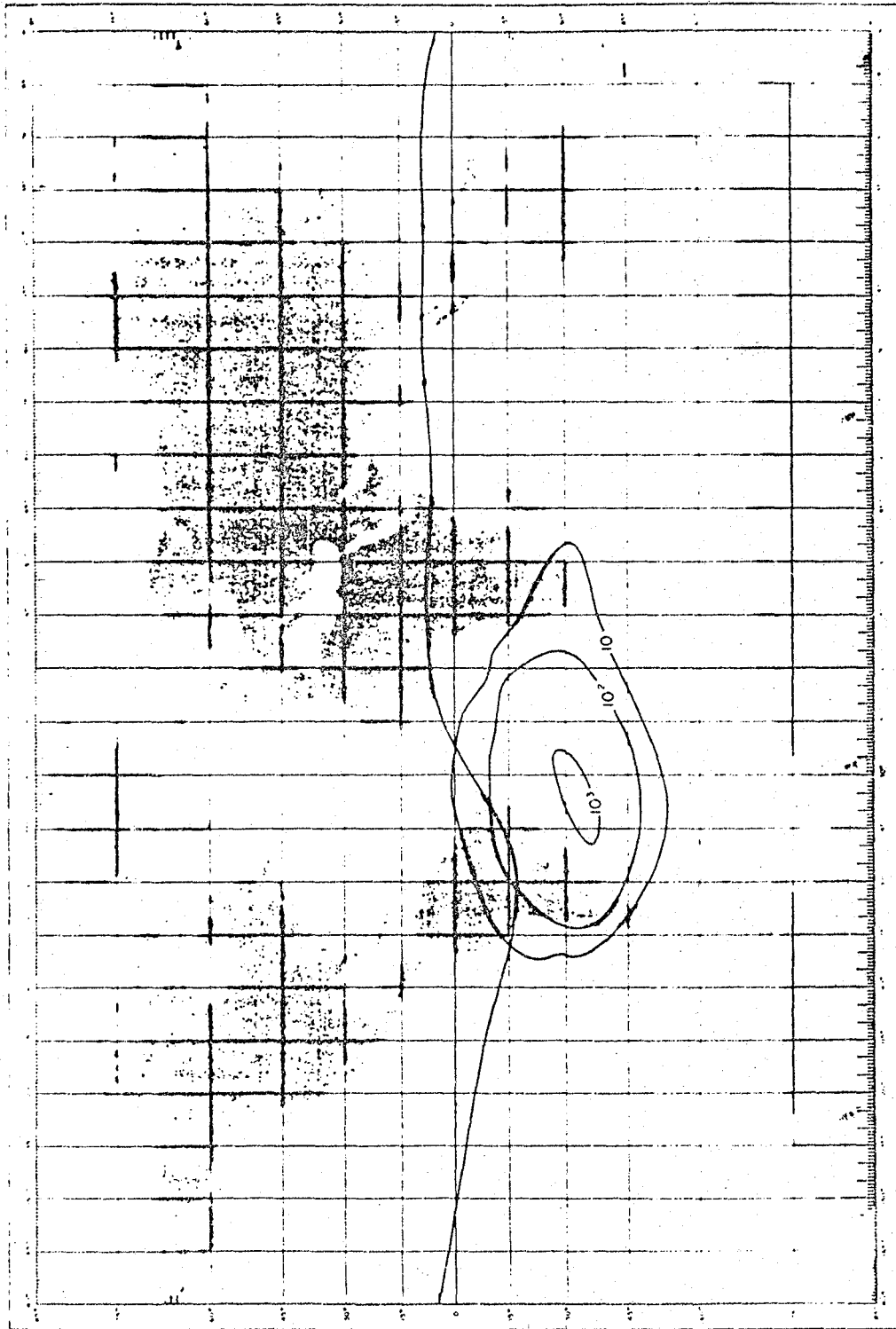
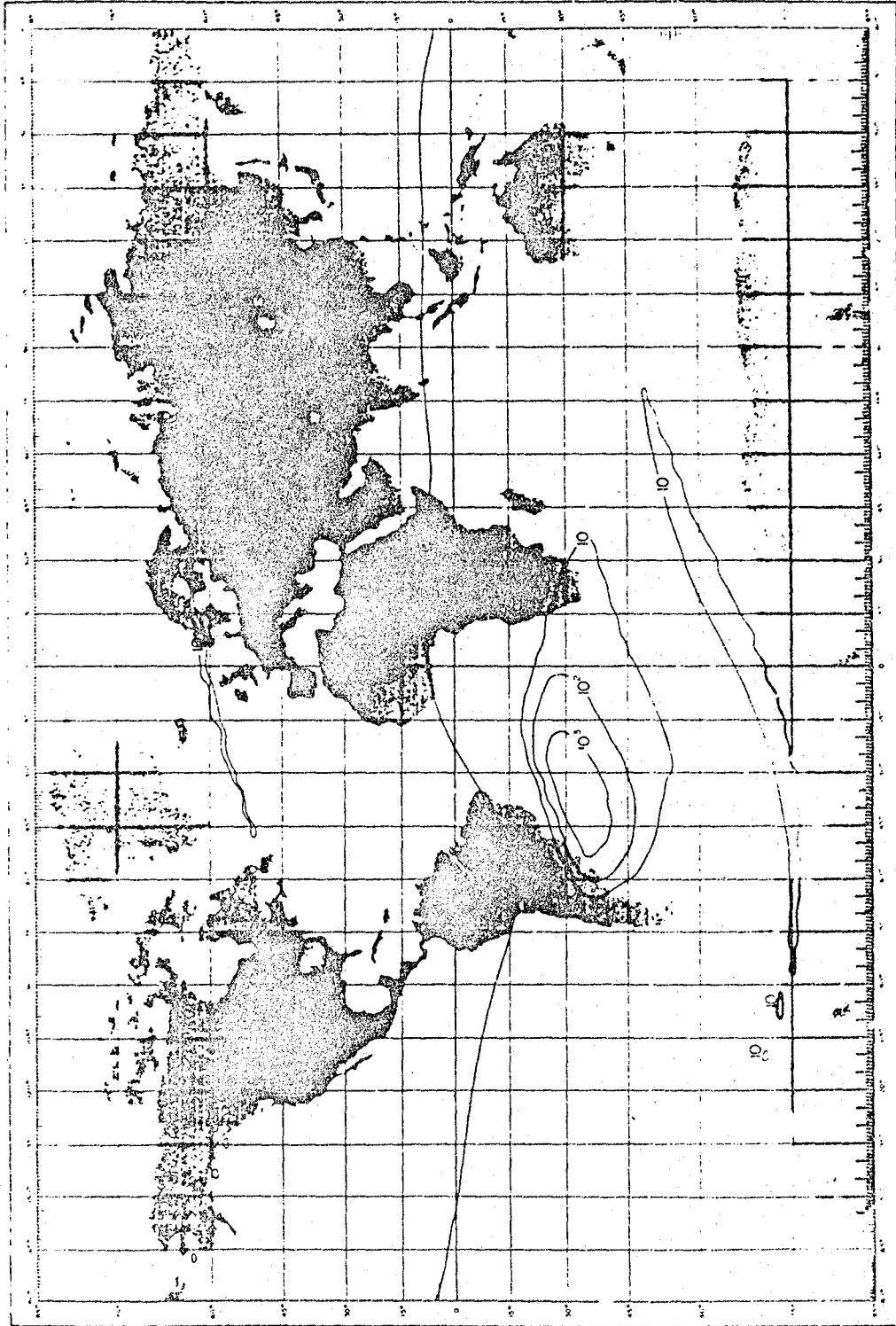
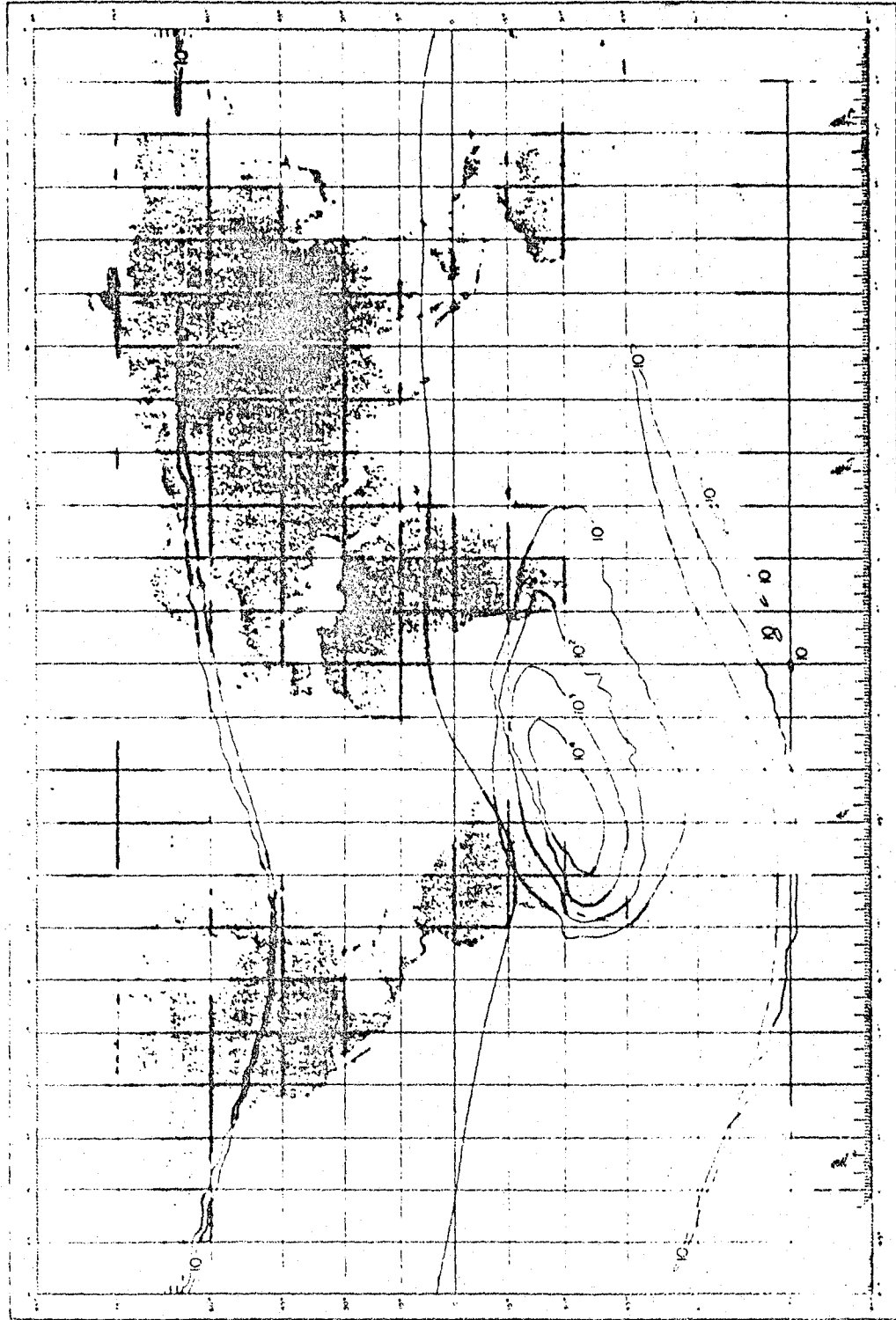


FIGURE 3. ELECTRON FLUX CONTOURS-E > 5 MEV ALTITUDE = 300 KM



ORIGINAL
OF P007

FIGURE 4. ELECTRON FLUX CONTOURS-E > 5 MEV ALTITUDE = 500 KM



ORIGINAL FILED
OF POOR QUALITY

FIGURE 5. DETECTOR LENGTH AFFECTS RADIATION-PULSE RATES IN Ge-X DETECTORS

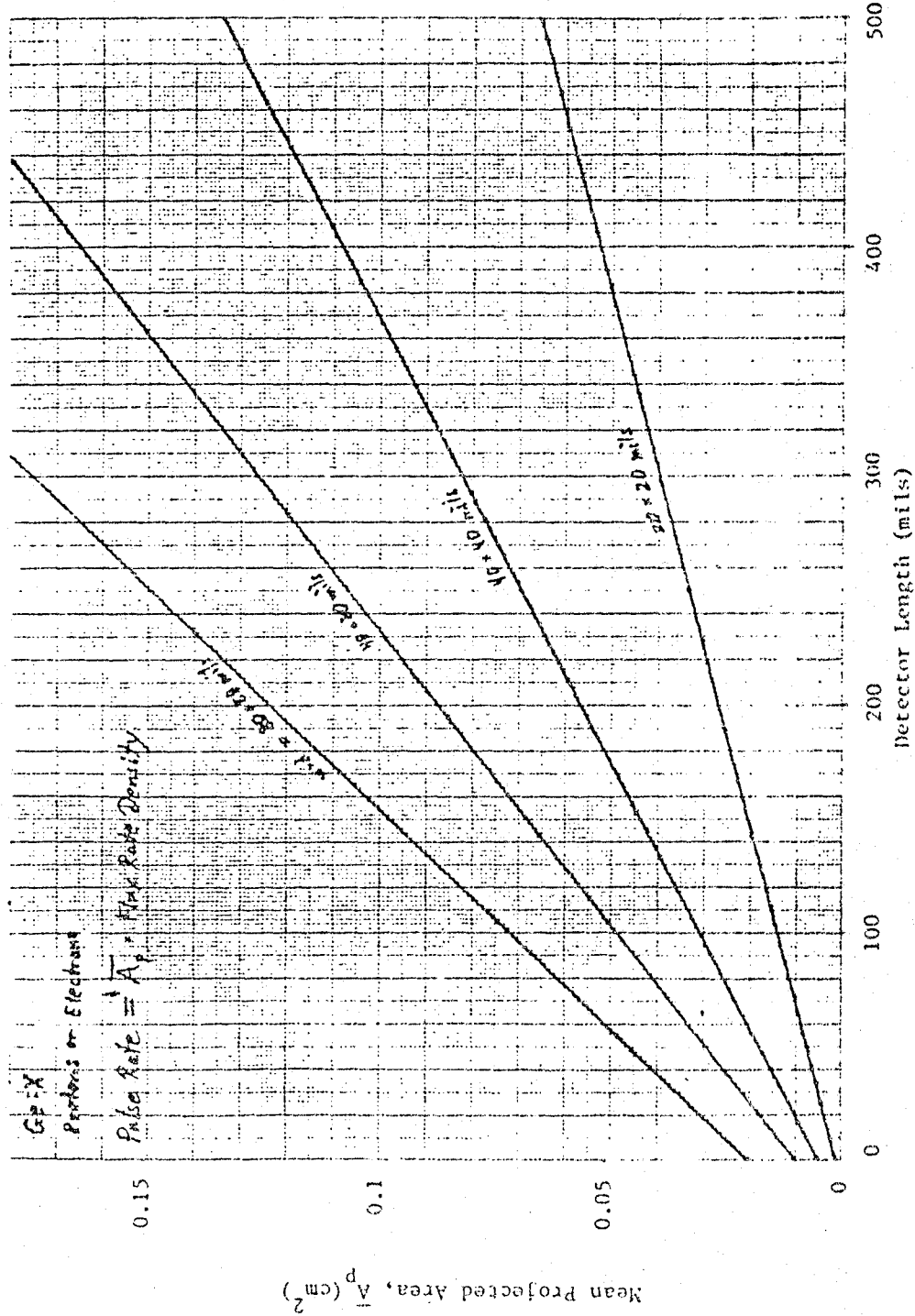
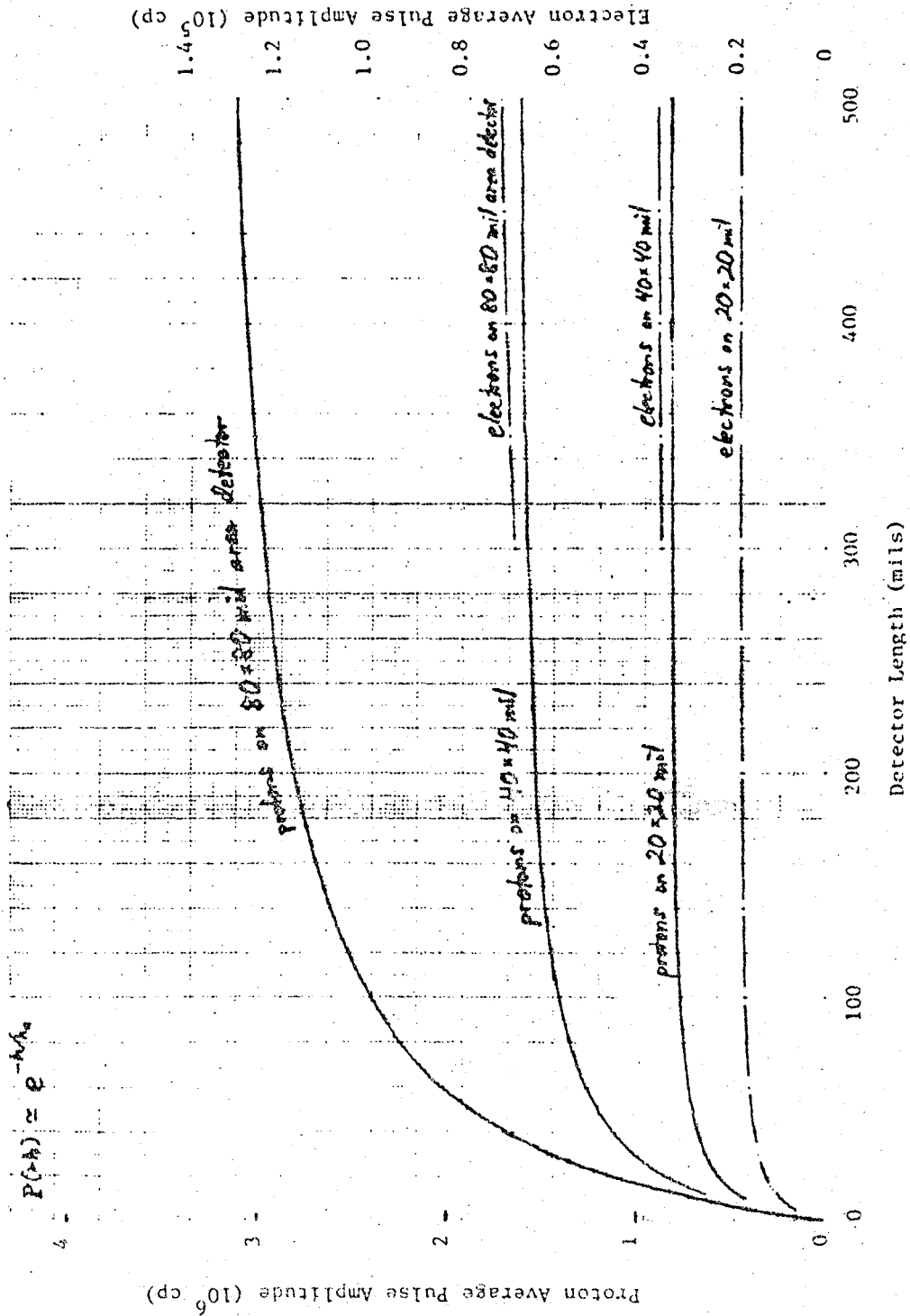
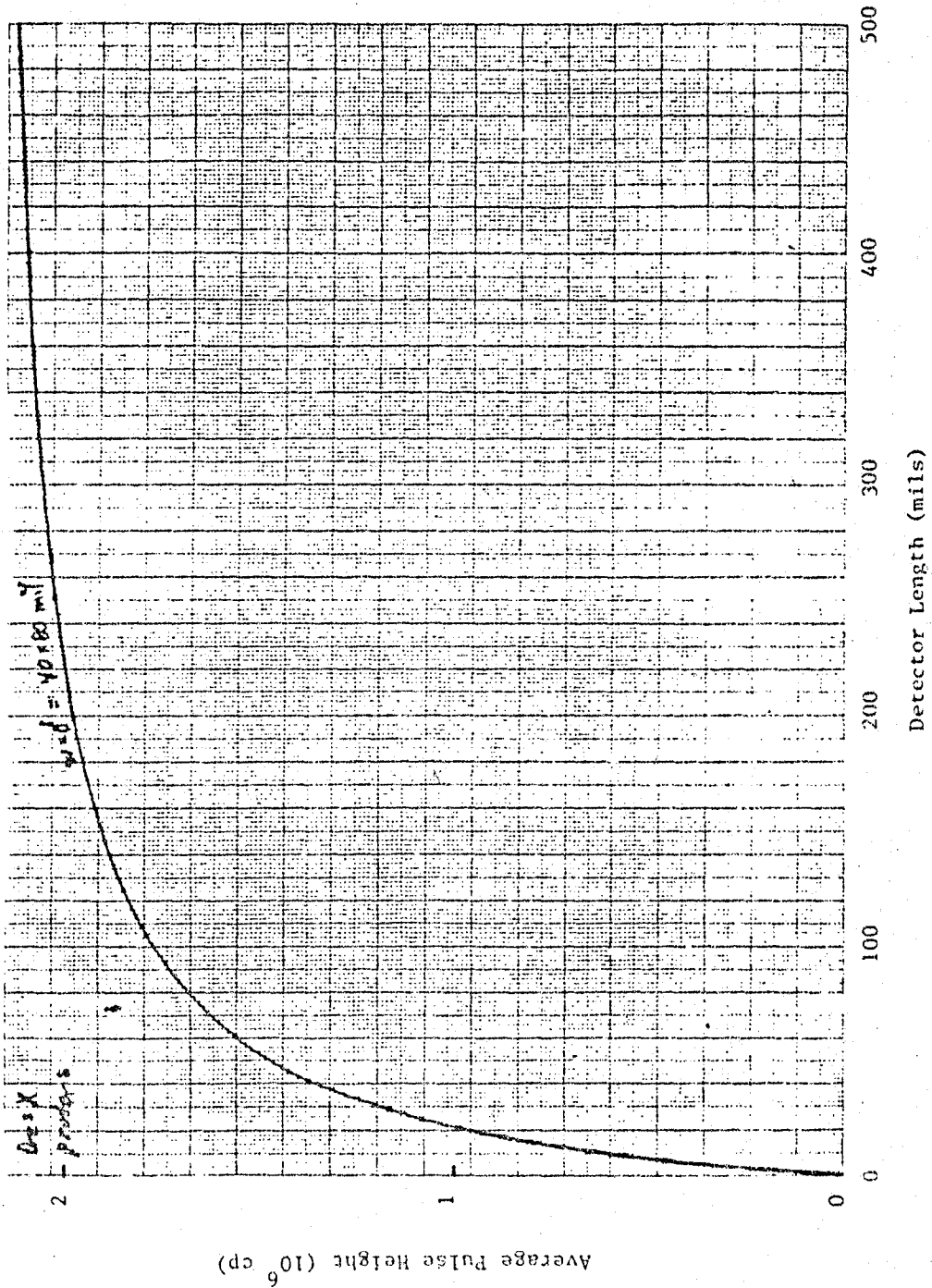


FIGURE 6. Ge: X DETECTOR LENGTH AFFECTS AVERAGE PULSE AMPLITUDE



ORIGINAL
OF POCR 67-217

FIGURE 7. AVERAGE PROTON-PULSE AMPLITUDE FOR Ge: X DETECTORS OF 2:1 CROSS SECTION



ORIGIN
OF POOR QUALITY

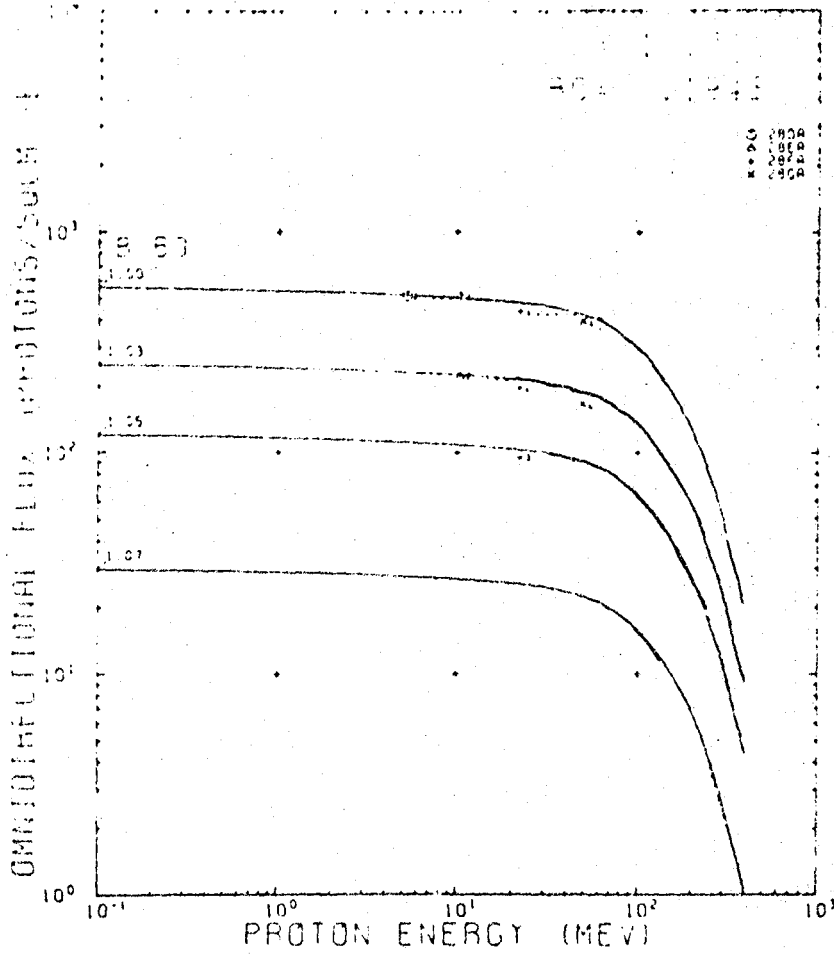


Figure E8. AP8MAX and Data Flux vs Energy Comparison Plot for L = 1.17 R_E

From: NSSDC/WDC-A-R&S 76-06.

ORIGINAL
OF POC...

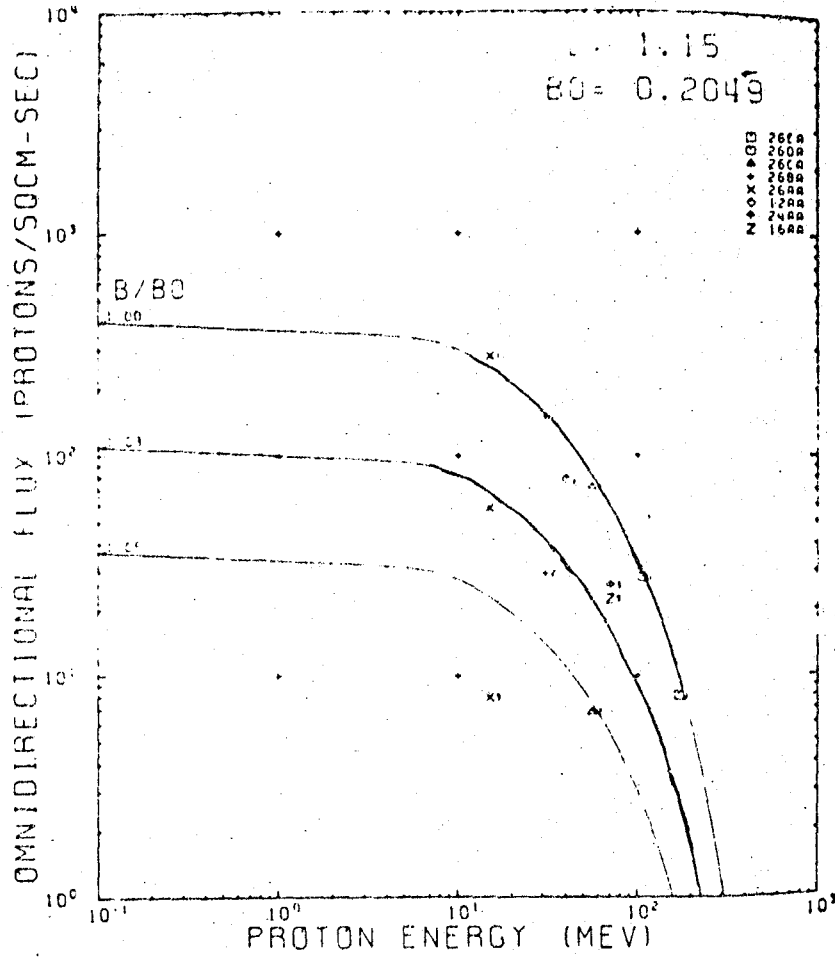


Figure E9. AP8MIN and Data Flux vs Energy Comparison Plot for $L = 1.15 R_E$

From: NSSDC/WDC-A-R&S 76-06

APPENDIX F

DESIGN DATA FOR BELLEVILLE SPRING WASHERS

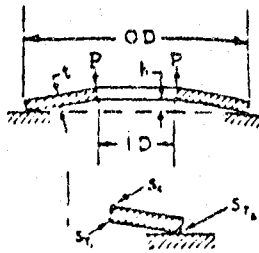
107-111-111

Specific Nomenclature for Belleville Spring Washer

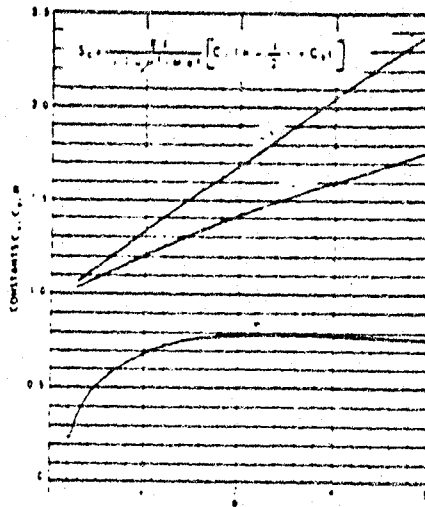
$R = OD - ID$
 $h =$ inside height in inches
 $P_F =$ load at flat position, lb.
 $H = h + t$

$S_c =$ Compressive stress at upper inner edge, psi
 $S_T =$ Tensile stress at concave side of ID, psi
 $S_T =$ Tensile stress at concave side of OD, psi

ORIGINAL PART OF POOR COPY



—Compressive stress constants for Belleville spring-washer calculations



$$P = \frac{E t^3}{(1-\mu^2) M_2} \times [(h-f)(h-\frac{f}{2})(t+\frac{f}{2})]$$

when $h=f$

$$P_F = \frac{E h^3}{(1-\mu^2) M_2}$$

M_2 constant for given design's

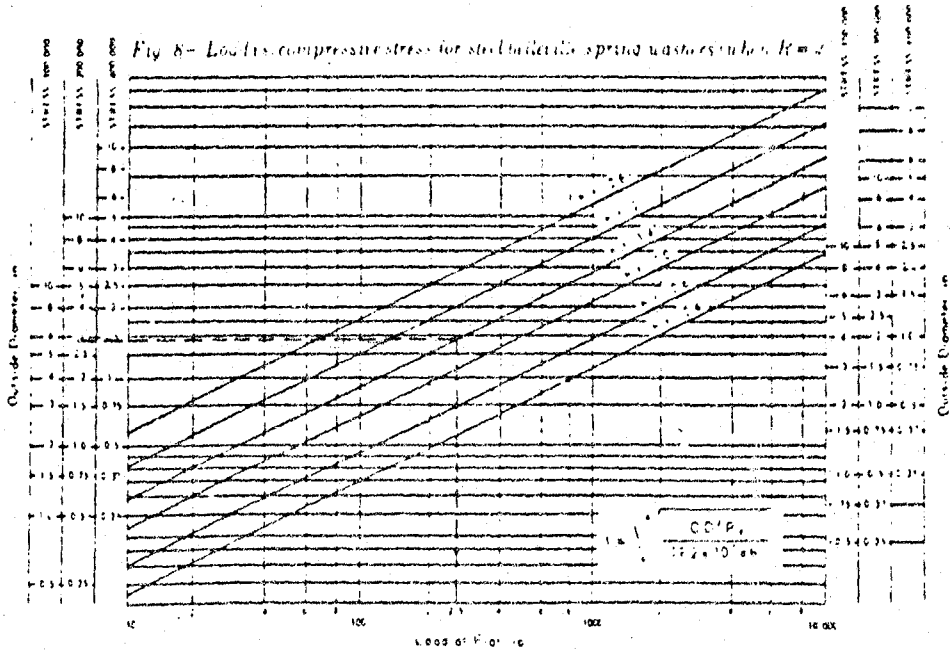
$$\frac{E}{\pi R^2 t} \left(\frac{E-\nu^2}{P} \right)$$

$$a = OD/2, \text{ in.}$$

$$C_1 = \frac{6}{2 \ln R} \left[\frac{R-h}{2 \ln R} - 1 \right]$$

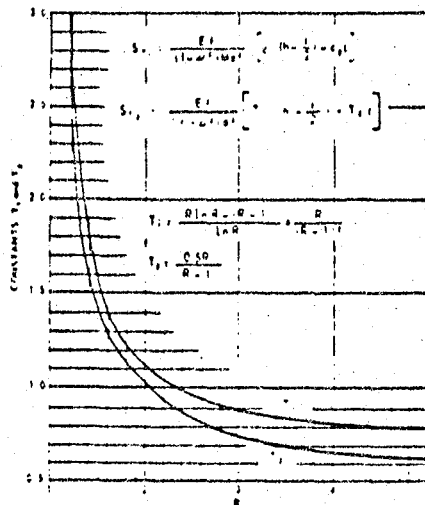
$$C_2 = \frac{6}{2 \ln R} \left[\frac{R-h}{2 \ln R} \right]$$

$\ln =$ natural log.

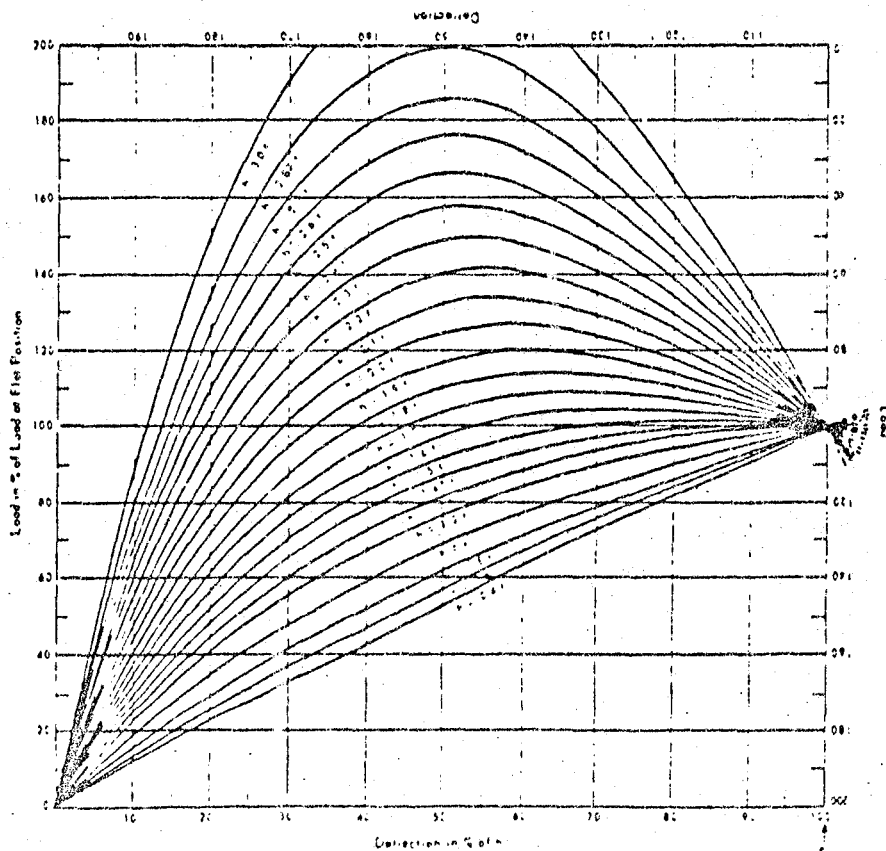


ORIGINAL COPY
OF POOR QUALITY

Tensile-stress constants for bellville
spring washers



Load deflection characteristics in bellville spring washers



APPENDIX G

THERMAL BUSS COMPUTATIONS

Incorporated herein are designer's hand calculations made to determine the size of the thermal buss components and the stress and torque required for the thermal buss screws.

G1 Length of Invar Sleeve

Assume a silver buss of length 0.625 inches in compression:

Contraction of buss components upon cooling to 2K will be

$$\text{Silver Buss } \Delta L/L \approx 0.0041 \text{ in/in}$$

$$\text{Invar 36 Sleeve } \Delta L/L \approx 0.000117 \text{ in/in}$$

$$\text{CRES 303 Screw } \Delta L/L \approx 0.00356 \text{ in/in}$$

The length of sleeve (x) must be selected so that

$$\Delta L_{Ag} + \Delta_{\text{sleeve}} = \Delta L_{\text{CRES screw}}$$

$$\text{or } 0.625 (-0.0041) + x (-0.000117) = (0.625 + x) (-0.00356)$$

so that

$$x = 0.09593$$

Sleeve should be 0.096 inches long with threads in nut going to the bottom.

G2 Stress and Torque for Thermal Buss Screws

The area of the silver buss in contact with a sapphire board is

$$0.025 \times 0.150 \approx 0.00375 \text{ in}^2$$

For 10^4 psi load will be 37.5 lb/screw

$$\text{Diameter of Screw Shank (\#1)} = 0.073$$

$$\text{Area of Screw Shank} = 0.0042 \text{ in}^2$$

$$\text{Stress} = 37.5/0.0042 = 8.964 \text{ Kpsi}$$

which is safe for CRES 303.

This would require a torque of approximately

$$T = KDP$$

where $K \sim 0.2$ (Assumed, Range is typically 0.13 to 0.21)

$D = 0.073$ in

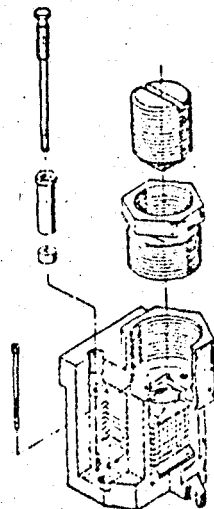
$P = \text{Preload} = 37.5$ lb

$T \sim 0.55$ lb-inches = 8.8 o2-inches

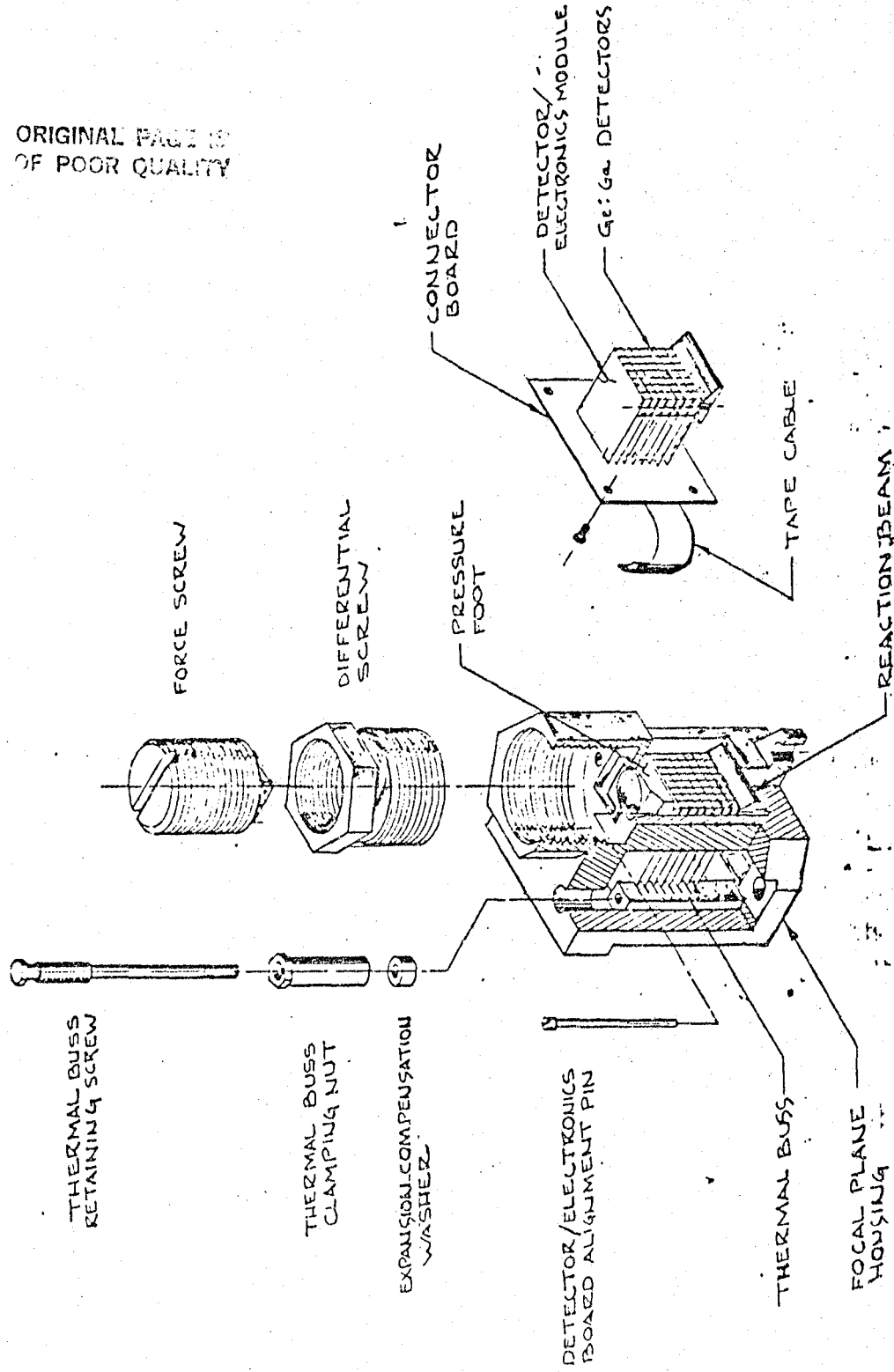
ORIGINAL PAGE IS
OF POOR QUALITY

APPENDIX J
UNRELEASED DRAWING SET

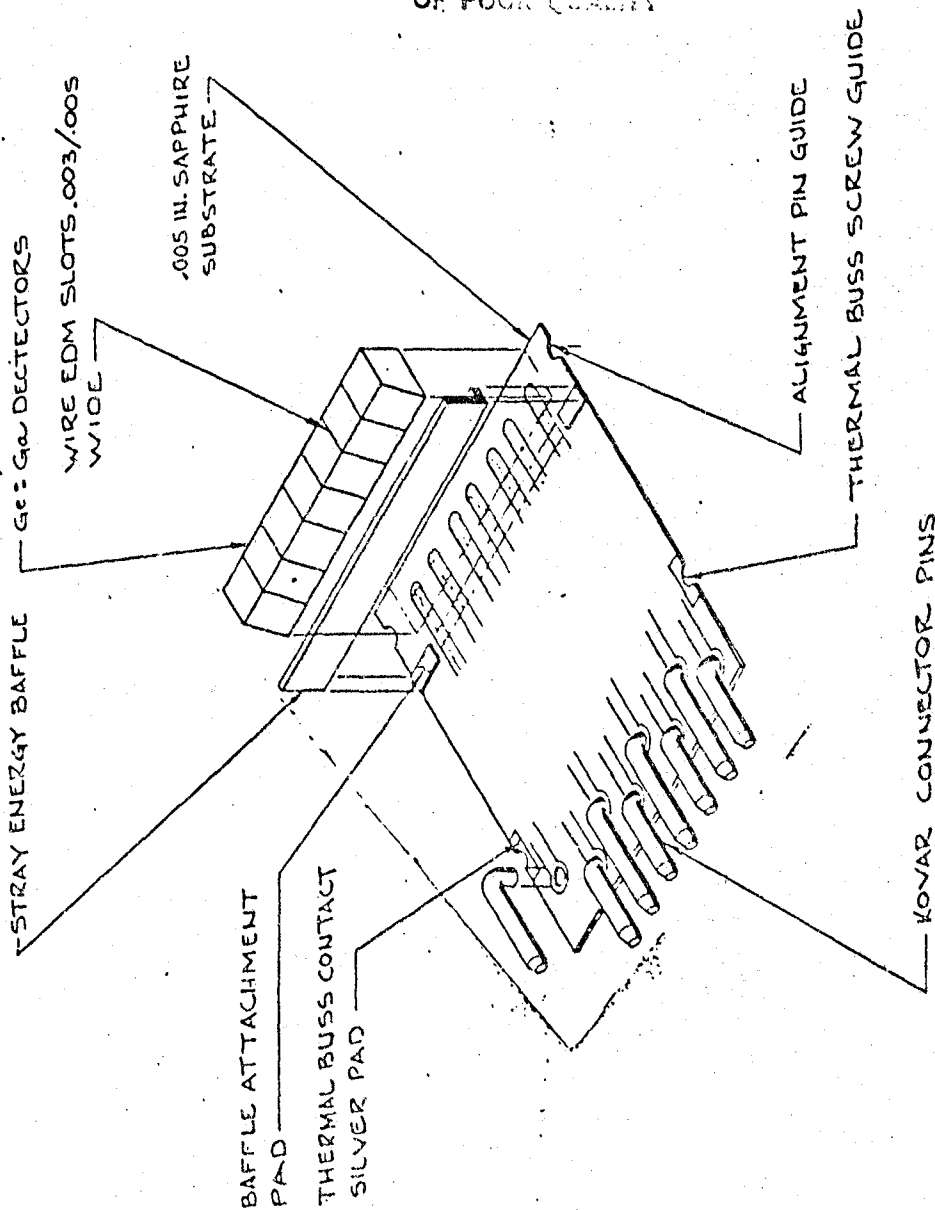
**HYBRID GE : GA
DETECTOR ARRAY**



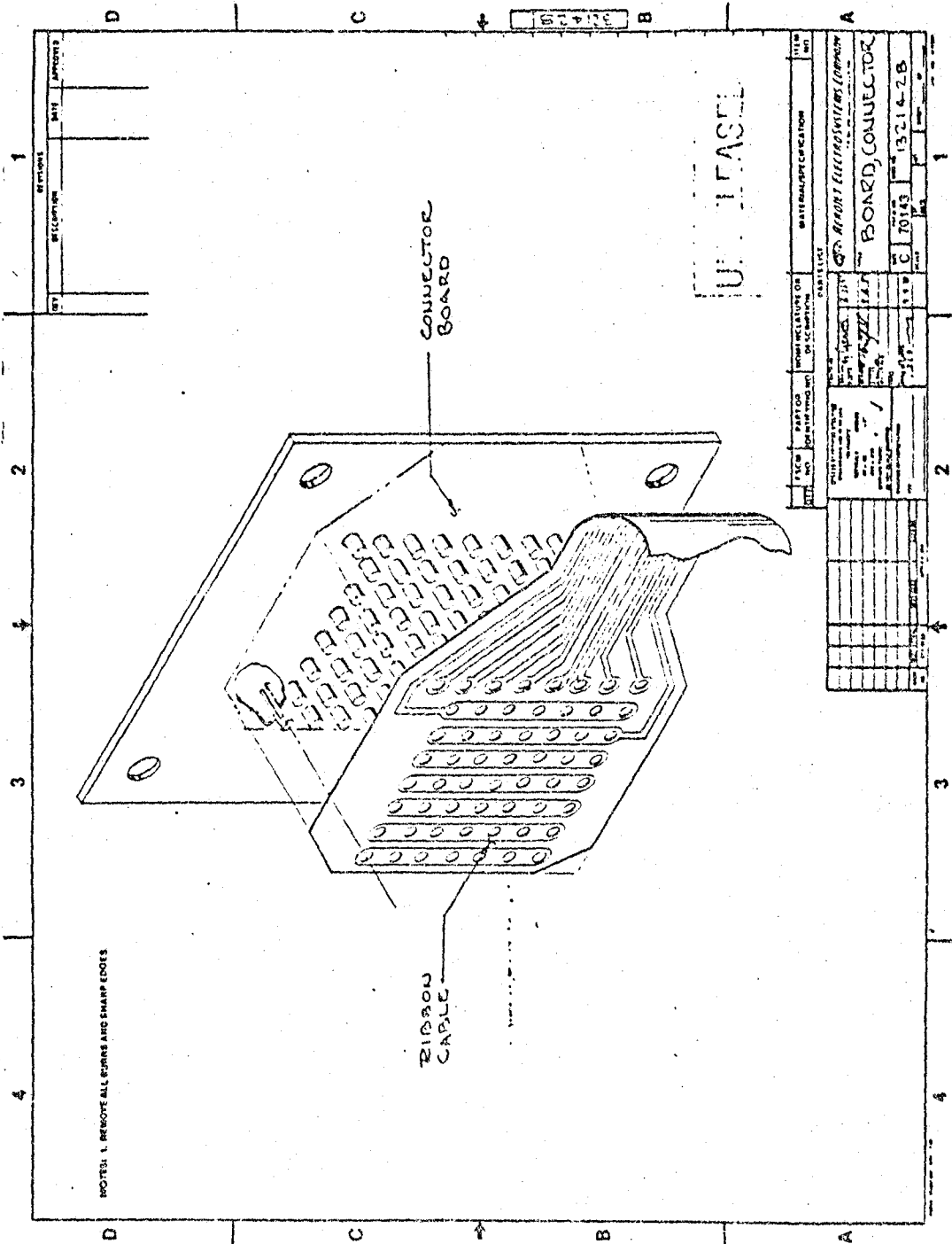
ORIGINAL PAGE IS
OF POOR QUALITY



ORIGINAL DESIGN
OF POOR QUALITY



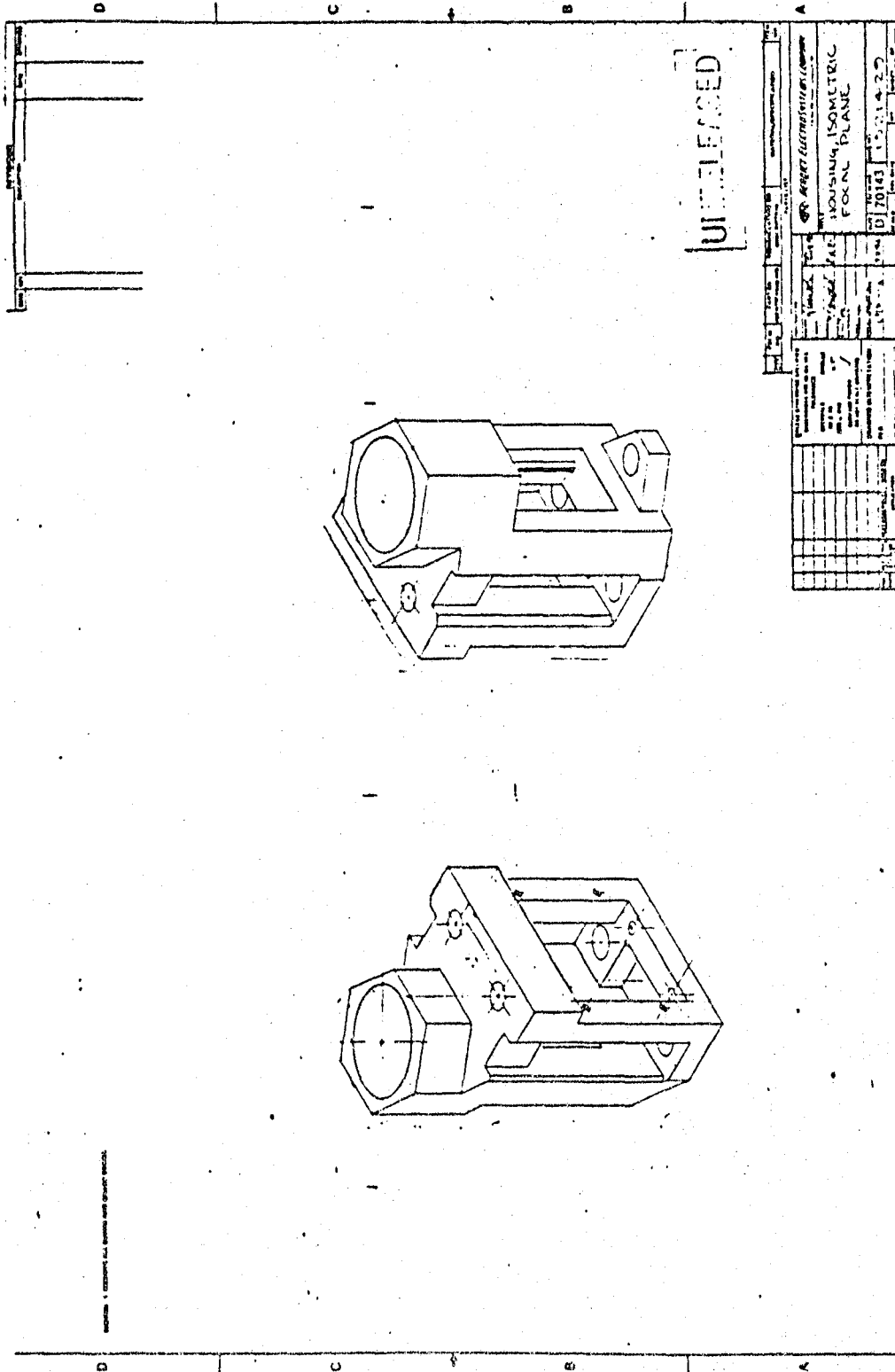
ORIGINAL P...
OF P... C...



REV	DESCRIPTION	DATE	APPROVED

FILE NO.	PROJECT NO.	DATE	BY	FOR

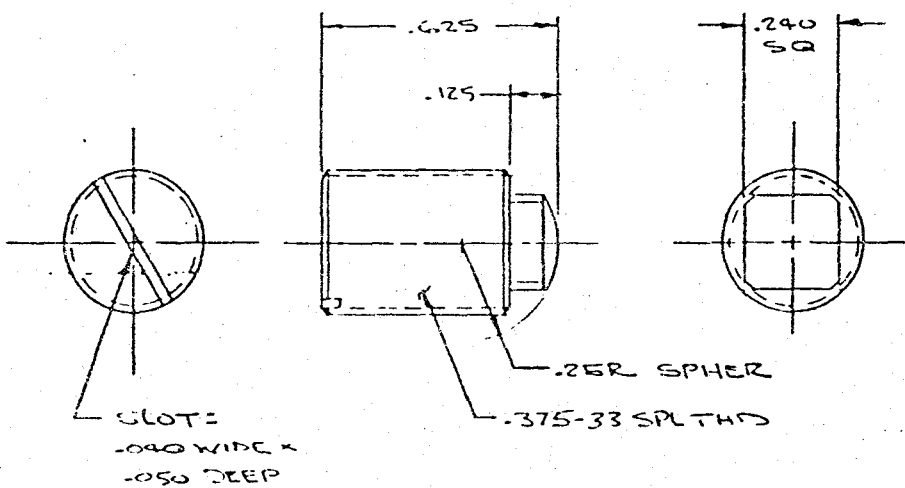
ITEM NO.	DESCRIPTION	QTY	UNIT



1321433

NOTES: 1. REMOVE ALL BURRS AND SHARP EDGES.

REVISIONS			
REV	DESCRIPTION	DATE	APPROVED



39

125

ORIGINAL FILED IN
OF POOR QUALITY

INVAR

QTY	FSCM NO	PART OR IDENTIFYING NO	NOMENCLATURE OR DESCRIPTION	MATERIAL/SPECIFICATION	ITEM NO

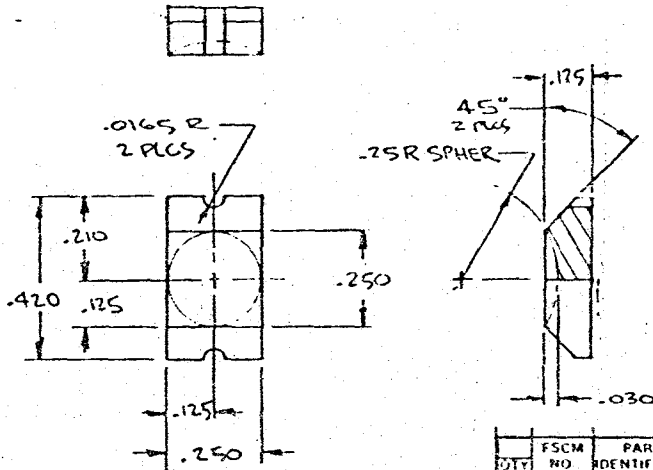
UNLESS OTHERWISE SPECIFIED DIMENSIONS ARE IN INCHES FRACTIONS		DRAWN BY <i>[Signature]</i> 1-5-58		 <small>111 2nd St. Santa Ana, Calif. 92701</small>
DECIMALS	ANGLES	CHECK	TITLE	
DT & BS	° 2"	BY <i>[Signature]</i> 1-5-58	SCREW, FORCE	
1/16 & 3/16		DATE		
SURFACE FINISH		SCALE		
NO. OF REACT DRAWING		SIZE		
		FSCM NO	DWG NO	
		B	70143	
		SCALE	1321433	
		DATE		
		WT		
		SHEET	OF	

Report #6907

↓ | 1321436 |

NOTES: 1. REMOVE ALL BURRS AND SHARP EDGES.

REVISIONS			
REV	DESCRIPTION	DATE	APPROVED



TUNGSTEN CARBIDE

QTY	FSCM NO	PART OR IDENTIFYING NO	NOMENCLATURE OR DESCRIPTION	MATERIAL/SPECIFICATION	ITEM NO
-----	---------	------------------------	-----------------------------	------------------------	---------

PARTS LIST

UNLESS OTHERWISE SPECIFIED DIMENSIONS ARE IN INCHES DECIMALS ANGLES XX.XX XX° XX'		DRAFTING SURFACE FINISH DIMENSIONS UNLESS OTHERWISE SPECIFIED		CONTROL NO DRAWN BY CHECKED BY DATE TITLE	
1321436 PARTS LIST		HEADJET ELECTROSYSTEMS COMPANY 1321436		TITLE FOOT, PRESSURE	
DATE SHEET NO		DATE SHEET NO		DATE SHEET NO	

↑ J12

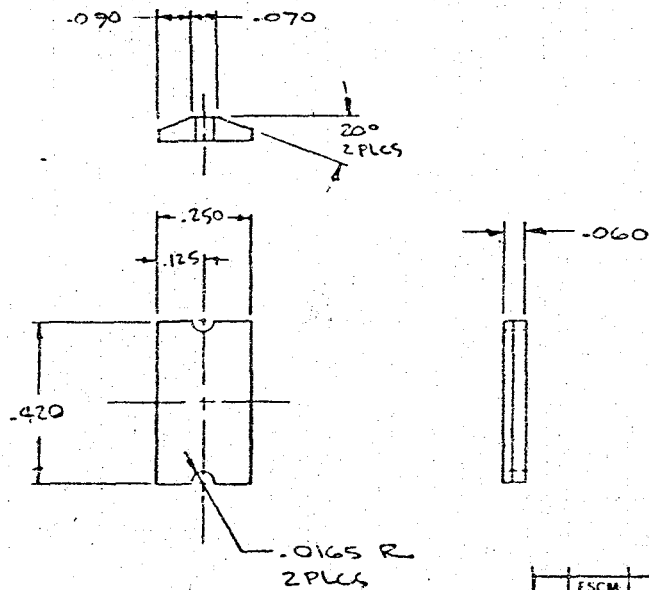
128

OF PARTS

Report #6907

↓ | 1321437

NOTES: 1. REMOVE ALL BURRS AND SHARP EDGES.



REVISIONS			
REV	DESCRIPTION	DATE	APPROVED

J13

129

ORIGINAL OF RECORD

TUNGSTEN CARBIDE

QTY	FSCM NO	PART OR IDENTIFYING NO	NOMENCLATURE OR DESCRIPTION	MATERIAL/SPECIFICATION	ITEM NO

PARTS LIST

SHEET DIMENSIONS: 11.000 x 8.500 DIMENSIONS ARE IN INCHES TOLERANCES: DECIMALS .0005 FRACTIONS 1/32 ANGLES .001 HOLE DIA .001 SURFACE FINISH .8 DO NOT SCALE DRAWING	CONTROLS: DRAWN: <i>CLAYTON</i> CHECKED: <i>CLAYTON</i> DESIGNED: <i>CLAYTON</i> DATE: 6-17-68 PER: <i>CLAYTON</i>	READJET ELECTROSYSTEMS COMPANY 10000 W. 10th Street, Omaha, NE 68114 TITLE: BEAM-REACTION SIZE: B FSCM NO: 70143 DWG NO: 1321437 SCALE: 1:1 DATE: 6-17-68 SHEET: 1 OF 1
--	---	---

Report #6907

END

DATE

FILMED

DEC 18 1984

End of Document